ABSTRACT

Title of Document: SYNTHESIS AND CHARACTERIZATION OF FUNCTIONAL ONE DIMENSIONAL NANOSTRUCTURES

Kwan Lee, Doctor of Philosophy, 2011

Directed By: Associate Professor Min Ouyang, Department of Physics

One- dimensional (1D) nanostructures have received growing interest due to their unique physical and chemical properties and promising nanodevice applications, as compared with their bulk counterparts. Complex 1D nanostructures with tunable properties and functionalities have been successfully fabricated and characterized in this thesis. I will show our recent efforts on precise controlled 1D nanostructures by template- assisted electrochemical synthesis as well as fundamental understanding of their physical behavior and growth mechanism of as-synthesized nanostructures. Particularly, three topics are presented: Firstly, a constant current (CC) based anodization technique is newly demonstrated to fabricate and control the structure of an anodic aluminum oxide (AAO) template. This technique has enabled the formation of long- range self- ordered hexagonal nanopore patterns with broad range of tunability of interpore distance (D_{int}). In addition, the combination of CC based anodization and conventional CV anodization can offer a fast, simple, and flexible

methodology to achieve new degrees of freedom for engineering planar nanopore structures. This work also facilitates our understanding of the self- ordering mechanism of alumina membranes and complex nanoporous structure. Secondly, functional 1D nanostructures including pure metallic, magnetic and semiconducting nanowires and their heterostructure are demonstrated by versatile template- based electrochemical deposition under feasible control. This study has enabled the creation of high quality and well- controlled 1D nanostructures that can be applied as a model system for understanding unique 1D physics. Some preliminary investigations including exciton confinement, anisotropic magnetism and surface plasmon resonance are also presented. Lastly, a novel and universal non-epitaxial growth of metal-semiconductor core-shell lattice-mismatched hybrid heterostructures is presented. Importantly, a new mechanical stress driven crystalline growth mechanism is developed to account for non-epitaxial shape and monocrystalline evolution kinetics.

SYNTHESIS AND CHARACTERIZATION OF FUNCTIONAL ONE DIMENSIONAL NANOSTRUCTURES

By

Kwan Lee

Dissertation submitted to the Faculty of the Graduate School of the
University of Maryland, College Park, in partial fulfillment
of the requirements for the degree of
Doctor of Philosophy
2011

Advisory Committee:
Professor Min Ouyang, Chair
Professor Theodore L. Einstein
Professor Lourdes G. Salamanca-Riba
Professor Raymond J. Phaneuf
Professor John Cumings

Dedication

To

My parents Gyun Lee and Younghwan Choi,

My parents-in-law Yongsub Choi and Yeonza Lee,

My lovely wife Sun Choi,

and My adorable daughter Alexis Jin Lee

Acknowledgements

I would like to express my sincere gratitude to my advisors, Prof. Min Ouyang for giving me the opportunity to work on exciting projects. I would especially like to thank for his guidance and support throughout my Ph.D research at the University of Maryland. I benefited from his guidance in every aspect during my Ph.D study, including the discussions we held and intelligent suggestions he made regarding my research.

I would like to thank my committee members, Professor Theodore L. Einstein, Professor Lourdes G. Salamanca-Riba, Professor Raymond J. Phaneuf, and Professor John Cumings for their invaluable advice.

Finally, I would also like to thank all previous and current members in Professor Ouyang Group for your help during my Ph.D. studies.

Table of Contents

List of Figures

Chapter 1: Introduction: One- Dimensional Nanostructures and AAO Techniques

1.1 Nanoscience and Nanotechnology

Nanoscience and nanotechnology is a fast-growing interdisciplinary field that expands exciting research in many different fields, including chemistry, physics, material science and biology. Many unique physical and chemical properties of confined structures in nanoscale have been theoretically predicted and experimentally observed due to quantum confinement effect and surface/interface effect. Therefore, development of new synthetic approaches and characterization tools of nanoscale structures that can manifest enormous size related effects has been extremely critical for the field.

Strategies that have been applied to achieve various nanoscale structures can be classified to two different categories, “top-down” approach and “bottom-up” approach. The top-down approach involves carving down a single crystalline bulk material into individual nanometer-sized grains. A common and high-throughput top-down approach is realized with advanced lithographic tools (such as electron beam lithography) used by today's semiconductor industries to produce electronic devices [1, 2]. However, dramatically increasing cost of each facilities as well as physical limitation of lithographic tools with internal stress and surface defects has posed significant challenges to continuation of this success in the top-down approach.

As an alternative, the "bottom-up" paradigm starts with simple building blocks such as atoms, molecules and nanoclusters, and involves the build-up of a material from the bottom, atom-by-atom or molecule-by-molecule. One extreme demonstration of this strategy is the adding, removal and manipulation of single atoms with scanning probe microscope (SPM) [3-5]. Bottom-up chemical synthesis also represents another attractive method and has demonstrated capability to build up complex structures through self-assembly of novel synthetic nanostructures with precise and rational control of size, composition and properties [6-9]. This approach is more likely to yield nanostructures with more homogeneous chemical composition and less defects as well as better long-range ordering.

My doctoral research has focused on synthesis and characterization of novel functional one- dimensional nanostructures of pure metallic, magnetic and semiconductor materials and their hybrid heterostructures via bottom-up chemical synthesis. In particular, a tunable nanoporous aluminum oxide template has been investigated under a newly developed constant current anodization approach in Chapter 2 and has made it possible to overcome traditional limitations and disadvantages regarding the aluminum anodization. Enabled by our tunable ordered porous nanotemplate, well-controlled one dimensional nanostructures possessing unique optical, plasmonic and magnetic properties based on template- assisted electrochemical deposition will be discussed in Chapter 3. Lastly, I have further demonstrated a novel route of non-epitaxial growth of anisotropic metal core-semiconductor shell nanostructures through a new grain growth mechanism in the range from nanoscale to micron-scale in Chapter 4.

1.2 One- Dimensional Nanostructures

Nanostructures are defined as structures which have at least one dimension below 100 nm and can be generally classified into zero- dimensional (0D) nanostructures (or quantum dots), one- dimensional (1D) nanostructures (or nanowires), and two-dimensional (2D) nanostructures (or quantum wells) [10]. Among all these nanostructures, 1D nanostructures with cross-sections of 2-200 nm and lengths up to several micron-meters (i.e., large aspect ratio) are believed to provide a good opportunity for applications in mesoscopic physics allowing electrons, holes or photons to propagate freely along the long dimension and to be quantum confined in the other two dimensions. Such 1D nanostructures have also been demonstrated to play important roles as nano-macro interfacial interconnects that can bridge nanoscopic and macroscopic world in the upcoming generations of nanometer scale electronics, optoelectronics, photonics and electromechanical devices [11] since so called “nanowhiskers” [12], and later “nanowires” [13] have been developed in the 1990s.

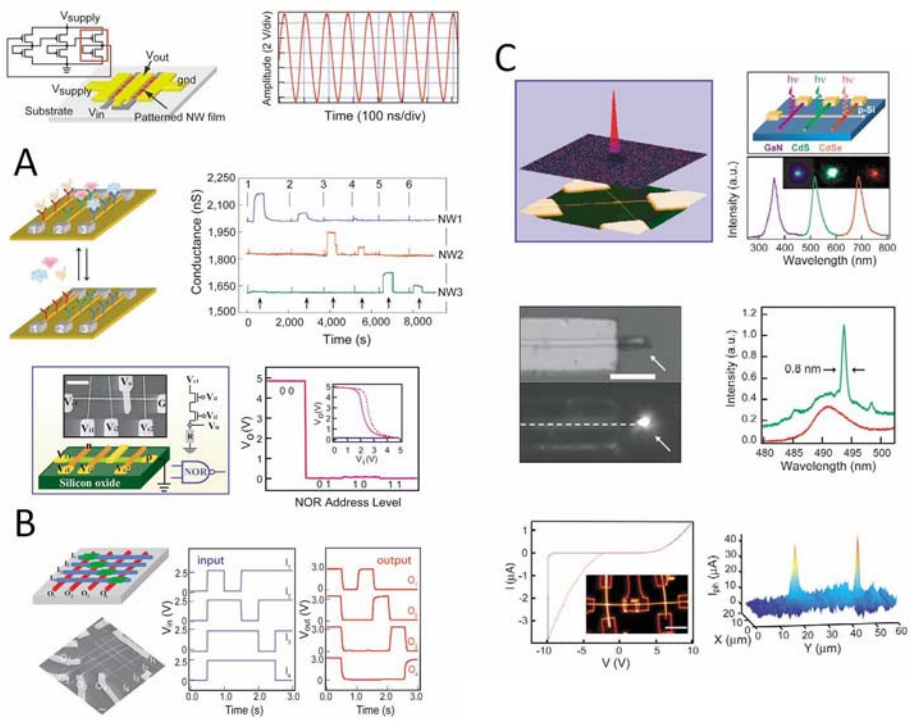

Figure 1.1 Examples of the 1D nanostructures in electronics, optoelectronics, and photonics applications with (A) Si NWFETs, (B) crossed Si and GaN NWs electronic logic devices and (C) crossed p-InP/n-InP and n-CdS/p-Si NWs photonic devices [14].

1.2.1 Chemical Synthesis of One- Dimensional Nanostructures

Vapor phase growth of nanowires: The gas phase generated by simple thermal evaporation in an appropriate atmosphere can react *with* a metal catalyst via the vapor-liquid-solid (VLS) process or *without* a catalyst through the vapor-solid (VS) method for 1D single element (such as Si) or compound (such as CdSe) nanostructure. Anisotropic crystal growth can be promoted with the presence of liquid alloy/solid interface by reducing symmetry of a seed based on the eutectic phase transition (for a VLS process)

and preferential reactivity and/or binding of gas phase reactants along specific crystal facets of a substrate (for a VS process) [15].

Solution phase growth of nanowires: Mass production with controlling highly reproducible shape and composition is a major advantage of solution based growth technique of nanostructures. In addition, hybrid nanostructure for multiple functions is likely assembled with other functional materials through this method in high yield, low cost and easy fabrication for nanoelectronic and biological applications. This synthetic strategy for the formation of nanowires has made use of anisotropic growth confined and directed by templates (alumina membrane, polymer membrane, mesoporous silica and self-assembly via surfactants) [16, 17], by kinetically controlled synthesis by supersaturation with metal catalyst through solution-liquid-solid (SLS) process[18], by kinetically solvothermal synthesis with appropriate capping agent [19], or by growth thermodynamically dictated by the crystallographic structure of the solid material [20]. Even though much research has been explored to elucidate growth mechanisms in solution, it is typically complicated and requires further and systematic investigation [10].

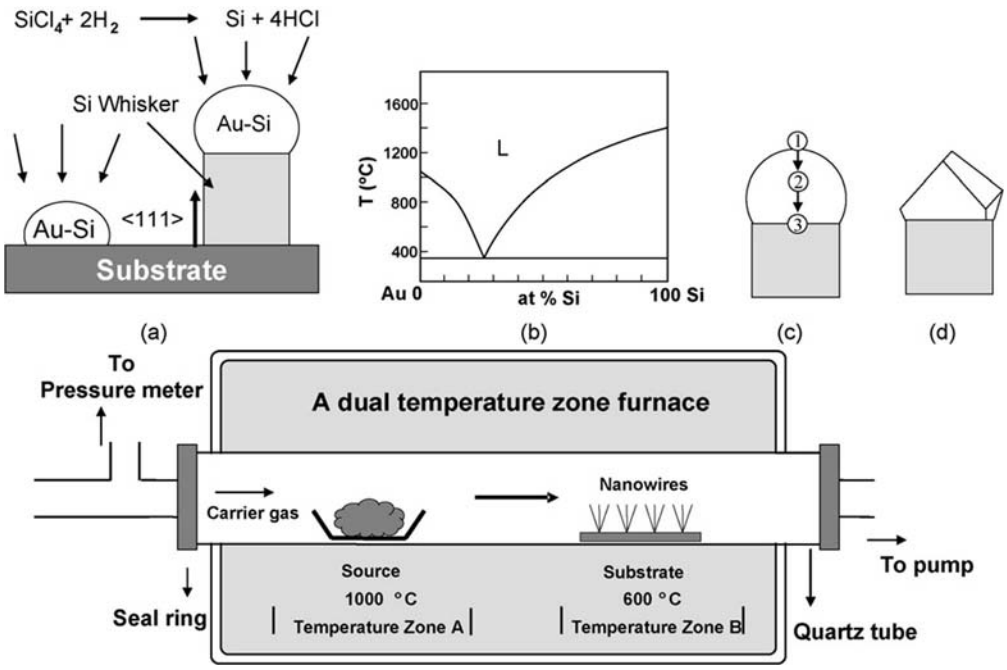

Figure 1.2 Scheme of the traditional vapor phase based nanowires formation method, for instance, silicon whisker or nanowires catalyzed with gold noble nanoparticles in gas flowing furnace [21].

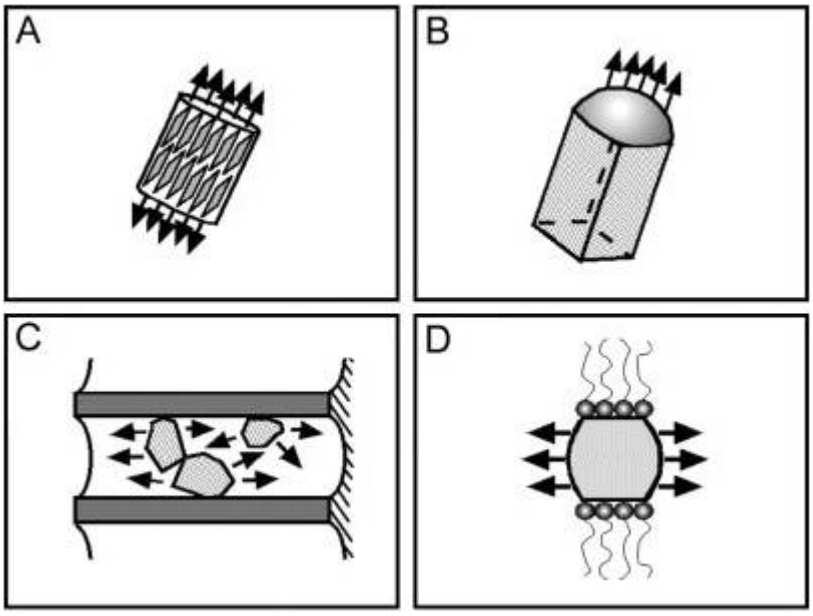

Figure 1.3 Typical strategies achieving 1D growth based in solution (A) the anisotropic crystallographic dictation structure of a solid; (B) confinement by a liquid droplet as in the SLS process; (C) directed growth with hard template; (D) kinetically controlled capping reagent [13].

1.2.2 Metallic nanowires

Free electron oscillation: The physics origin of the localized surface plasmon resonance (LSPR) is a coherent oscillation of conduction electrons physically confined in small sized metal nanostructures that can be induced at a specific frequency of incident electromagnetic waves, which exhibits unique size- and shape- dependent optical properties of nanoscale metallic nanostructures [22, 23].

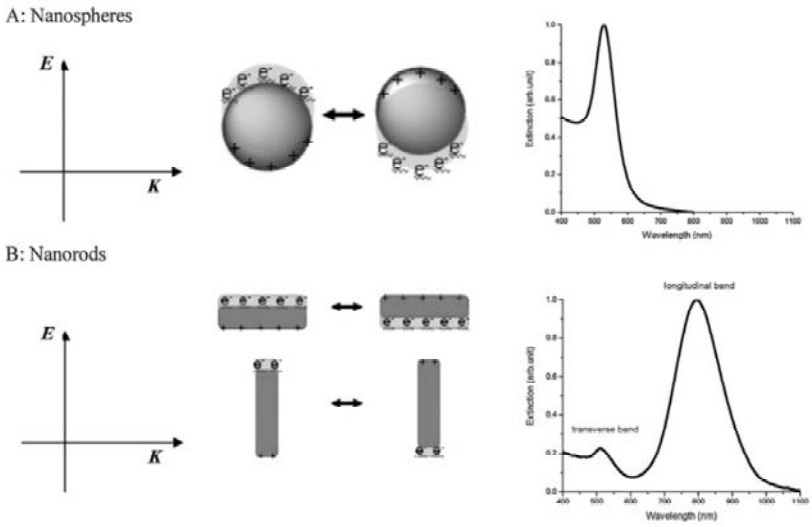

Figure 1.4. Schematic illustration of the interaction of polarized light and gold nanospheres (A) and nanorods (B) to form the electronic coherent SPR oscillation with longitude mode and transverse mode [24].

SPR of Isotropic Nanostructures: Isotropic (or spherical) noble metal nanocrystals with small size (less than 60nm for Au, and 40nm for Ag nanoparticles in which external light excitation is more associated with the absorption than the scattering

component in extinction) show only one dipole SPR mode in a uniform medium because of in- phase resonance with the incident electromagnetic field.

In the quasistatic approach, a spherical nanoparticle of radius (r) is irradiated by z polarized light of wavelength λ in the long wavelength limit with $r/\lambda < 0.1$. It can assume that electric field around nanoparticles is uniform, which allows the Laplace equation of electrostatics to be solved instead of using Maxwell's equations [25]. The resultant analytical solution for the magnitude of electromagnetic field outside the particle, $E_{outside}$, is given by

$$\mathrm{E_{outside}}(x, y, z) = \mathrm{E_0}\hat{z} - \alpha \mathrm{E_0}\left[\frac{\hat{z}}{r^3} - \frac{3z}{r^5}(x\hat{x} + y\hat{y} + z\hat{z})\right] \tag{1.1}$$

where x, y, and z are the usual Cartesian coordinates; r is the radial distance; $\hat{x}$, $\hat{y}$, and $\hat{z}$ are the Cartesian unit vectors; and α is the metal polarizability. The simplest way to describe LSPR can be found in the Mie scattering theory for calculating the extinction (absorption + scattering) cross section of a metal nanosphere [26]:

$$C_{extinction} = \frac{24\pi^2 R^3 \varepsilon_{medium}^{\frac{3}{2}}}{\lambda}\left[\frac{\varepsilon_{imaginary}(\lambda)}{(\varepsilon_{real}(\lambda)+2\varepsilon_{medium})^2+\left(\varepsilon_{imaginary}(\lambda)\right)^2}\right] \tag{1.2}$$

where $C_{extinction}$ is the extinction cross section, R is the radius, and ε_m is the relative dielectric constant of the medium surrounding the nanosphere. This equation shows that the interaction between a metal nanoparticle and light depends strongly on its dielectric properties (ε_{real} and $\varepsilon_{imaginary}$).

SPR of Anisotropic Nanostructures: When the diameter becomes larger, the SPR frequency is red shifted and higher order harmonics such as quadrupole SPR mode appear in the extinction due to phase retardation of the applied field inside the nanostructures. This suggests that anisotropic nanostructures with large aspect ratio should manifest rich plasmonic phenomena and physics. In the case of anisotropic noble metal nanostructure, for example, nanorods and nanowires, two or more distinct plasmon bands can be produced, which can be attributed to transverse and longitudinal dipole mode of the SPR. Using an extension of the Mie theory it is attempted here to explore theoretically the relationship between the aspect ratio of the gold nanorods and maximum absorption energy. According to the Gans theory [27, 28], the extinction coefficient γ of randomly oriented particles in the dipole approximation is

$$\gamma = \frac{2\pi N V \varepsilon_m^{\frac{3}{2}}}{3\lambda} \sum_{j=1,2,3} \frac{\left(\frac{1}{P_j^2}\right)\varepsilon_{imaginary}(\lambda)}{\left(\varepsilon_{real}(\lambda)+\frac{1-P_j}{P_j}\varepsilon_m\right)^2+\varepsilon_{imaginary}(\lambda)^2} \tag{1.3}$$

where, N is the number of particles per unit volume, V is the volume of each particle, ε_m is the dielectric constant of the surrounding medium, λ is the wavelength of the incident light, and ε_{real} and $\varepsilon_{imaginary}$ are the real and imaginary parts of material dielectric function, respectively. Dielectric constant of materials is frequency dependent, while ε_m is assumed to be a constant. P_j are the depolarization factors (the ratio of internal electric field induced by charges on the surface of a dielectric when an external field is applied to the polarization of the dielectric.) for the three axes a, b, and c of the rod with a>b=c.

In the quasistatic regime, the induced dipole moment of a spheroid is given by [29]

$$\mathbf{P} = \alpha \mathbf{E} \tag{1.4}$$

where E is the incident electromagnetic field and the polarizability (α) of a sphere and an ellipsoid can be described by [30]

$$\alpha = 4\pi R^3 \frac{\varepsilon - \varepsilon_m}{\varepsilon + 2\varepsilon_m};\ \text{for a sphere} \tag{1.5}$$

$$\alpha_{x,y,z} = 4\pi abc \frac{\varepsilon_l - \varepsilon_m}{3\varepsilon_m + 3L_{1,2,3}(\varepsilon_l - \varepsilon_m)};\ \text{for an ellipsoid} \tag{1.6}$$

The production of the plasmon resonance mode follows by setting the denominator of the equation equal to zero, with

$$\varepsilon + 2\varepsilon_m = 0\ (\text{for sphere}) \tag{1.7}$$

$$3\varepsilon_m + 3L_{1,2,3}(\varepsilon_l - \varepsilon_m) = 0\ (\text{for an ellipsoid}) \tag{1.8}$$

This condition is able to be met with

$$\varepsilon = -2\varepsilon_m;\ \text{for sphere} \tag{1.9}$$

$$\varepsilon_l = \varepsilon_m \left(1 - \frac{1}{L_{1,2,3}}\right);\ \text{for an ellipsoid} \tag{1.10}$$

They are defined with geometrical factor (L) as

$$L_1 = \frac{1-e^2}{e^2}\left(-1 + \frac{1}{2e}\ln\frac{1+e}{1-e}\right) \tag{1.11}$$

$$L_2 = L_3 = \frac{1-L_1}{2} \tag{1.12}$$

where

$$e^2 = 1 - \left(\frac{b}{a}\right)^2 \tag{1.13}$$

The ratio a/b is the aspect ratio.

It has been observed that the aspect ratio and the diameter of an anisotropic noble metal nanostructure play key roles on the dipole, quadrupole, and higher order multipole modes of plasmon resonance and are important parameters to tune and realize intense color [24], Raman enhancing capabilities and their utility as labels in biodetection platform [31]. Since many applications require a SPR band created on a specific energy, a predictive analytical equation to determine the SPR frequency is desirable. Many investigations on Au@Ag core-shell nanoparticles have been performed because they provide opportunities to tune the nanoparticles' optical properties [32-34].

Moreover, while Au nanorods via a wet-chemical synthesis have been demonstrated with reasonable control of diameter and aspect ratio, nanorods typically exhibit crystal facets, leading to inhomogeneous overgrowth of Ag due to the competing crystal growth on different side facets [35].

However, Au nanowires using electrochemical deposition typically leads to polycrystalline structure with well-controlled diameter and aspect ratio that can lead to homogenous shell growth.

In Chapter 3 of this thesis, noble metal nanowires synthesized using template-assisted electrochemical techniques represent ideal systems for studying the role of structural parameters in the anisotropy of SPR. This is enabled by the capability of controlling CC anodization for the diversity of porous nanostructure membrane regarding pore size and length. This approach allows one to adjust nanowire dimensions with

precise control over length, diameter, and composition. Having uniform diameter and aspect ratio control is a significant advantage over other solution- phase synthesized rods.

1.2.3 Magnetic nanowires

The storage density in magnetic recording storage media has increased at a very high rate over the past several years [36]. However, thermal stability will eventually stand as the ultimate limit of longitudinal recording. When bit size is reduced to increase the areal density, for good signal-to-noise ratio with over 1000 grains in each bit, the individual grains composing the media will eventually become so small that they will no longer be thermally stable [37]. One approach to extend this limit is through patterned perpendicular media, where one information bit corresponds to one single- domain. Since each bit can be composed of a single large aspect ratio nanowire with rather than ~1000 grains, the areal density of patterned media can, in principle, be much more than an order of magnitude greater than in conventional longitudinal media. While lithography based techniques shows some promise, characterization of the magnetization of such high-density arrays has been relatively lacking.

After the discovery of self-organized nanoporous structure of aluminum oxide templates using a two- step anodization procedure, the desire to produce regular arrays of nanowires has spurred significant research interest to seek the possibility of filling the pores with magnetic materials, aimed at high density perpendicular magnetic recording media through electrochemical deposition [38]. As a result, an overflow of literature on

the deposition of magnetic materials including not only common room temperature ferromagnetic materials (Fe, Co, and Ni) but also mixtures of these elements with each other and even with non-magnetic elements has appeared [39-41], and has led to the realization of a high-density surface distribution of isolated ferromagnetic columns, as well as large perpendicular magnetic anisotropy [42-44]. For example, for single element magnetic materials, an AC deposition technique was employed for Fe nanowires [42], a pulsed DC deposition was developed for Ni [45], and a DC deposition was applied for Ni and Co in nanoporous templates [38]. Moreover, both magnetic multiple layers and alloy nanowires have also been demonstrated [39, 41]. Both of these are crucial in enhancing the recording density of high-density perpendicular recording media.

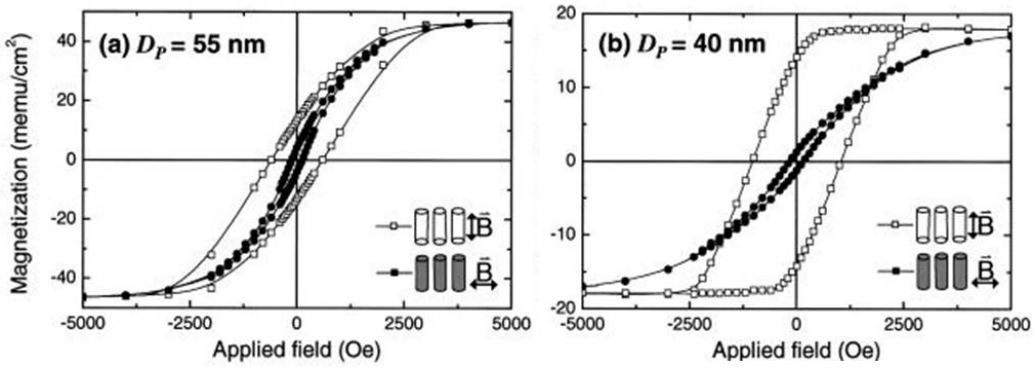

Figure 1.5. Anisotropic magnetic properties with typical hysteresis loops for nickel nanowires array in AAO template with different pore size under the applied field H parallel and perpendicular to the wire axis [46].

1.2.4 Semiconducting nanowires

Semiconducting nanowires have been reliably fabricated in single crystal form, by controlling all the material parameters such as doping and chemical composition, and used for a wide range of devices in the fields of electronics, optoelectronics, photonics and energy to healthcare including LEDs, bipolar junctions, p-n junctions, logic gates, and even computational circuits [47, 48]. Semiconducting materials have been generally prepared by high temperature solidification methods or by vapor phase methods. Liquid solution, using water or other solvents, including organic, ionic liquids, and molten salts represents another phase for growth of semiconductor thin films. In particular, electrodeposition in liquid phase of semiconducting materials can offer advantages, such as large area, low cost, generally low temperature and soft processing of materials [49].

Nanowire arrays have attracted intense attention because of their unique anisotropic electronic and optical properties. It is available by tailoring the quantum size effect in the nanostructures not only along the radial direction with small diameters, but also along the axial direction by aspect ratio control. It makes it possible to observe light trapping effect through enhancement of optical absorption efficiency of the materials [48-50], to enhance photocurrent efficiency of photo- generated electron-hole pairs in aligned nanowires [44], and to explore high density magnetic recording [51, 52] and sensors [53].

However, to date, study of the preparation of semiconductor nanowires by electrodeposition in templates has been lacking, while a variety of metal and conductive polymer nanowires arrays have been produced by electrodeposition in templates

[50, 54, 55]. For instance, silicon nanowires based on template- assisted electrodeposition have only recently been demonstrated due to challenges, such as sticky aqueous solvent and oxidation to which the higher reduction potential than water has led [56]. Moreover, intrinsic drawbacks of aqueous bath deposition include the lack of length uniformity due to hydrogen generation, the challenge of high temperature deposition and limited choice of appropriate aqueous solutions. To overcome these limitations, the method we used for semiconducting materials is based on electrodeposition into the nanopores of AAO membranes by using organic solvents such as dimethyl sulfoxide (DMSO) solution containing metal chloride. This makes high temperature deposition possible to ensure high quality of nanowires. Furthermore, by controlling deposition and discharge processes in a pulsed AC electrochemical deposition, it is possible to control the quality of the nanowires array with a remarkable degree of precision as demonstrated in Chapter 2.

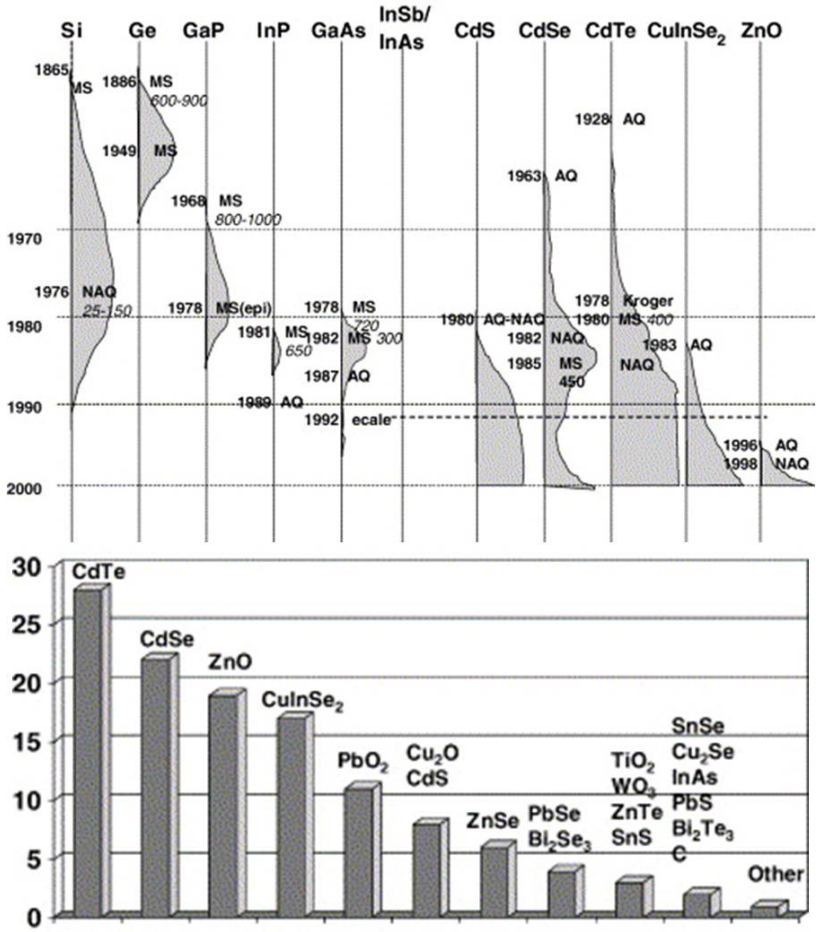

Figure 1.6 (Top) Road map of electrodeposition of main inorganic semiconductor (grey area represents the research intensity) and (Bottom) Number of published papers from Current Contents data base (from 2000 to April 2002) as a function of the nature of the semiconductor. [49]

1.3 One- Dimensional Ordered Nanoporous Templates

1.3.1 Anodization of Aluminum

Anodic oxidation is the process in which an electrochemically active species is oxidized by the passage of current or by an applied voltage in appropriate electrolytes. Anodization of aluminum was developed in the early 1900s as a method to protect aluminum from corrosion as well for dying or coloring the surface of aluminum [19], has received a lot of attentions due to a wide variety of applications, including dielectrics and more recently, nanoscience and nanotechnology [57]. Anodic oxidation is one of the techniques that can be applied to form a thicker oxide on aluminum to provide desirable properties. This is because an oxide can initially form at a rapid rate, but slow down over time to form a stable oxide film (called native oxide) of a few Å when a fresh oxide-free aluminum surface is exposed to air at room temperature.

1.3.2 Electrochemistry at the Metal-Oxide and Oxide-Solution Interfaces

During the anodic oxidation process, the aluminum serves as the anode and a chemically stable metal, such as platinum or graphite is needed as the cathode. The overall electrochemical reactions that occur during electrochemical oxidation of aluminum can be written as follows:

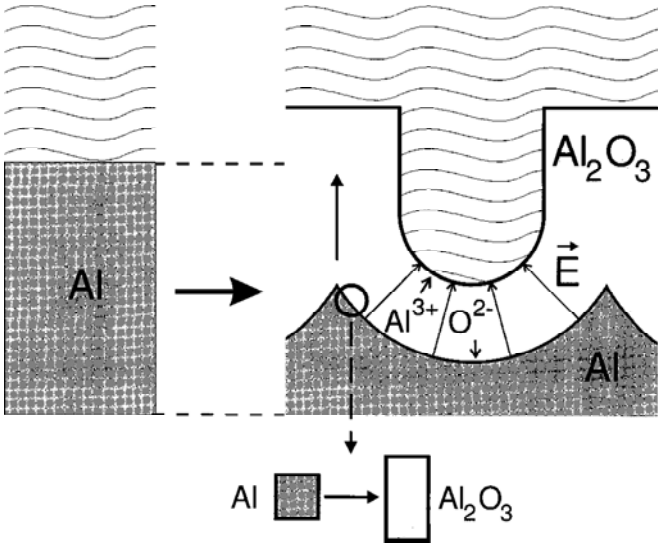

Figure 1.7. Volume expansion of aluminum during anodic oxidation. On the left the level of the unanodized metal surface is depicted [58].

Anode (oxide growth):

$$2Al(solid) + 3H_2O(liquid) \rightarrow Al_2O_3(solid) + 6H^+(liquid) + 6e^- \quad (1.14)$$

Cathode (hydrogen evolution):

$$3H^+(liquid) + 3e^- \rightarrow \frac{3}{2}H_2(gas) \quad (1.15)$$

Though the overall reactions depict a simple anodization process, the actual chemistry and reactions involved are much more complicated. For example, the electrochemically active species such as oxygen anions or hydroxyl anions and the metal cations have to diffuse and migrate through the oxide for the occurrence of subsequent oxidation. The oxidation reaction can occur at the metal-oxide interface, oxide-solution interface or somewhere intermediate in the established oxide. Other anions and water

molecules from the electrolyte can also get incorporated into the forming oxide [19, 26, 32-34, 36, 59].

1.3.3 Porous-type and Barrier-type Aluminum Oxide

Depending on several factors, in particular the electrolytes, two types of anodic films can be produced: barrier type and porous type. Barrier type films can be formed in completely insoluble electrolytes ($5 < pH < 7$), e.g., neutral boric acid, ammonium borate, tartrate, and ammonium tetraborate in ethylene glycol. Porous type films can be created in slightly soluble electrolytes such as sulfuric, oxalic and phosphoric acid [60].

Porous type Anodic Alumina: When the aluminum surface is anodized in the presence of a solution containing acids such as sulfuric (H_2SO_4), oxalic ($H_2C_2O_4$) or phosphoric (H_3PO_4) acids, self- organized nanoporous structures are formed in the anodic oxide film. As aluminum is anodized in the acidic medium, both the metal-oxide and the oxide-electrolyte interfaces become curved like spherical segments. The anodization current is observed to rise dramatically before reaching a steady-state current level until all of the aluminum has been depleted and converted into porous alumina. The pore diameter typically depends on anodization conditions, including anodization voltage, type of acid and pH value of the acid, and can range from less than 10nm to more than 100 nm, whereas length of the nanopores can be extended to the domain of micrometers, depending on anodizing time. A thin insulating oxide layer encapsulates the bottom of

each pore and is called oxide barrier layer, whose thickness can range from about 10nm to over 100 nm, and lies directly above metallic aluminum surface. At the bottom of pores, the oxide barrier layer gets continuously regenerated, as the aluminum anodizes, but it maintains small constant barrier oxide thickness.

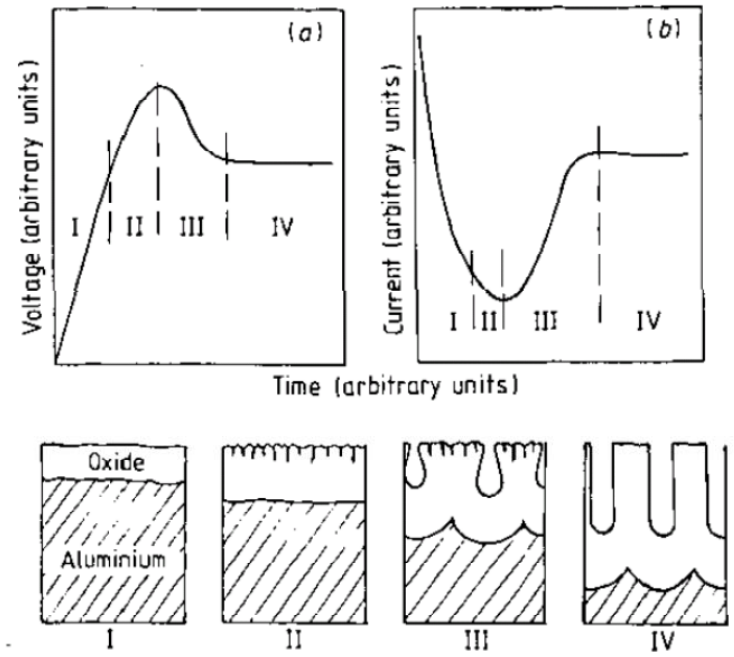

Figure 1.8 Schematics of voltage and current transient in (a) galvanostatic and (b) potentiostatic anodization.

Pore Formation Mechanisms: Current efficiency during the formation of nanoporous alumina is less than 100% (experimentally measured current efficacy under a condition is about 62% [61]) and the anodizing ratio of barrier layer of a porous oxide is about 1.2nm/V. This is smaller than that of the barrier type oxide (1.4nm/V). These phenomenological features suggest that a dynamic equilibrium during porous growth is established between film formation by oxidation at the metal-oxide interface and film dissolution at the oxide-electrolyte interface. Moreover, the chemical dissolution rate of

the oxide is shown to be several orders of magnitude smaller than the oxide formation rate in steady state during the anodization [62]. Therefore, the field- assisted dissolution model was proposed, and it was assumed that the dissolution rate of aluminum oxide was greatly enhanced due to the scalloped geometry at the presence of an electric field during the anodization. However, no theoretical models match well with experimental investigations due to the limited information on the kinetics of the field- assisted dissolution of the oxide [63]. Moreover, the low current efficiency of the anodization procedure could be understood with the direct ejection model of aluminum ions by assuming that the aluminum cation is dissolved directly into the solution [59, 64]. Such direct ejection of aluminum ions is not involved in the pore formation but is a required condition for porous oxide formation.

One investigation has elucidated the field-assisted plastic flow model in steady-state for pore formation with a tungsten tracer during anodization [65]. It visualized details of mass transport in the porous oxide films. It indicated that steady state growth of pores is maintained by plastic flow of the film growth stresses during the anodization in acidic electrolyte. Based on the distribution of tungsten tracer in the scalloped barrier layer, the pores were created mainly by the flow of materials from pore bases to cell walls in anodization without loss of tungsten tracer. However, other tracers showed experimentally different distributions from tungsten tracer in oxide. It was required to verify the oxide flow model and to determine if the field- assisted dissolution of the oxide happened during anodization.

Barrier type Anodic Alumina: Barrier type anodic aluminum oxide is formed when aluminum is anodized at the presence of solution with a pH value greater than 5 because very high efficiency of Faradaic current (close to 100%) in building the oxide through anodization is attributed to barrier type oxide film formation [66] and both the aluminum-alumina and the alumina-electrolyte interfaces remains planar. The anodizing current decays exponentially with time, which prevents from formation of pores on the oxide. This results in a nonporous insulating oxide layer formation that extends throughout surface of the exposed aluminum. In the case of barrier anodic alumina, any protons or hydrogen ions generated as the byproduct of the hydrolysis process get locally neutralized by the base. As a result this greatly thwarts growth and propagation of nanopores into the aluminum substrate. Due to the hydrogen ion neutralization reaction, when anodizing aluminum at higher pH, the electric field enhanced alumina dissolution at the electrolyte-oxide interface is absent. Therefore, this keeps formation of barrier type alumina uniform and planar.

1.3.4 Self- Ordered Porous Aluminum Oxide

In order to form ordered alumina nanoporous structures, a multistep anodization process is necessary, including a pre-treatment of aluminum foil, anodizing, and post-treatment steps. The pre-treatment procedure includes annealing of aluminum foil to increase grain size, degreasing of samples, and electro-polishing to reduce aluminum foil roughness [21].

Two- Step Anodization: The two-step anodization process has been attractive because the initial anodization at the pre-selected cell potential is typically not able to achieve straight porous structure, however, a periodic concave triangular pattern can be formed on the aluminum surface, acting as self-assembled masks for the second anodization after subsequent chemical etching of as-grown aluminum oxide layer formed in the first step of anodization. The second anodization can be carried out under the same conditions applied for the first step.

Self-ordered porous aluminum oxide shows a linear relationship between interpore distance and applied voltage and is independent on acidic anodization electrolytes under certain concentrations. Sulfuric acid and oxalic acid are suitable for the formation of template pores with diameter less than 40nm at low potentials. For the synthesis of an alumina template with bigger pore diameters, phosphoric acid is chosen.

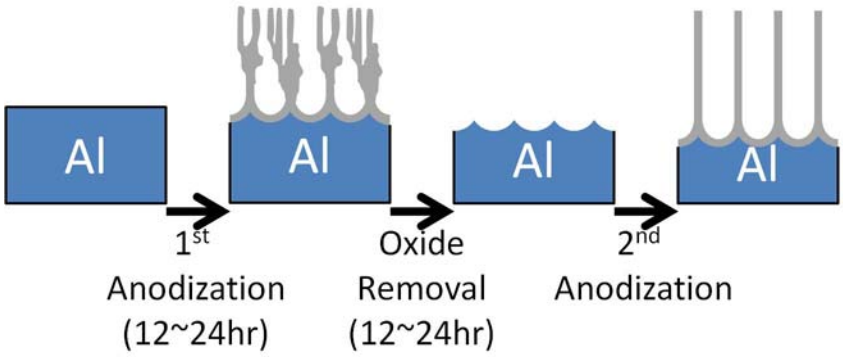

Figure 1.9 Schematics of two- step anodization of aluminum for self- ordered nanoporous membrane.

Mild and Hard Anodization: Soon after the first discovery of an ideal honeycomb porous structure with 100nm interpore distance (D_{int}) at the Al-AAO interface under the conditions of prolonged anodization in 0.3M oxalic acid at 0°C with application of a constant voltage of 40V [21], other anodization conditions that could lead to the formation of self-ordered porous structure with various D_{int} were extensively explored [50-53]. As a result, a new regime of self-organized nanoporous structure has been achieved by a long time anodization process with low concentration of acid electrolyte. These conditions were attributed to so-called "mild anodization" for the self-ordering patterns.

Recent advances in anodization of aluminum under a high anodic voltage (or high electric field) have allowed exploitation of self-ordered nanoporous AAO beyond the mild anodized patterns. After a pretreatment process involving peroxide layer formation and electrolyte aging, an extended regime of the interpore distance of self- ordered pores has been demonstrated in hard anodization conditions [67, 68]. It is worth noting that the proportionality factor in hard anodization is about 2.0nm.V while in mild anodization it is about 2.5nm.V.

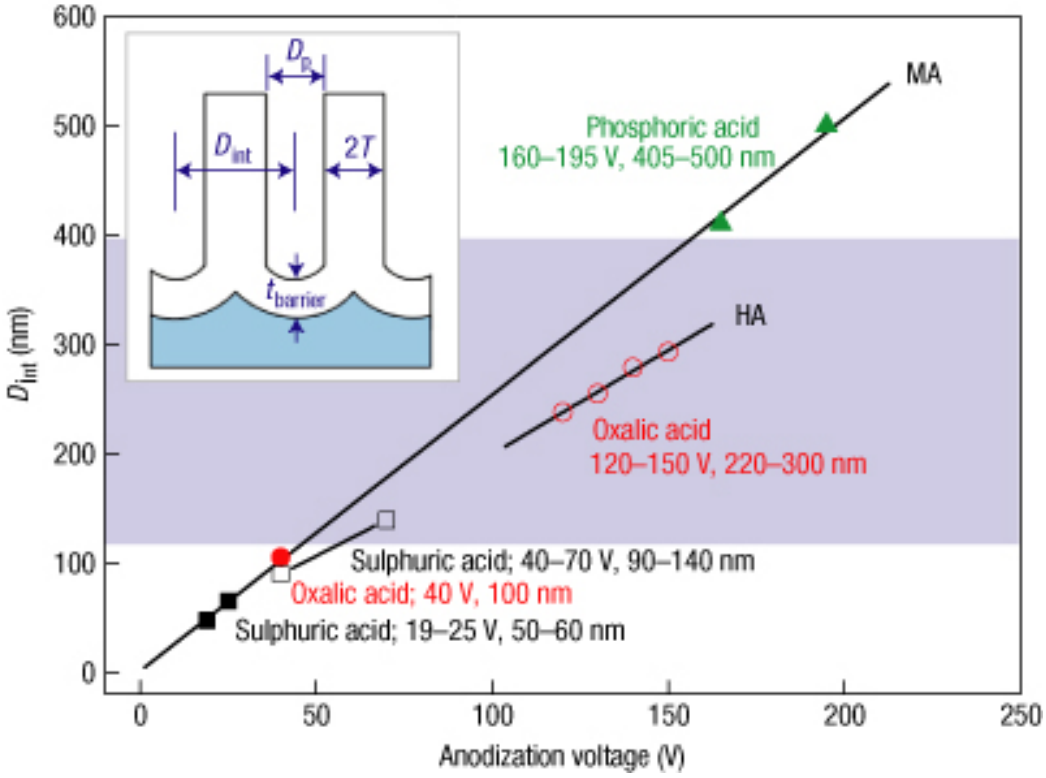

Figure 1.10 Summary of self- ordering voltages and the interpore distance in various anodization conditions [68].

1.4 Electrochemical Deposition

Increasing demand for faster, smaller, less expensive electronic systems in process technologies has driven development of high-yield, cost-effective electrochemical processing techniques, such as electrochemical deposition (also called electroplating or metallization) to manufacture a variety of microelectronic components [69]. The main advantages of electrodeposition over vacuum techniques like physical and chemical vapor deposition include room temperature operation with reduction of thermal stress, low cost of equipment without requiring high vacuum facilities, and high deposition rate with easy scalability.

Conventionally, electrodeposition has been used to grow metallic thin films on conducting surfaces. But if this growth is confined to be within nanopores of insulating templates, it can be used to fabricate 1D or 0D nanostructures, and is called as template-assisted electrodeposition. This template- assisted electrochemical deposition as a versatile method for generating many kinds of nanostructures with control of dimensions, properties, and morphology can represent a simple, low-cost and high throughput technique for fabrication of continuous metal and semiconductor nanowires with large aspect ratio in nanoscale diameter due to the unique structure of anodic aluminum oxide [54, 70-74].

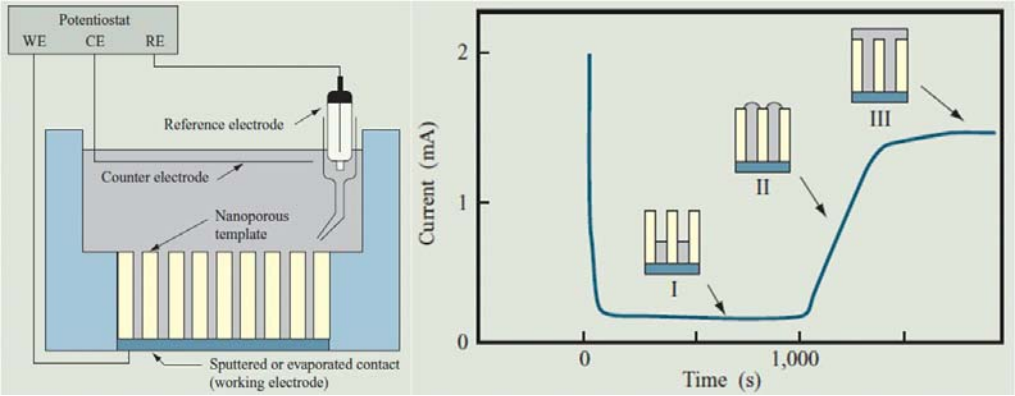

Figure 1.11. (Left) Schematic illustration of cell for electrochemical deposition of nanowires and (Right) Deposition current–time transient for template- assisted deposition

1.4.1 Thermodynamics and Kinetics in Electrochemical Deposition

Electrodeposition is the process in which metal ions are reduced from either an aqueous, organic, or molten salt electrolyte. Here an aqueous solution process is used as example.

Reduction of metal ions M^{Z+} in aqueous solution with electron deficient condition is represented by:

$$M^{Z+}{}_{solution} + Ze \leftrightarrow M_{lattice} \tag{1.16}$$

The double sided arrow shows that this reaction is reversible and is dependent on the thermodynamic conditions. This equilibrium reaction is the half cell reaction for metal ions, and the reaction in the forward direction to reduce metal ions is attributed to the supply of electron from an outside source. This means that the reduction rate has to be larger than that of oxidation under an applied potential. Electrodeposition occurs at the

metal-solution interface at the expense of dissolved metal ions from solution; the character of the interface between the metal electrode and solution is thus of crucial importance for the electrodeposition process because the potential difference is mostly attributed to the metal-solution interface, even though a typical electrochemical cell system has four different phase boundaries (i.e., two metal-solution interfaces and two metal interfaces) with the difference of Fermi levels causing the potential difference.

Double Layer Models: Three typical models have been developed for understanding charge distribution in the solution side of the metal-solution interface due to excess charge from metallic electrode: (1) the Helmholtz Model, (2) the Gouy-Chapman Model, and (3) the Stern Model [75]. The double layer in a metal-solution interface consists of two equal and opposite layers of charge. This layer is assumed as planar at fixed distance in the Helmholtz model. In this model, the double layer capacitance is determined by the dielectric constant of the electrode metal, regardless of the equilibrium electrode potential. However, a dependence of double layer capacitance on the equilibrium electrode potential was shown experimentally. Therefore, the Gouy-Chapman model employed Poisson-Boltzmann equation for the double layer distribution [76], and the electrode potential exponentially decays from the electrode into the solution with statistically distributed double charge layer and it shows that higher concentration of electrolyte results in a faster potential decay. However, highly charged double layer is not understood with this model, Stern suggested the combination of Helmholtz model and Gouy-Chapman model for so-called internal “Stern” layer (with the Helmholtz model) and an outer diffuse layer (i.e. Gouy-Chapman layer) of double layer.

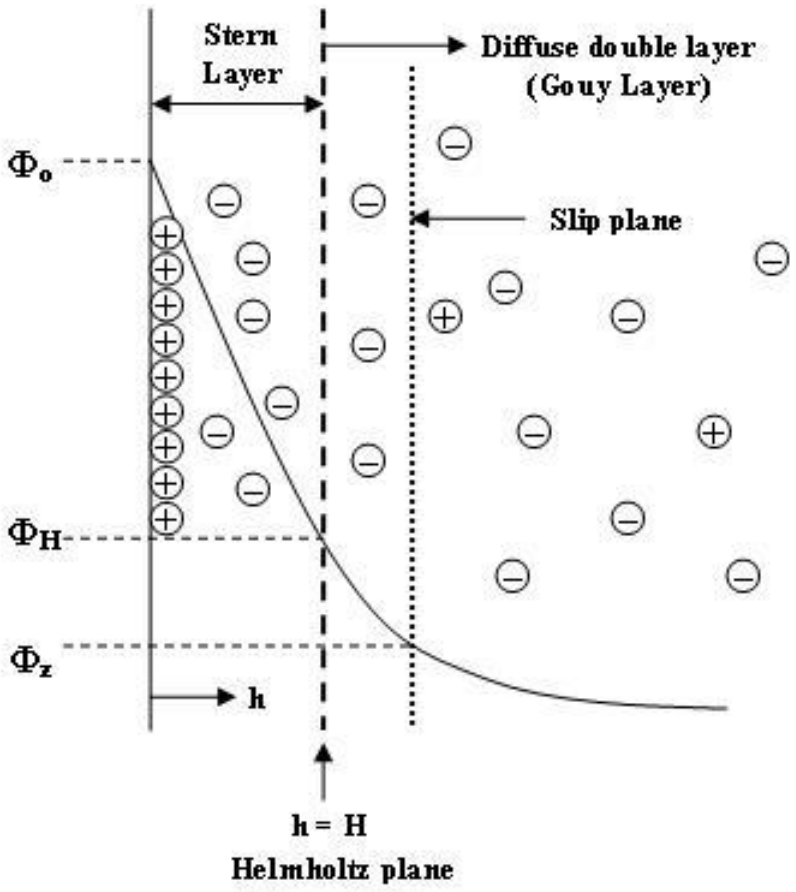

Figure 1.12 Scheme of double layer between metal electrode and electrolyte [75].

Nernst Equation and Overpotential: The standard reduction potential is measured against a standard hydrogen electrode under standard conditions (25℃, a 1M concentration for each ion participating in the reaction and a partial pressure of 1 atm for each gas). However, conditions in a real cell usually deviate significantly from the equilibrium, and the Nernst equation is used for describing the real cell potential [75].

$$E = E_0 - \frac{RT}{zF} \ln\left(\frac{a_c}{a_0}\right) \tag{1.17}$$

The new equilibrium cell potential under a given condition (depending on both temperature T and ions concentration with activity of ions at the electrode surface (a_C) and that of bulk solution(a_0)) is calculated from standard reduction potential with gas constant (R), one Faraday constant (F), and number of electrons (z) in the reaction as open circuit potential (OCP) [75]. An external potential has to be applied for continuous growth in the electrochemical deposition, and the overpotential (η) at this non-equilibrium condition is expressed by

$$\eta = E(I) - E_{Nernst} \tag{1.18}$$

The overpotential is required to overcome barriers of the overall electrode reactions and the reaction rate in the system is determined by charge transfer and mass transfer.

Charge transfer (or electron transfer) is directly determined by the electrode potential. The Butler-Volmer equation describes the relationship between the reaction rate of electrochemical deposition and charge transfer under the overpotential by

$$i = \vec{i} - \overleftarrow{i} = i_0 \left[\exp\left(\frac{(1-\alpha)zF\eta}{RT}\right) - \exp\left(\frac{-\alpha zF\eta}{RT}\right)\right] \tag{1.19}$$

where, α is the so-called dimensionless charge transfer coefficient, which is related to the activation energy, and T is the absolute temperature. The preference between reduction and oxidation is determined by the polarization of the overpotential value, and the deposition rate exponentially increases with large overpotential.

However, the process is limited by the mass transport, i.e. migration, diffusion and convection in the electrolyte, even though the deposition rate increases exponentially

as the absolute value of the overpotential increases. This is mainly related to the concentration gradient between the liquid-electrode interface and the bulk solution.

Under control of mass transport, the overall deposition rate is limited by the diffusion limited current [75]:

$$i = \frac{nFD_{M^+}C_{bulk}}{\delta} \tag{1.20}$$

where the diffusion layer thickness is given by:

$$\delta = 2\sqrt{D_{M^+}}\sqrt{\frac{t}{\pi}} \tag{1.21}$$

Therefore, charge transfer is followed by the Butler-Volmer relationship at the low overpotential, while a diffusion-limited process is dominant based on the overall current, and the charge transfer under high overpotential is constant.

1.4.2 Electrochemical Deposition Method

Constant Voltage (CV) and Constant Current (CC) Deposition: Both deposition current and working electrode potential are important parameters to determine the course of a reaction in electrochemical deposition. They can be controlled as a function of time. The deposition current is controlled in galvanostatic synthesis to form products. Constant current (or controlled current) in galvanostatic synthesis technique makes the potential the dependent variable with time. A controlled morphology with good adhesion is provided under controlled current. However, the reactant activity is

decreased by cell potential drift with time and a multiplicity of electrodeposition rate is attributed to cell potential transient.

On the other hand, potentiostatic synthesis involves the control of the cell potential. Both low diffusion rate of reactant molecules from bulk electrolyte to the electrode surface and decrease in reactant activity could cause rapid decay in the cell current as the reaction proceeds. However, a pure single phase product by the applied potential is likely to be yielded.

Direct Current (DC) and Alternative Current (AC) Deposition: A metal electrode deposited on the template is used as the working electrode in a DC deposition. However, many procedure steps are required in making the working electrode. These include removal of aluminum metal from nanoporous oxide film, removal of barrier layer by chemical etching and frangibility of the template. The complexity of these processes could easily lead to the failure of samples. On the other hand, the AC deposition could be done through as-produced template without additional process (unreacted aluminum substrate acts as one electrode). A barrier layer oxide of nanoporous template shows rectifying properties and enables electrochemical deposition by AC electrolysis [77]. The cathodical half cycle of applied AC electrodeposition voltage (or current) produces the electrodeposition at the bottom of the pores of the aluminum oxide films by reducing metal cations in the electrolyte to an oxidation-state zero. During the anodic half cycle, rectifying properties of the films and the presence of electrolyte ensure that reanodization of oxide films occurs to a greater extent than any re-oxidation of metal particle deposited

in the pores. Moreover, no separation of AAO template from the Al substrate also affords good quality filling of pores with single metals, if optimized electrodeposition conditions are used [78]. Gösele's group in Germany has recently demonstrated high uniformity of electrodeposition in the template by using current-controlled deposition sequences [45, 79, 80].

1.5 General Characterization of Nanowires

1.5.1 Transmission Electron Microscopy

In this thesis, transmission electron microscopy (TEM) has been performed extensively to characterize as-synthesized one- dimensional nanostructures. The morphology, crystallographic features, and chemical compositions of nanowires have been obtained by using both a JEOL 2100F field emission TEM and a JEOL 2100 LaB6 TEM operated at 200 KV. In the optical microscope, light is the illumination source and is focused with glass lenses, while TEMs use highly energetic electron beam source which is emitted from the filament and accelerated by a high voltage (100 kV – 1000 kV). Electromagnetic lenses (through a set of condenser lenses onto the specimen) are used for beam focusing. Atoms within the specimen scatter the electron beam and these diffracted beams are then brought to focus by the objective lens on its back focal plane and form a diffraction pattern. A final TEM image or diffraction pattern can be produced on a fluorescent viewing screen by a series consisting of the objective lens, the intermediate

lens, the projector and magnifying lenses. One- dimensional nanostructures were characterized in detail with spatial imaging and diffraction characterization including conventional imaging, phase contrast imaging (high resolution TEM), Z-contrast imaging and selected area electron diffraction (SAED). In addition, the TEM system is available with high energy electrons and thus enables electron excitation of atoms of samples. One of the spectroscopic techniques based on electron excitations is energy-dispersive x-ray spectroscopy (EDS) for chemical composition analysis of the nanostructures. Samples for TEM characterization are prepared by adding one drop of nanowires dispersion in volatile solvent onto copper grids with carbon support film. The samples are ready to be characterized after the solvent is evacuated.

1.5.2 Ultraviolet-visible (UV-vis) Spectroscopy

All the one- dimensional nanostructures were optically characterized with SHIMADZU UV-2501PC. The beam from a visible and/or ultraviolet (UV) light source is separated into monochromatic beams by a prism or diffraction grating. Each monochromatic beam in turn is split into two equal intensity beams by a beam splitter. One beam, called the sample beam, passes through a small transparent container (cuvette) containing a solution of NPs in a transparent solvent. The other beam, called the reference beam, passes through an identical cuvette containing only the solvent. Both the intensities of these light beams are then measured by light detectors and compared. In our measurement, the UV scan region is normally from 200 to 400 nm, and the visible

portion is from 400 to 800 nm. Absorbance cuvettes have 10mm path length, PMMA materials (PLASTIBRAND® standard disposable cuvettes, Useable wavelength > 300 nm) and contain 1.5 ml sample chambers. This measurement for 1D nanostructures was performed in the range from 300nm to 900nm.

1.5.3 UV-vis-NIR Spectrophotometer

Optical features of noble metal nanowires in near infrared regime were also monitored by UV-vis-NIR absorbance spectroscopy using a PerkinElmer LAMBDA 1050 UV/Vis/NIR Spectrophotometer, in which a double-beam mode is applied and the spectra data were baselined to the spectrum of 99.99% chloroform solvent. Extinction measurements could be taken at wavelengths <3000nm. Absorbance cells are single crystalline quartz with 3.5mm path length, (Infrasil® Quartz or equivalent, useable range: 220 to 3800nm, Starna Cells, Inc.). All noble metal nanowires were capped with alkanethiols in order to achieve a good dispersion in the chloroform solvent.

1.5.4 SQUID Magnetometer

SQUID or Superconducting Quantum Interference Devices are very sensitive magnetometers used to measure extremely small magnetic fields, based on superconducting loops containing Josephson junctions. A commercial SQUID machine

from Quantum Design (MPMS XL model) was used for this thesis study and it has the following features: AC Susceptibility Measurement from - 0.1 Hz to 1K Hz with the sensitivity as 2 x $l0^{-8}$ emu at 0 T; Ultra-Low Field Capability from ± 0.05 G for the 7 T magnets; Reciprocating Sample Option (RSO)-DC Magnetization absolute with the sensitivity as 1 x 10^{-8} emu at 2,500 Oe and Continuous Low Temperature Control/Temperature Sweep Mode (CLTC) with the Sweep rate as 0.001 ~ 10 K/min. The nanowires embedded in AAO template sample kept in a lock-ring capsule for magnetic characterization.

Chapter 2: Self- Ordered, Controlled Structure Nanoporous Membranes Using Constant Current Anodization

In this chapter, I will present a constant current (CC) based anodization technique and demonstrate its use to fabricate and control structure of mechanically stable anodic aluminum oxide (AAO) membranes with long- range self- ordered hexagonal nanopore pattern in a highly controlled manner. For the first time the interpore distance (D_{int}) of a self-ordered nanopore array can be continuously tuned over a broad range with CC anodization. It is uniquely defined by the conductivity of sulfuric acid as electrolyte. This technique can offer new degrees of freedom for engineering planar nanopore structures by fine tailoring of the CC based anodization process. These results not only facilitate further understanding of self-ordering mechanism of alumina membranes but also provide a fast, simple (without requirement of pre-patterning or pre-oxide layer), and flexible methodology for controlling complex nanoporous structures, thus offers promising practical applications in nanotechnology, including the fabrication of complex functional one- dimensional nanowires nanostructures.

2.1 Introduction

Self- ordered AAO membranes with hexagonal arrangements of nanoscale pores represent important and versatile nanostructures for a variety of applications, while simplicity and a high degree of control of nanopore arrays is crucial [50, 69, 81-86].

Current fabrication techniques mainly rely on constant voltage (CV) anodization process. In conventional CV process, self- ordered AAO films can only be achieved for several specific interpore distances (D_{int}) with the proportionality constant (defined as the ratio of D_{int} to applied voltage) ξ_{MA}=2.5nm/V (termed "mild pattern") by a two- step procedure [82, 87]. While flexibility in controlling AAO membranes with large D_{int} has been demonstrated when combined with pre-textured surfaces [88, 89], this type of anodization typically requires long processing time (up to a few days) in order to promote highly organized pore structures and/or sophisticated lithographic techniques. More recently, alternative CV approaches with low working temperature and high current densities have shown promise to expand the self- ordered regime with a shorter process time (a few hours), possessing distinct proportionality constant as ξ_{HA} =2.0nm/V (termed "hard pattern"); however, it requires pre- treatments of the samples, such as the formation of a thick uniform pre-oxide layer on the surface, in order to suppress breakdown effects as well as inhomogeneous growth [13, 68, 90]. Existence of a pre-oxide layer might pose challenges to achieve very small D_{int}, and the corresponding harsh anodization condition could also lead to poor mechanical properties of AAO films [91]. On the other hand, studies of self- ordered AAO membranes prepared from constant current (CC) based anodization have been lacking. While an attempt was recently reported to fabricate a novel AAO membrane with six- membered ring symmetry [92], there is no further control on the regular hexagonal nanoporous structure with long- range order as achievable from CV based anodization. One major reason is because it is difficult to retain stable anodic voltage during CC process, which is believed to be critical for self-ordered nanoporous structure [93-95].

2.2 Experimental Approach

2.2.1 Materials and Facilities for Anodization

Aluminum foils (99.999%, 326852, Sigma- Aldrich) are used as received without annealing. Before CC anodization, aluminum foils are electrochemically polished in a 1:4 mixture solution of 70% perchloric acid and 99.5% ethanol at 5°C for 3mins. No other pre- anodization or pre- treatment steps are required for CC process.

A typical CC anodization is carried out in a home-made glass cell with sample located in the side- wall configuration. The whole glass cell is placed on top of a stirring hot plate to agitate the electrolyte vigorously as well as to control electrolyte temperature during the anodization process. The sample temperature is controlled independently by thermally contacting with a thermoelectric solid state plate (MPA250-12, Melcor Corp.) equipped with a commercial temperature controller (MTTC-1410, Melcor Corp.). With this system, it is possible to maintain constant sample temperature with a preset value and to remove a large amount of heat efficiently due to applied high anodic current. A graphite plate is used as a cathode. The whole CC anodization process typically only takes about 15-20mins, which is much faster than the conventional CV anodization process.

2.2.2 Characterization Techniques

In order to get detailed structure of AAO membrane, high resolution TEM (JEOL 2100 LaB_6) and field emission scanning electron microscopy (SEM) (Hitachi SU-70) are applied. For TEM specimen preparation, the oxide layer from CC anodization is removed with a mixture solution of 1.8 wt% chromic acid and 5 wt% phosphoric acid for 6h. The resultant self- ordered pattern can then be transferred to the aluminum surface. In order to make a thin TEM sample, this patterned aluminum is continuously anodized under CV with either 0.3M oxalic or 5wt% phosphoric acid (anodic voltage applied at this step is the same as the plateau voltage established in the CC process). A free standing AAO membrane is thus obtained by removing residual aluminum metal with saturated mercury chloride and attached to a TEM copper grid. No further widening process is performed for all the samples. For SEM specimen preparation, a thin carbon film (~10nm) is typically evaporated on the surface of an AAO membrane in order to reduce charge accumulation due to poor conductivity of oxide.

2.3 Results and Discussion

2.3.1 Constant Current Anodization

Figure 2.1(a) highlights typical voltage characteristics with time in CC anodization process with 6M pure sulfuric acid (H_2SO_4), which shows a dramatic difference from previous CC anodization studies [92, 96]. Evolution of the anodization voltage can be clearly divided into four different stages: (1) the voltage slowly arises with time (the initial to point *i*); (2) the voltage sharply increases to a maximum (points *i* to *ii* to *iii*); (3) the voltage suddenly drops to a lower voltage (points *iii* to *iv*); and (4) the voltage maintains at a stabilized value (defined as "plateau voltage"). Existence of a plateau voltage in our CC anodization process suggests that optimum self- ordering condition of high field and high current density can be simultaneously achieved under our conditions. A large scale transmission electron microscopy (TEM) image of AAO template resulting from such a CC anodization process is shown in Figure 2.1(b). The typical domain size in the self- ordering regime is ~2-3 μm, which is comparable to that from CV anodized samples, however, considering that there are no pretreatments (such as annealing) in all our samples, the domain size observed here should be considered as a minimum estimate. A well- organized hexagonal cell feature is also evident by Fast Fourier Transformation (FFT) of one single domain (inset of Figure 2.1(b)), and further revealed in the high resolution TEM image (Figure 2.1(c)) as well as a direct bottom view of AAO sample after CC anodization (Figure 2.1(d)). AAO membranes as prepared from

this CC anodization are found to be mechanically stable without any crack, which suggests that our CC anodization is a rapid self-equilibrium process.

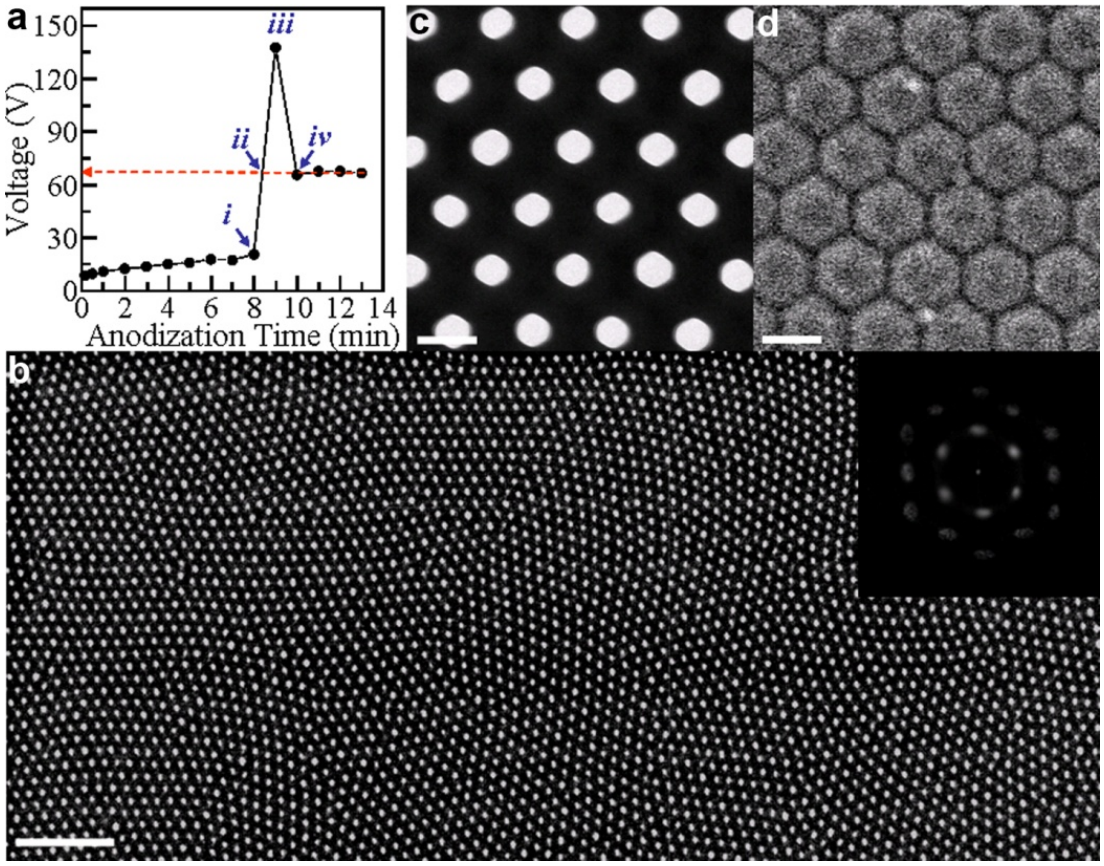

Figure 2.1 Self- ordered AAO membrane fabricated by CC anodization process. (a) Typical voltage – time characteristics under CC anodization condition with 6M sulfuric acid. Current density, 105 mA/cm^2; Electrolyte temperature, 20°C; Sample temperature, 30°C. Red dashed arrow highlights constant plateau voltage achieved in this process. Points (*i*) - (*iv*) feature critical transition stages during the CC anodization process. (b) Large scale TEM image of AAO membrane fabricated from a, showing long ranged ordering and domain structure. Scale bar: 1μm. Inset represents two- dimensional FFT of one selected single domain, featuring high hexagonal ordering of as-fabricated AAO membrane. (c) High resolution TEM image of fabricated AAO membrane. Scale bar: 100nm. (d) Field emission SEM image of bottom view from the barrier layer side fabricated from a. Scale bar: 100nm.

Our observed voltage- time characteristics are distinct from all previous CC studies, and can be attributed to the constant sample temperature control during the whole anodization process as well as the applied high current density. It has been found that anodization is typically accompanied with a large evolution of heat in the solution bath as well as inside the nanopores even under vigorous stirring, leading to some abnormal temperature dependence [66]. Our direct control of sample temperature can avoid this issue and ensure CC anodization proceeds under thermostatically conditions, which is found to play a critical role in governing the voltage evolution. Only a range of sample temperature can offer characteristic voltage- time dependence as in the Figure 2.1(a) and Figure 2.2.

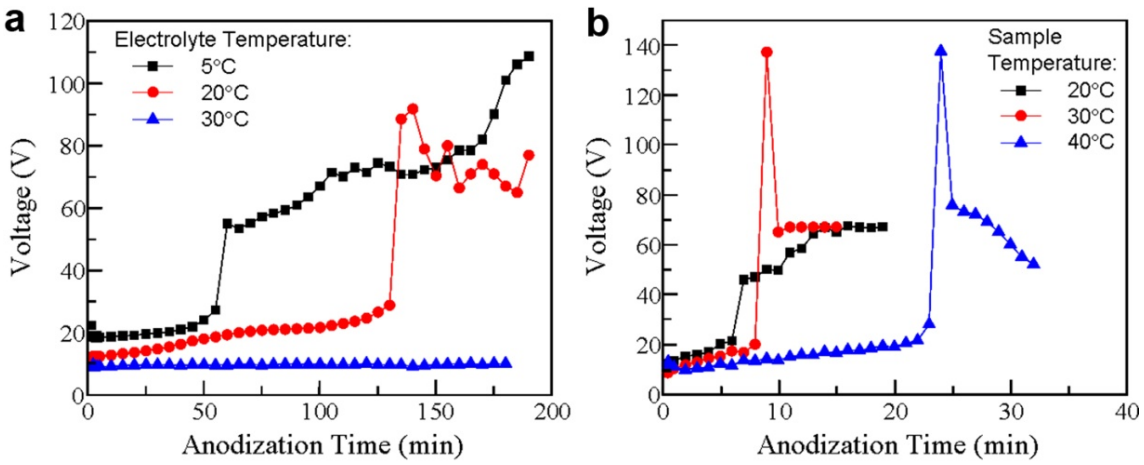

Figure 2.2 Effect of sample temperature control. (a) CC anodization process without sample temperature control. Current density, 47.2mA/cm^2. (b) CC anodization process with feedback control of constant sample temperature. Other than sample temperature, anodization condition remains the same for all the curves: Current density, 105mA/cm^2; Electrolyte temperature, 20°C; Concentration of H_2SO_4: 6M.

While the nature of porous oxide growth is still not unambiguous, it is generally believed to involve two competing processes: oxide formation at the metal-oxide

interface and oxide dissolution (both chemical dissolution and field- assisted dissolution). [93] As compared with previous CC anodization under the same acid concentration but with smaller applied current density [97], the voltage ramping rate at the initial stage (up to point *i*) is ~0.04V/s, which is much smaller than former value of 0.8V/s and suggests that chemical dissolution (determined by stable sample temperature) of the barrier oxide layer is much more significant in our process. This leads to the uniform porous oxide film growth at lower voltage, which can suppress local catastrophic events (such as breakdown) frequently observed at high fields and perform as a protective oxide layer [98]. Subsequently, as the voltage develops continuously, more oxygen related ionic species (O^{2-}, OH^{-}, SO^{4-}) from the electrolyte can be transported inward and react with aluminum, leading to an extremely rapid and homogeneous film growth (points *i*-*ii*-*iii*). At the maximum voltage, field- assisted dissolution is significantly enhanced and the voltage drops correspondingly due to the barrier layer thinning and homogeneous nucleation of pores (points *iii*-*iv*). The steady- state evolution of the ordered porous structure at high current density can thus be achieved from the dynamic equilibrium between oxidation and dissolution process, as evidenced by the existence of plateau voltage after point *iv* in Figure 2.1(a). Our CC anodization process offers big advantages over other anodization processes in that it is a fully self- adjusting process (thus the procedure is considerately simplified) and the overall processing time is greatly reduced due to applied high current density.

Importantly, we observe that the plateau voltage shown in Figure 2.1(a) only depends on the concentration of acid electrolyte, as shown in Figure 2.3 and Figure 2.4, and similar voltage characteristics and self- ordered patterns can be obtained for different

concentrations of H_2SO_4, as summarized in Figure 2.5(a) and Figure 2.6. The maximum D_{int} of 130nm obtained with pure H_2SO_4 CC anodization occurs at 8M, and the D_{int} tends to decrease as concentration decreases or increases. In order to compare with CV anodization processes, we further define the proportionality constant ξ_{CC} of CC anodized alumina membrane as the ratio of D_{int} to the plateau voltage, and summarize results in Figure 2.5(b). Our results suggest that the self- organization of nanopores achieved here agrees well with the hard pattern in the CV anodization. This is consistent with a previous suggestion that high mechanical stress due to rapid oxide formation results in small cell size in order to enlarge the surface area of the metal-oxide interface [68].

2.3.2 Understanding CC Anodization

In order to understand the novel tunability of D_{int} by acid electrolyte concentration, we compare it with the room temperature conductivity of H_2SO_4 in Figure 2.5(a). The overall tendency of conductivity variation on electrolyte concentration is comparable with that of the D_{int}. Qualitatively, the conductivity of electrolyte relates directly to the rate of the migration of oxygen ionic species across the barrier layer, therefore, the increase of conductivity (for example, due to the increase of electrolyte concentration) results in an increase in the barrier layer thickness and thus a higher plateau voltage under CC conditions. At the very high concentration of pure sulfuric acid, the conductivity decreases because there is not sufficient water present to ionize the electrolyte and therefore the anodized barrier layer becomes thinner [62]. The discrepancy between the

maximum room temperature conductivity and at the maximum D_{int} can be attributed to fact that the local electrolyte temperature near the bottom of nanopores is above room temperature due to the higher sample temperature (above 40°C). In particular, higher electrolyte temperature (up to 60°C) was applied with higher concentration of sulfuric acid as shown in Figure 2.6 and it could lead to a shift of maximum conductivity to higher concentration [62]. The relationship between conductivity and D_{int} is further confirmed by one of our control experiments, using aluminum sulfate to adjust the conductivity of sulfuric acid with the same acid concentration in Figure 2.7. We clearly observe a rise of plateau voltage as the concentration of aluminum sulfate increases, which can be attributed to the thicker barrier layer enabled by enhanced ionic transport towards oxide-metal interface with the addition of aluminum sulfate under the CC condition.

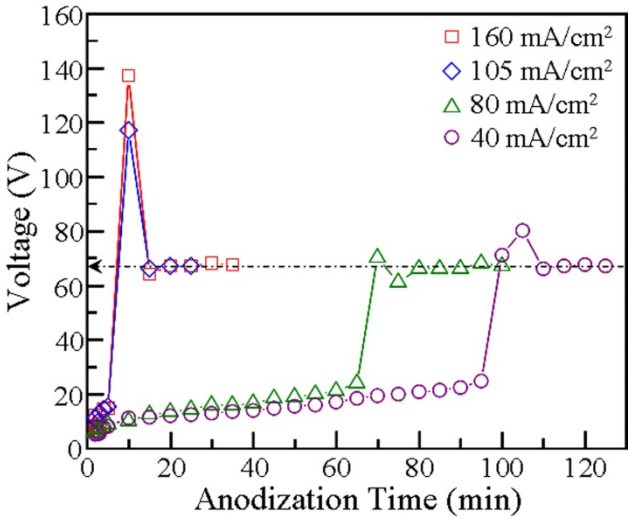

Figure 2.3 Independence of CC anodization plateau voltage on current density. Other than current density, anodization condition remains the same for all the curves: Electrolyte temperature, 20°C; Sample temperature, 30°C; Concentration of H_2SO_4: 6M.

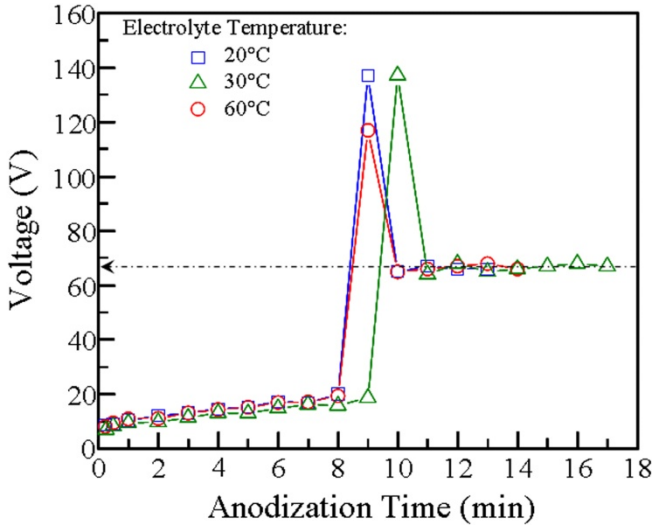

Figure 2.4 Independence of CC anodization plateau voltage on electrolyte temperature. Other than electrolyte temperature, anodization condition remains the same for all the curves: Current density, 105mA/cm^2; Sample temperature, 30°C; Concentration of H_2SO_4: 6M.

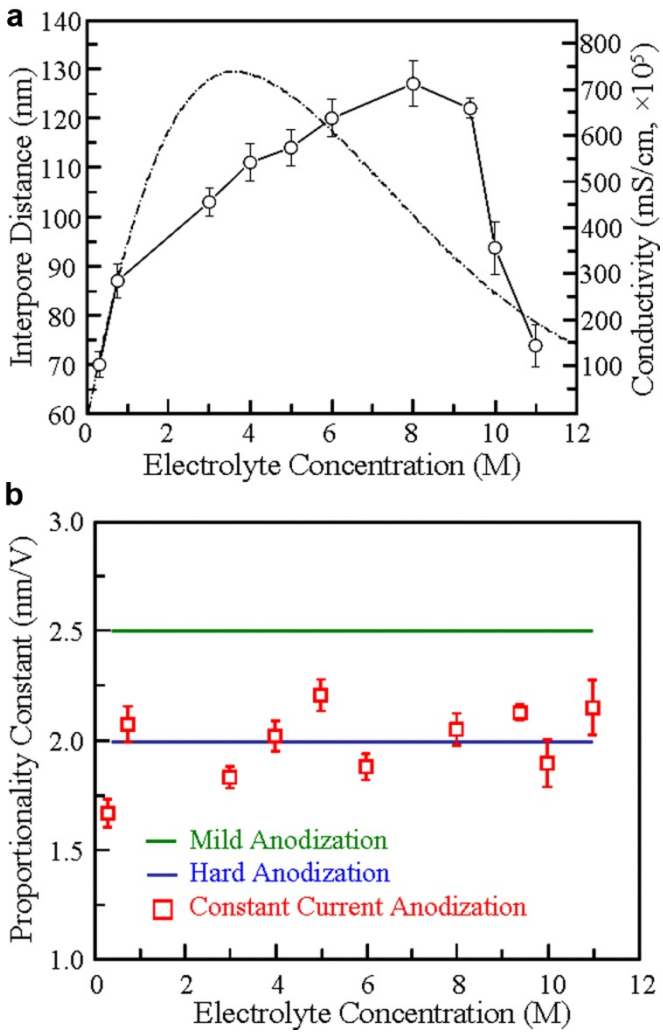

Figure 2.5 The effect of acid concentration on self- ordered nanopore structure in the CC anodization. (a) Dependence of D_{int} on the concentration of pure H_2SO_4. For comparison, room temperature conductivity vs. H_2SO_4 concentration is also presented (dash-dot curve) [62]. (b) Summary of proportionality constant ξ_{CC} of CC anodized alumina membrane fabricated under different H_2SO_4 concentration. For comparison, green and blue lines highlight two distinct ξ_{CV} observed in CV mild and hard anodization, respectively [68, 82].

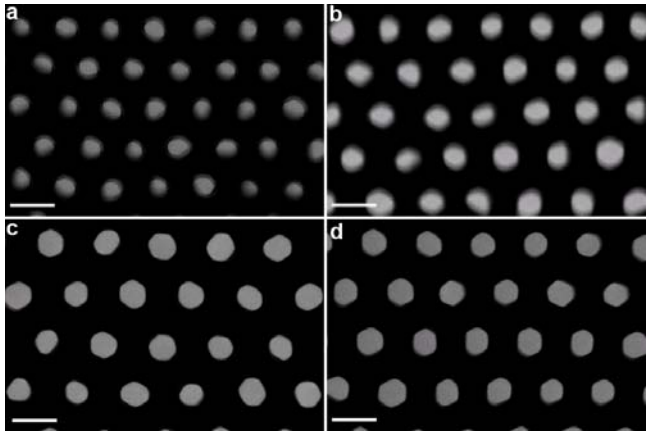

Figure 2.6 TEM images of AAO membrane obtained with different H_2SO_4 concentration. (a) 3.0M (200mA/cm^2, 20°C), (b) 5.0M (150mA/cm^2, 20°C), (c) 8.0M (100mA/cm^2, 50°C), and (d) 9.4M (110mA/cm^2, 60°C). Scale bars, 100 nm.

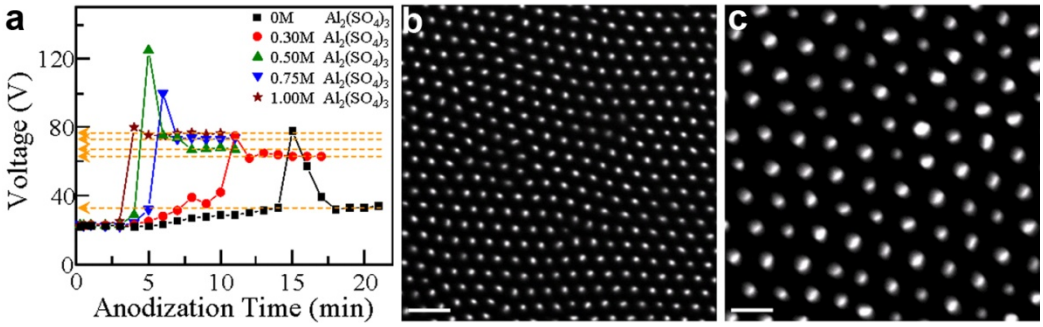

Figure 2.7 Tuning conductivity of electrolyte as well as plateau voltage by addition of $Al_2(SO_4)_3$ to 0.75M H_2SO_4 under 210mA/cm^2 at 20°C. (a) Different voltage- time characteristics with various additions of $Al_2(SO_4)_3$. Plateau voltage increases with the increase of $Al_2(SO_4)_3$ concentration. (b) and (c) are selected TEM images of AAO membrane prepared without and with addition of 0.75M $Al_2(SO_4)_3$, respectively. Scale bars, 200nm.

2.3.3 Manipulated Nanoporous Structure Membrame

The existence of characteristic transition points (points *i*, *ii*, *iii* and *iv*) in the anodization voltage evolution represents various development stages of oxide films during anodization and can be manipulated by different experimental conditions. This enables flexibility to tune finely the nanoporous array structure of an AAO membrane, which cannot be achieved with the CV process. Figure 2.8(a) highlights two examples. We observe that maximum voltage (at the point *iii* in Figure 2.1(a)) can be tuned by changing the sample temperature. The only difference in experimental conditions between the top characteristic curve of Figure 2.8(a) and that of Figure 2.1(a) is that sample temperature is reduced from 40°C to 20°C at the point *i* and maintained at 20°C for the rest of anodization process, which brings maximum voltage down close to the plateau voltage. As a result, a mild pattern with D_{int}=160nm is obtained (Figure 2.8(b)) under the same plateau voltage realized in Figure 2.1(a). The resultant mild pattern under such condition might be related to suppression of dissolution rate (thus thicker barrier layer) due to low sample temperature. Furthermore, an intriguing planar hybrid pattern is observed if the CC process is converted to CV anodization at the point *ii* while keeping rest of anodization condition the same as that of Figure 2.1(a). Figure 2.8(c) and the inset clearly show co-existence of domains with two different D_{int} of 120nm and 160nm, respectively. While more detailed experiments are necessary to provide further control, our results offer a simple method to achieve planar structural engineering of such AAO template, which has been lacking so far. Combined with recent progress of modulation of nanopore structure along vertical pore growth direction [68, 82], it should offer a

promising opportunity to achieve truly three- dimensional structural engineering of AAO templates, thus might be important for applications in the field of sensors, plasmonics and photonic crystals.

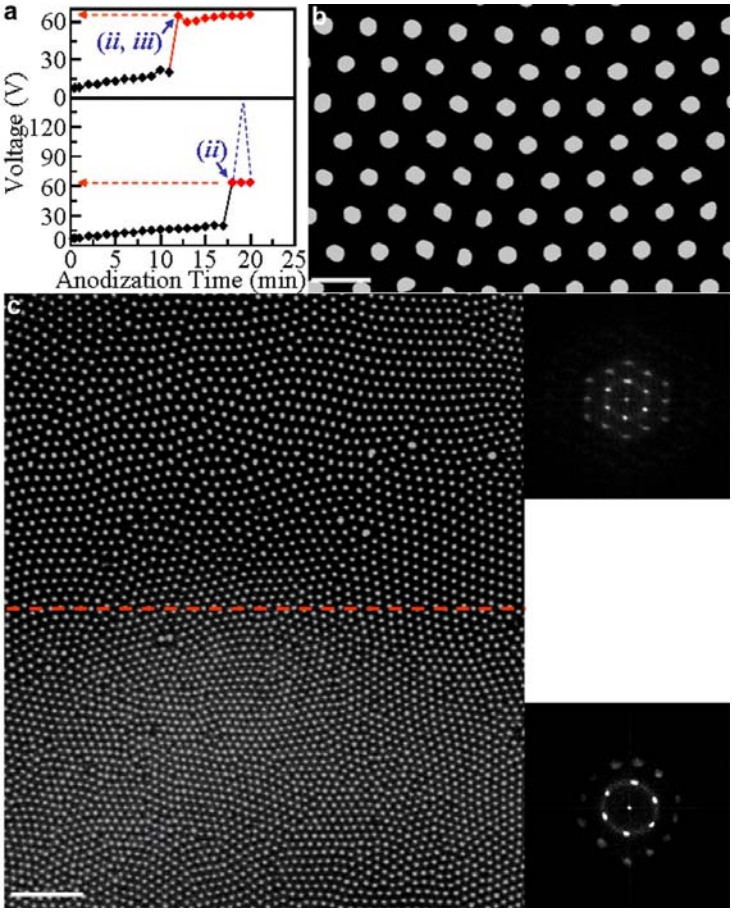

Figure 2.8 Manipulation of planar nanoporous structures. (a) Voltage-time characteristics show two different controls of CC anodization process under 105mA/cm^2. Top (mild pattern): experimental condition remains the same as that of Figure 2.1(a) except that sample temperature was reduced from 40°C to 20°C after (*i*), thus leading to the coincidence of points (*ii*) and (*iii*). Bottom (hybrid pattern): experimental condition remains the same as that of Figure 2.1(a) except that CC process is replaced with CV process (at the plateau voltage; 67V) right after point (*ii*). (b) TEM image of AAO membrane fabricated from top process of (a), showing mild pattern with D_{int}=160nm. Scale bar: 200nm. (c) Left: TEM image of AAO membrane fabricated from bottom process of (a), showing hybrid mild-hard pattern with two distinct D_{int} of 160nm and 120nm, respectively. Pattern boundary is highlighted by a red dashed line. Right top: FFT of one selected single domain of mild pattern. Right bottom: FFT of one selected single domain of hard pattern. Scale bar, 1μm.

2.3.4 Combination Anodization

The D_{int} in our CC anodization with pure sulfuric acid is uniquely defined by the plateau voltage and determined by the conductivity of electrolyte. However, we observe that this D_{int} can be further tuned within a certain range (while maintaining long ranged hexagonal ordered pattern) if the CC anodization is replaced by CV anodization immediately after point *iv* (Figure 2.1 (a)). Figure 2.9 (b) and Figure 2.9 (c) show hexagonal nanopore array with different D_{int} equal to 143 and 109 nm, respectively, which are achieved by simply applying a constant voltage at 80V and 50V right after point *iv* in the Figure 2.1(a), respectively. While the mechanism behind this requires more controlled experiments, we believe that at point *iv* the CC process might already create local pattern with periodic nucleation sites in Figure 2.10, and the following up growth of pores under different voltage behave as branching method in traditional CV anodization [99, 100]. Such a combination of CC and CV anodization processes further expands the tunable range of D_{int} in pure CC anodization and makes it possible to achieve nanoporous structures that could be challenging with conventional techniques. For example, formation of AAO with small D_{int} has been difficult to achieve through self- organized process in CV anodization. Masuda *et al* recently reported ordered AAO patterns with D_{int} less than 50nm fabricated under harsh conditions of extremely high electrolyte concentration and temperature[101]. Enabled by our combinatorial CC-CV technique as described in the Figure 2.9(a), Figure 2.9(d) demonstrates one example with D_{int}= 46 nm, which is obtained with very low concentrated sulfuric acid of 0.75M.

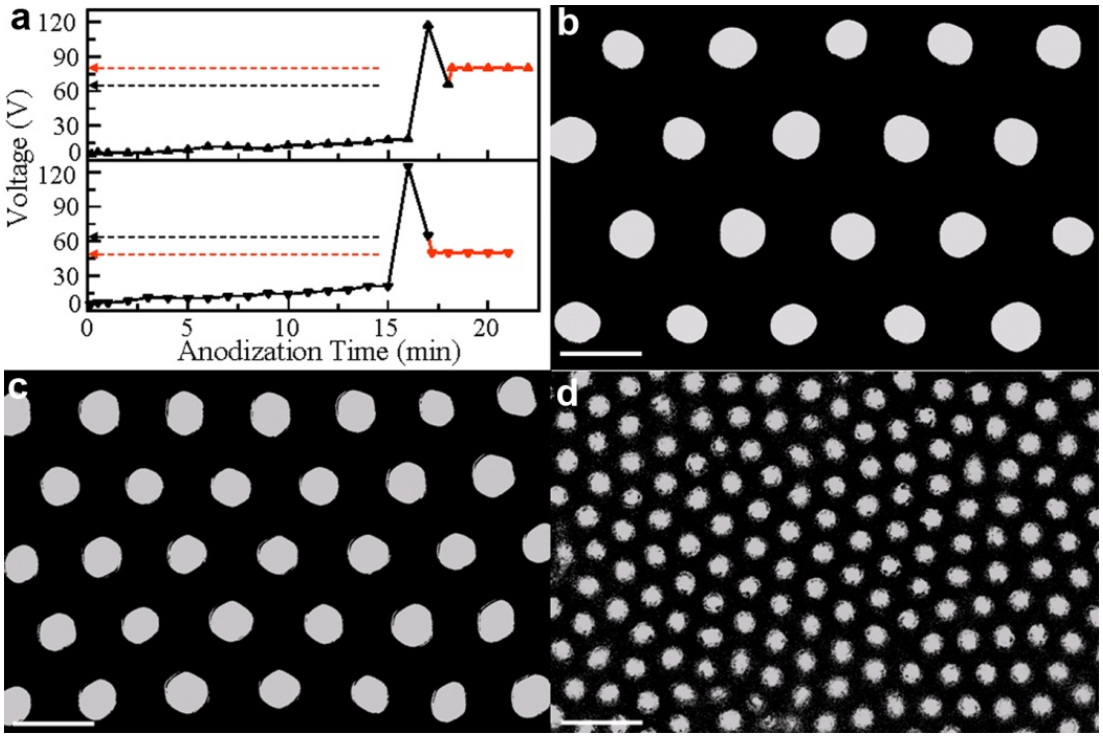

Figure 2.9 A novel combination of CC and CV anodization processes. (a) A typical combination of CC and CV anodization is shown to switch CC mode to CV mode right after point (*iv*) in Figure 2.1(a), while maintaining the same sample and electrolyte temperatures, as exemplified by two selected voltage- time evolutions. Final voltages of top and bottom curves are 80V and 50V, respectively, which are highlighted by red dashed arrows. Black dashed arrows represent plateau voltage of CC process at point (*iv*), which is 67V for 6M H_2SO_4 under 105mA/cm^2. (b) and (c) TEM images of AAO membranes fabricated from top and bottom processes of (a), respectively. Scale bars, 100nm. (d) TEM image of AAO membrane with D_{int}=46nm, which is fabricated by applying constant voltage of 18V immediately after point (*iv*) of CC process with 0.75M H_2SO_4 and 55°C of sample temperature. Scale bar, 100nm.

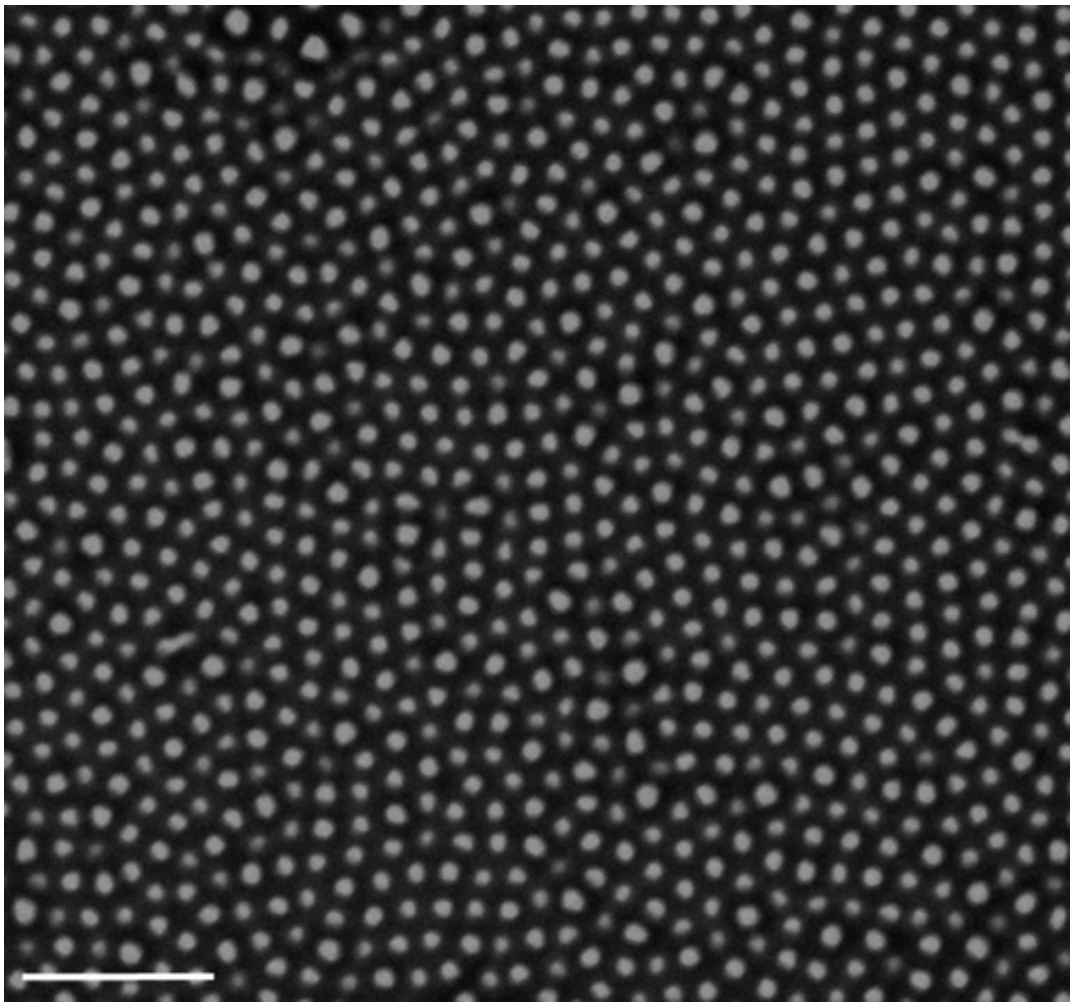

Figure 2.10 TEM image AAO membrane at point (*iv*) in the Figure 2.1(a). Local ordering of porous structure can be observed. Continuous CC anodization with the plateau voltage could reduce defect density and further provide membrane with long ranged ordering as the image shown in the Figure 2.1(b). Scale bar, 500nm.

2.4 Summary

Our CC anodization method offers advantages over traditional CV anodization process, and opens up exciting opportunities, ranging from fundamental understanding of self- ordering mechanism of nanoporous AAO membranes to practical technological applications of using CC anodization. For example, the faster and simpler CC process, as compared with conventional CV anodization, makes it feasible to be adapted for industry, especially considering that sulfuric acid has been widely applied in industrial anodization process. Nanopore size is continuously tunable over a broad range with long ranged self-ordered pattern. Furthermore, our results show that voltage evolution during the CC process experiences different critical stages (points *i*, *ii*, *iii* and *iv* in Figure 2.1(a)), indicating different features of anodic formed oxide layer. Therefore more detailed structural and compositional characterizations at different stages should provide a full picture of self- ordering mechanism of general anodization process. Importantly, our CC process is very flexible and offer various opportunities for controlling the structure of an AAO template, thus leading to potential realization of three dimensional complex nanostructures that is important for the field of nanotechnology.

Chapter 3: Template- Assisted Electrochemical Depositions for Functional One- Dimensional Nanostructures

In this chapter, high quality and well- controlled one- dimensional functional nanostructures by template- based electrochemical depositions for pure semiconducting, metallic, magnetic materials and their heterostructures will be addressed.

3.1 Introduction

Recently, studies of one- dimensional (1D) nanostructures have drawn much attention, because of the potential applications of 1D nanostructures in advanced electronics, optoelectronics, catalysts, chemical sensors and magnetic data storage [10, 102-104]. As the device dimensions are scaled down to the nanometer region, advanced nanoscale fabrication technology should play a key role in the future applications of nanodevices. Therefore, many recent research efforts have been dedicated to large-scale synthesis, quality control and functionality integration of 1D nanostructures. Among these approaches, electro- and electroless- chemical deposition of target materials in conjunction with removable nanoscale templates technique represent the most promising synthetic routes for functional 1D nanostructures.

Among all the nanoscale templates that have been explored, the anodic aluminum oxide (AAO) membrane represents the most promising template that can be used as

sacrificial templates because they possess tunable regular nanoporous structures with high pore densities, high aspect ratio, and good thermal stability [54, 73, 105]. In addition, the AAO membrane can be easily removed after a pore-filling process by chemical etching. The combination of electro- and electroless- chemical deposition with AAO templates should offer a low-cost, high-throughput, and effective technique for producing desired 1D nanostructures within the pores of the AAO templates.

As already elaborated in Chapter 2, many studies on anodization of aluminum have moved from the industrial process for protecting, strengthening, and coloring aluminum for several decades to the formation of self-organized nanoporous templates [59]. It has been found that pore diameter and pore density are tunable and dependent upon applied potential, temperature, and electrolyte. However, only limited conditions are available to form uniform, cylindrical, hexagonally ordered pores using conventional anodization techniques, and two- step anodization process or pre-patterned aluminum surface is typically required [66, 87, 106]. Such limitations can be overcome by our new constant current anodization technique, presented in Chapter 2.

For electrochemical deposition with an AAO template, direct current (DC) electrodeposition has been demonstrated to be a particularly powerful technique in terms of substantial controls over composition and crystallinity [107] and easy access to compositional modulation along the axis of nanowire [67]. However, it is unlikely that the DC electrodeposition techniques are amenable to industrial scale processing because of the requirement of laborious preprocessing before deposition, including removal of any remaining aluminum substrate, chemical opening of the ends of the pores and deposition of a conducting layer as working electrode on one end of the AAO template

[67, 107, 108]. Such redundant processing requirements are attributed to the existence of oxide barrier layer on the pore bottom. Recently, a new technique was reported: gradually reducing the applied voltage immediately after anodization to thin down the barrier layer so that DC electrodeposition can be employed without complete removal of aluminum substrate [109]. However, the barrier layer thinning process is also very time-consuming and it is hard to achieve a homogeneous barrier layer with reduced thickness.

On the other hand, alternating current (AC) deposition techniques with AAO templates are preferable to develop a nanostructure with fewer processing steps. They are more reliable for scale-up, and can produce nanowires without the requirement of a barrier layer thinning process. However, this technique provides relatively less control over the 1D nanowire structure, as compared with the DC method, due to the electrical rectifying behavior of barrier layer.

3.2 Experimental Approach and Materials

3.2.1 Preparation of self- organized nanoporous aluminum oxide template

Anodization of Aluminum (for both AC and DC depositions): High-purity aluminum foils were commercially available (Alfa Aesar, Al foil, 2.5 mm/0.10 in. thick, Puratronic 99.997% metal basis, 100×500 mm^2), and were annealed at 500 °C in a nitrogen atmosphere for 4 hours to increase the grain size. Then electro- polishing with mixture of ethyl alcohol (C_2H_5OH) and perchloric acid (70% $HClO_4$) with 4:1 volume

ratio was followed at the temperature below 5°C and under 20V DC for 3~4 minutes were used to realize a mirror- like surface. For highly ordered porous aluminum oxide templates, AAO was produced using a two- step anodization under two different conditions. The Al was first anodized in 0.2M sulfuric acid under 25V at 10°C, or 0.3 M oxalic acid under 40 V at 15°C for 4~6 hours. The alumina from first anodization was removed by etching in aqueous solution of 6wt% phosphoric acid (H_3PO_4) and 1.8wt% chromic oxide at 65 °C for 2 hours, followed by rinsing with copious distilled water and re-anodized for desired time (depending on requirement of pore length) with 5.0 μm/h alumina growth rates under the same conditions of the first- step anodization.

Thinning the Barrier Layer (for AC deposition): A third anodization was occasionally performed in 0.2 M phosphoric acid (H_3PO_4) at 10°C under 25V for AAO membrane anodized in sulfuric acid and 15°C under 40V for alumina template formed in oxalic acid in order to reduce the barrier layer thickness to facilitate subsequent electrodeposition and to reduce effects of the barrier layer on the subsequent AC deposition. For example, after this third anodization, the barrier layer thickness can be reduced from 40nm to 25nm in case of AAO template anodized in oxalic acid.

Widening Pores (for both AC and DC depositions): The pore diameter could be increased by partial dissolution of aluminum oxide in an acidic solution. Widening in a solution of 0.1M phosphoric acid (H_3PO_4) at 40°C for varying times can produce pores ranging from 40nm (anodized in oxalic acid) to 80nm in AAO films. This process can

also help improvement of smoothness of pores. For AC electrochemical deposition, this is the last step before the electrodeposition process. For DC deposition, more steps are needed as described below.

Removal of the Barrier Layer (for DC deposition only): This process is required for DC electrochemical deposition in order to form a working electrode on the AAO template surface. There are two typical methods for this purpose. One is the usage of saturated mercury chloride, and the other is a copper- based solution.

Saturated mercury chloride ($HgCl_2$) solution is applied to remove the un-anodized aluminum substrate for applications when both ends of the template channel need to be open. This method enables slow reaction of amalgam to avoid damage of AAO template, but it is not recommended based upon environmental considerations.

In other approach, the un-anodized aluminum is soaked in the solution of 0.2 M $CuCl_2$ in 36% HCl A brief sonification is needed to remove a residue of copper that may stick onto the alumina template. This reaction is exothermic, and its etching rate can be controlled by changing concentration of acid and copper ions. The reaction generated in this process needs to be controlled with cold water; otherwise, the pore structure of AAO could be damaged. Then aluminum oxide barrier layer at the bottom of pores is removed by chemical etching with 5wt% phosphoric acid at 30°C for 50 to 90 minutes depending on pore size (or barrier layer thickness).

Thermal Evaporation of Metal Electrode (for DC deposition only): The working electrode in DC electrodeposition was obtained by thermal evaporation of silver shot (1~3mm, 99.999% metal basis. Premion®). An evaporator equipped with a 3cm ion gun, 3 sputter guns, 4 thermal sources, thickness monitor, and cryo-pumped vacuum chamber was used as Center for Nanophysics and Advanced Materials (CNAM) shared facility. A 150 nm-thick Ag film was then deposited with a growth rate of ~0.15nm/s, which was fast enough to complete deposition in 30 minutes, but also slow enough to generate high-quality films. Templates with Ag working electrode film could be stored for over 6 months in a container (Fluoroware® Inc., single wafer shippers 2.5inch) to protect them from dust at room temperature (20~30°C).

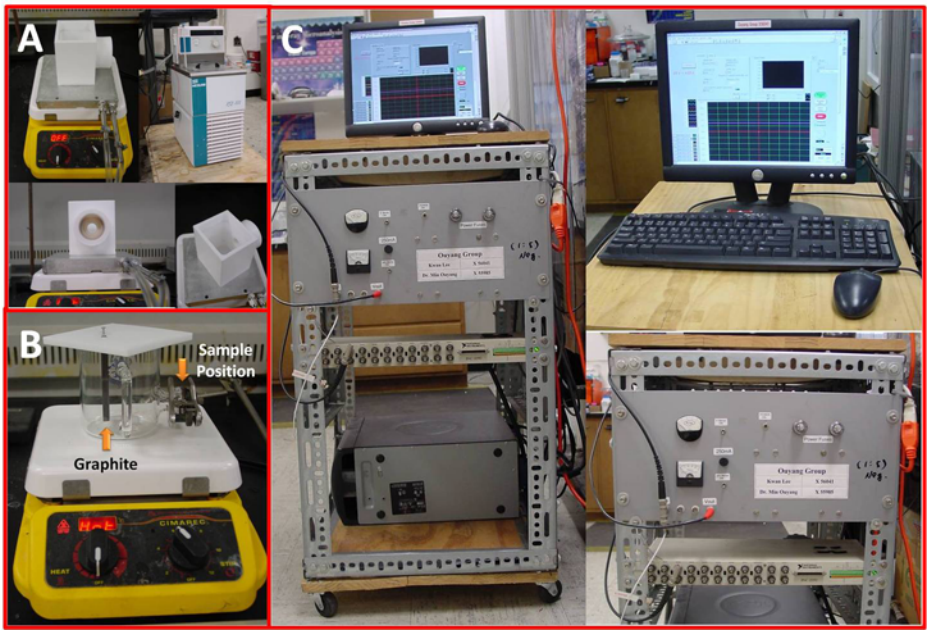

Figure 3.1 Home-made apparatus for electrochemical synthesis; (A) Teflon cell for anodization process on cooling metal plate and chiller; (B) Glass cell for DC and AC electrochemical deposition with graphite counter electrode attached on Teflon cap; and (C) Mobile home-made computer-controlled electrochemical work station with labview software.

3.3 Synthesis of Various Pure Nanowire Structures

3.3.1 Semiconductor nanowires

The optical properties of semiconducting nanowires have been extensively explored because of their tunable band gaps, ballistic transport, optical anisotropy, and strong excitonic effects [103]. As the diameter of a nanowire decreases to a size comparable to the exciton Bohr radius (for example, 2.8nm for CdS and 5.4nm for CdSe), their optical properties are significantly modified by radial quantum confinement [110, 111]. For example, a blue-shift in the photoluminescence (PL) was observed in CdSe nanowires possessing small diameter, which was attributed to quantum confinement effect in electronic band structures [112]. In addition to the quantum confinement effect, optical properties can also be influenced by such as composition and crystallinity of semiconductor nanostructures [113]. Any deviation from stoichiometry leads to imperfections within the nanowire crystal lattice and affects its properties. In this section, high quality semiconductor nanowires of CdS and CdSe are fabricated by versatile template based electrodeposition.

Experiment: Cadmium chalcogenide (CdE = CdS and CdSe) nanowires were synthesized with an AAO template (anodized in oxalic acid) by AC electrodeposition with an applied square waveform in non-aqueous electrolyte solution. The electrolyte solution consisted of 0.055M $CdCl_2$ and 0.19M S (or saturated Se) in organic solvents

such as dimethyl sulfoxide (DMSO) at high temperature [114]. All electrodepositions were performed at high temperature (100-120°C for CdS and 170-180°C for CdSe) under AC electrodeposition (50Hz, 80% offset) with a square waveform ($40V_{peak}$ for CdS and $20V_{peak}$ for CdSe). Such a waveform was generated and controlled by a home-made electrochemical power system with labview software in Figure 3.1.

Results and Discussion: The mechanism of formation of cadmium chalcogenide nanowires in AAO templates with cadmium ions and dissolved chalcogen elements in DMSO can be understood in the following reaction equations at the cathode [114]:

$$Cd^{2+} + 2e^{-} \rightarrow Cd \tag{3.1}$$

$$Cd + E \rightarrow CdE \tag{3.2}$$

Cadmium ions are attracted to nanopores of AAO template and reduced with the assistance of applied current or potential between cathode and anode, while elemental S (or Se) atom diffuses into the pores. CdS (or CdSe) is formed with the reaction of Cd atoms and nucleated at the pore bottoms.

In a template- assisted electrodeposition, the diffusion direction of ions is confined along one dimension. Smaller pore size of templates can lead to a decrease in the diffusion rate of ions. Therefore, this process is determined by the diffusion rate of ions because it is slower than conventional surface electrochemical reaction and nanowires growth is controlled by the so called diffusion- limited electrodeposition

process. Therefore, the steady diffusion process under DC electrodeposition condition is generally favored to produce high quality semiconductor nanowires.

Meanwhile, in the case of the AC process, the alternation of electric field for discharging keeps changing both the diffusion direction and the diffusion rate of the ions. It could easily cause a high density of defects with polycrystalline morphology in nanowires [114]. This is the major reason why most syntheses of 1D nanostructures with template- assisted electrodeposition so far have been performed using DC (either potentiostatic or galvanostatic) method for excellent crystallinity. To overcome the disadvantages of traditional AC electrodeposition, a symmetric square waveform consisting of 80% off-time (16ms) for cathodic deposition and 20% off-time (4ms) for anodic potential was applied in our synthesis. This deposition sequence with short anodic potential time could reduce the effect of continuous changing of diffusion direction and rate of ions under the AC deposition, and help to discharge the barrier layer under a steady state diffusion limited process at high temperature with controlling off-time. It has been demonstrated to develop single crystalline nanowires as shown below.

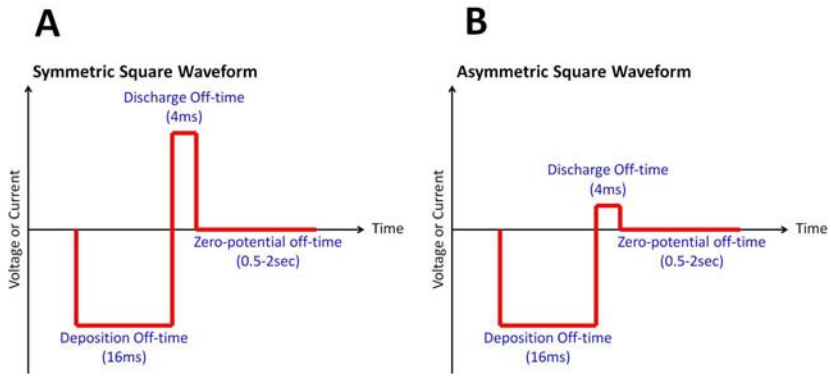

Figure 3.2 Controlled square waveform for AC electrodeposition: (A) symmetric and (B) asymmetric potential.

3.3.1.1 CdS Nanowires

Figure 3.3(A) shows a typical digital photo of as-deposited CdS nanowires embedded in AAO with the characteristic CdS color. The transmission electron microscopy (TEM) image shown in Figure 3.3(B) reveals that the length of CdS nanowires can be well controlled with electrodeposition time within less 10% deviation and the average diameters were around 40 nm, which corresponds to the pore size of the applied AAO templates. High resolution TEM (HRTEM) images and corresponding Fourier transform of this HRTEM image indicate that single crystalline CdS nanowires adopted the hexagonal Wurtzite structures, and that they were grown along the [002] direction (c axis) as shown in Figure 3.3(C) and Figure 3.3(D) for different lengths of CdS nanowires.

In Figure 3.3(E) compares two room-temperature absorption spectra of CdS nanowires with different lengths. Though the intensity is different, both show an absorption peak around 446nm with a blueshift of about 70 nm compared to exciton absorption of bulk CdS (515 nm). It clearly indicates the existence of quantum confinement effect, determined by diameter [115]. Moreover, the shoulder edge of absorption spectrum can be ascribed to the size uniformity of the as-grown nanowires. The size quantization is due to the localization of electrons and holes in a confined volume of the semiconductor nanowires. This results in a change in energy band structure including separation of individual energy levels and an increase in the effective optical bandgap of the semiconductor as compared with the bulk value.

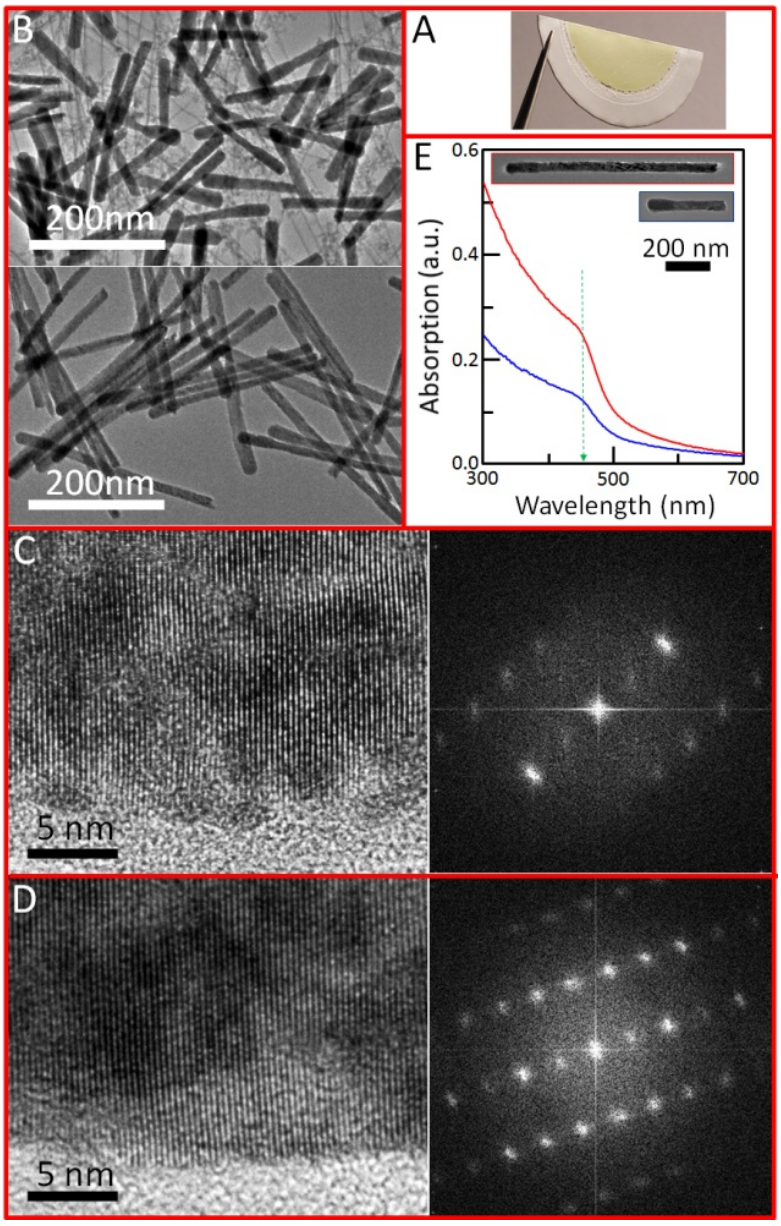

Figure 3.3 Semiconductor CdS nanowires: (A) photo of AAO template with AC deposited single crystalline CdS nanowires, (B) Large scale TEM images of CdS nanowires with two different lengths, (C) High- resolution of TEM image of one short CdS nanowires, showing single crystalline lattice (Left) and diffraction pattern (Right), (D) High- resolution of TEM image of one long CdS nanowires, showing single crystalline lattice (Left) and diffraction pattern (Right), (E) Length dependence of optical absorption of CdS.

3.3.1.2 CdSe Nanowires:

Selenium powder was dissolved in DMSO solvent at much higher temperature (i.e. around 170~180°C) than the dissolution temperature of sulfur in DMSO (110~120°C). Therefore, a high temperature process of CdSe electrochemical deposition is required to avoid re-precipitate the Se powder.

Similar to the CdS nanowires, single crystalline CdSe nanowires in AAO could also be achieved by our AC deposition, however, the specific synthetic conditions needed to be adjusted. For example, as compared with the condition of CdS nanowires (under 40V), CdSe nanowire deposition was performed under 20V with a symmetric square waveform (50Hz, 80% cathodic potential off-time). Application of a lower potential is caused by a positively shifted cathodic potential and the increase in the rate of diffusion, ionic mobility and electrolyte conductivity due to high temperature process.

In Figure 3.4(A), a typical photograph (inset) of the CdSe nanowires prepared by electrodeposition in AAO templates is shown with different color from the CdS sample with the same diameter due to the different exciton energy. The CdSe nanowires have uniform diameters of about 40 nm, which was determined by pore diameters. The nanowires are about 500 nm in length and are found across the whole sample with an area of 3.2 cm^2 (deposition area was determined by 211 Viton O-ring used in electrochemical cell). This result indicates that nanowires can be filled uniformly into the pores of the AAO template by our optimized AC electrodeposition. Our HRTEM and selected area electron diffraction characterization (Figure 3.4(B)) suggest that the as-grown single

crystalline CdSe nanowires have the Wurtzite structure with a smooth morphology and with no other structural defect along the axis of nanowires. To my knowledge, this is an unprecedented level of control of single crystalline structure of II-VI semiconductor nanowires by our controllable AC electrodeposition techniques.

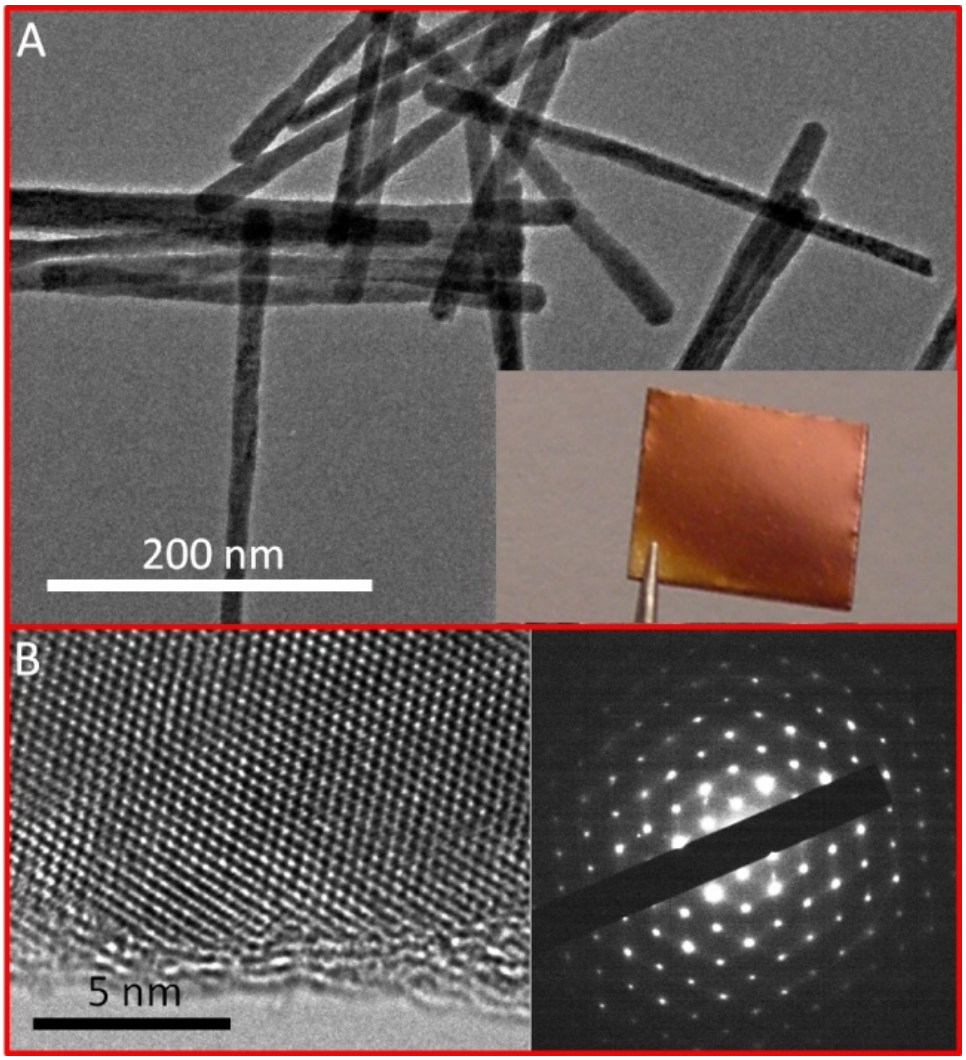

Figure 3.4 Semiconductor CdSe nanowires.(A) Large scale TEM images of CdSe nanowires. Inset, photo of AAO template with AC deposited single crystalline CdSe nanowires, (B) High- resolution of TEM image of CdSe nanowires, showing single crystalline lattice (Left) and diffraction pattern (Right).

3.3.2 Metal nanowires

Metal nanostructures in a certain size range alter only slightly their optical properties due to the long mean free path of electron in metallic materials, while a simple size change of semiconductor nanostructure controls the optical properties.

However, as discussed in Chapter 1, one important characteristic of metal nanostructures is the existence of a surface plasmon resonance (SPR) due to a collective free charge oscillation under the excitation by an electromagnetic wave (light). Such a SPR shows a strong frequency dependence on the anisotropy of metal nanostructures.

For instance, one- dimensional Au nanorods/nanowires can manifest different modes of SPR. One mode is perpendicular to the long axis of nanowires (transverse mode) and is typically resonant with light in the range of 500~550 nm, while the other is parallel to the long axis (longitudinal mode) whose plasmon wavelength depends strongly on the length of gold nanowires and shifted to the red with larger aspect ratios. Therefore in order to understand the SPR of metal nanowires, it is important to achieve a very tight control of their dimensionality.

To achieve this, a template- assisted electrodeposition method for metallic nanowires can show dramatic advantages regarding control of uniform length and diameter, as compared with other chemical synthetic routes in which undesired morphology of different metallic nanostructures are also generated simultaneously and make it difficult to investigate intrinsic physics of the SPR [116].

3.3.2.1 Ag nanowires

Experiment: For Ag nanowire synthesis, an AAO template was made under 25V with 0.2M sulfuric acid through the two- step anodization as mentioned in Section 3.2.1. An electrolyte was prepared by dissolving 0.05M silver nitrate in DMSO solvent at 80°C and electrochemical deposition was also performed at the same temperature. Under galvanostatic synthesis, pulsed AC deposition with a square waveform was applied with controlled zero- potential off-time to recover deficient silver ions after cathodic deposition in the pores. The optimized condition is 27.5mA cathodic potential (16ms) and 27.5mA anodic potential (4ms) with 2sec zero- potential off-time as one cycle of electrodeposition

Results and Discussion: Thus far, most silver nanowires electrodeposition with AAO templates has been performed using potentiostatic DC deposition techniques because the application of lower overpotential could lead to the formation of single crystalline structures formation based on a 2D layer growth mechanism [107]. Galvanostatic pulsed AC deposition has also been applied with a thinned barrier layer [78]. However, neither method has shown homogeneous length control of Ag nanowires inside the pores due to a few issues: (1) hydrogen generation; (2) poor adhesion of metal electrode on AAO template surface for DC deposition; or (3) instability of irregular thinned barrier layer of AAO template for AC deposition. To improve the uniformity of the electrochemically synthesized metal nanowires, a high- temperature processing, the

addition of additives in the electrolyte, and pre-treatment of AAO template for strong adhesion of metal electrode have been demonstrated [107, 117].

In our method for Ag nanowire formation and control in AAO template, organic solvent (i.e., DMSO) was used because the use of aqueous solutions produced a lack of length uniformity and control, due to hydrogen generation in the pores of template during cathodic deposition [118]. Furthermore, this organic solvent could also enable a high-temperature processing for Ag nanowires formation that could be helpful for ion diffusion and recovery of the concentration gradient caused by the deficient silver ions in the pores.

In Figure 3.5(A), the digital photo shows as-deposited Ag nanowires in an AAO template with the red-brown color associated with the SPR. The length distribution, crystallinity and surface configuration of Ag nanowires were further characterized in detail by TEM, as shown in Figure 3.5(B) and Figure 3.5(C). Low magnification TEM images indicate that most of the Ag nanowires were homogeneous in both length and diameter, but some deviation was noticed, and attributed to variation of the barrier layer thickness and/or instability during the electrodeposition. From the HRTEM image in Figure 3.5(C), planar defects were observed with different contrast across the wire due to lattice defects such as twin boundaries and stacking faults. Such structural defects can be understood that our pulsed AC deposition technique might differ from the steady state diffusion limited process in a DC deposition because of zero- potential off-time, which enable recovery of the concentration gradient in the pores with high temperature. Moreover, a relatively high overpotential was applied due to the rectifying barrier layer

and led to large grain formation in the pores and generation of planar defects in each cycle of cathodic deposition.

With the capability of homogeneous length and diameter control of Ag nanowires, anisotropic optical features with different aspect ratios were investigated, as shown in Figure 3.5(D). The optical spectra of Ag nanowires were characterized with a UV-vis-NIR spectrophotometer (Chapter 1), in which Ag nanowires were released from AAO templates and re-capped with alkanethiols in order to avoid sample aggregation and to achieve homogeneous dispersion in chloroform ($CHCl_3$) solvent. Clearly, different dipole modes of the Ag nanowires are shown in which a transverse mode near 400nm can be attributed to a homogeneous diameter of Ag nanowires, uniquely determined by the pore size, and a length dependent longitudinal dipole mode, as well as higher- order multiple mode are seen with red shifting as the length of Ag nanowires increases.

Most investigations of SPR with Ag nanowires with large aspect ratio have been done with single nanowires [16, 119] or demonstrated only two dipole modes in nanorods with small aspect ratio because it was hard to synthesize uniform silver nanowires through chemical synthesis. However, template- assisted techniques enable easy control of nanowire length with deposition time.

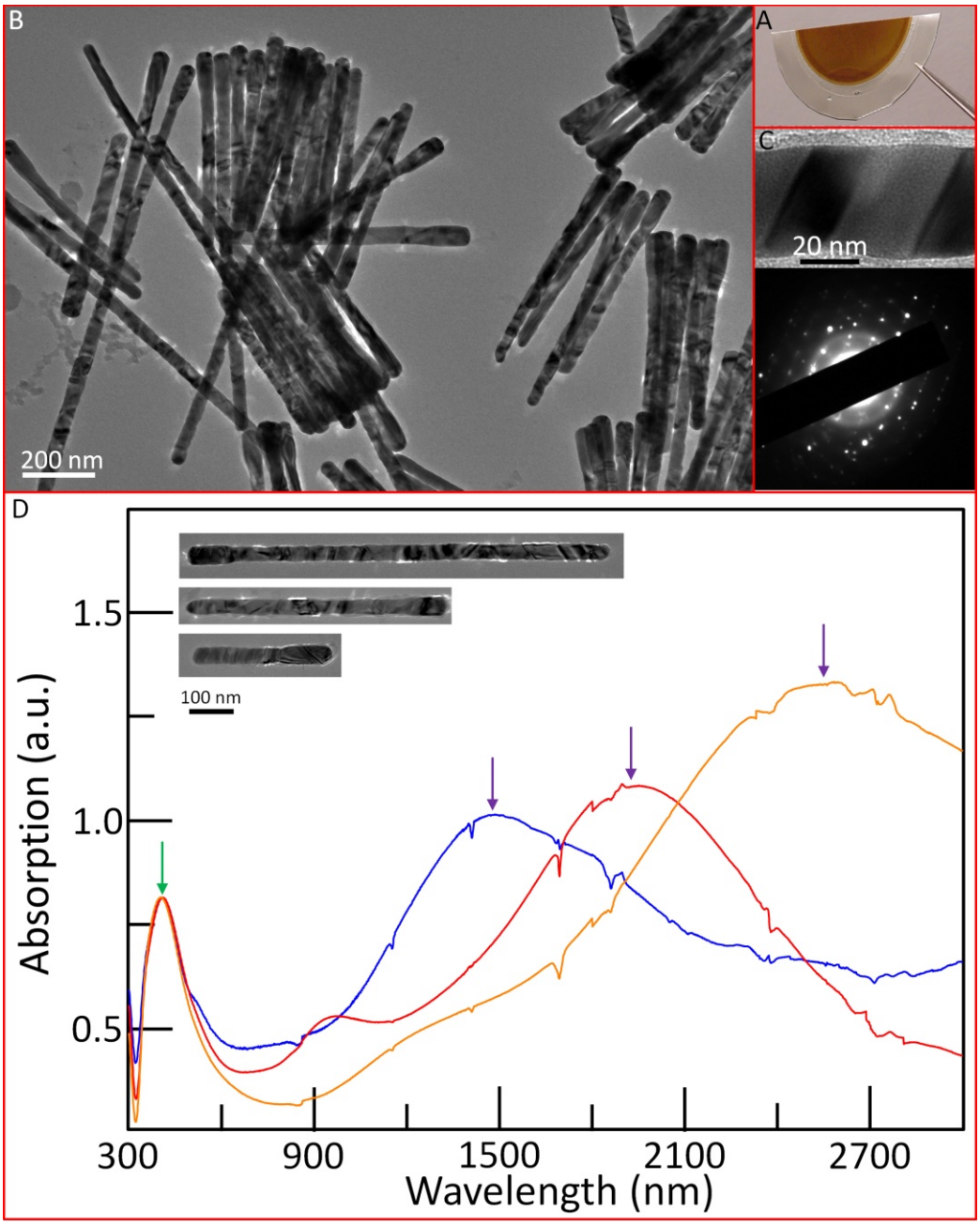

Figure 3.5 Metallic Ag nanowires.(A) Photo of AAO template with AC deposited Ag nanowires, (B) Large scale TEM images of Ag nanowires, (C) (Top) High resolution of TEM image of section of Ag nanowires, showing twin structure along wire; (Bottom): electron diffraction pattern;(D) Length dependence of longitude and transverse surface plasmon resonance modes of Ag nanowires. (Inset) typical TEM images of three nanowires with three different lengths. (Spectra normalized for transverse mode)

3.3.2.2 Au Nanowires

Experiment: For Au nanowires, the DC method was applied with a commercial gold electrolyte (Orotemp 24 RTU (Au, cat. no. 2/0927B)). AAO template preparation for DC process was described in Section 3.2.1. Silver was thermally evaporated onto template as working electrode (150nm thickness film). Silver nanowires as sacrificial segment were deposited first under galvanostatic DC deposition with commercial electrolyte (025 Ag RTU (Ag, cat. no.x7522000)) to fill the pores that were etched away with an Ag working electrode film in nitric acid after Au nanowire formation at room temperature. DC deposition was performed under 0.8mA/cm^2 (for sacrificial Ag nanowires) and 1.4mA/cm^2 (for Au nanowires), and length of Au nanowires was controlled deposition time at room temperature.

Results and Discussion: Free electrons of a noble metal (i.e., silver, gold, and copper) excited by visible light can fulfill the requirement of surface plasmon resonance (SPR) condition because they have a dielectric constant which is dependent on the incident frequency and consists of a large negative real component and a small imaginary component in the range of visible- light wavelength. For instance, spherical gold and silver particles with a diameter in the range of less 50nm shows SPR peaks at around 530nm and 450nm, respectively due to wavelength dependence of their dielectric constant.

While Au nanowires could also be synthesized by an AC electrodeposition method at high temperature similar to the Ag nanowires described in Section 3.3.2.1, a galvanostatic DC method was used for SPR investigation of Au nanowires because this method could offer a smooth morphology. We found that pre- deposition of sacrificial Ag nanowires was critical, and could lead to controlled uniform length of subsequent Au nanowires, because it could avoid the inhomogeneous adhesion issue of thermally evaporated Ag film.

Most of the Au nanowires manifested polycrystalline feature with very large domain size (50~100nm) and smooth morphology. Under the typical deposition conditions, the length deviation was in the range of less than 10%. Length was simply controlled by the time of galvanostatic DC deposition, as shown in Figure 3.6(A)-(D).

In Figure 3.6(E), the appearance of multiple absorption peaks in absorption spectra of Au nanowires can be attributed to multiple dipole SPR modes. While the transverse SPR mode shows a nearly constant energy (near 530nm) for Au nanowires with different length, longitude mode of SPR shows an obviously red-shifted energy with increasing length (152±6nm (AR=3.5), 230±10nm (AR=5.3), and 304±12nm (AR=7.1)). Furthermore, a higher order longitude mode of the SPR can also be observed, and shows a similar length dependence as well. Our observation here agreed qualitatively with a previous report [116], even though the SPR energies are red-shifted compared with literature values. This can be understood to be associated with a different dielectric environment due to the solvents (for example, refractive index of D_2O (n=1.32) in this other literature report and Chloroform (n=1.45) in our measurement) [120].

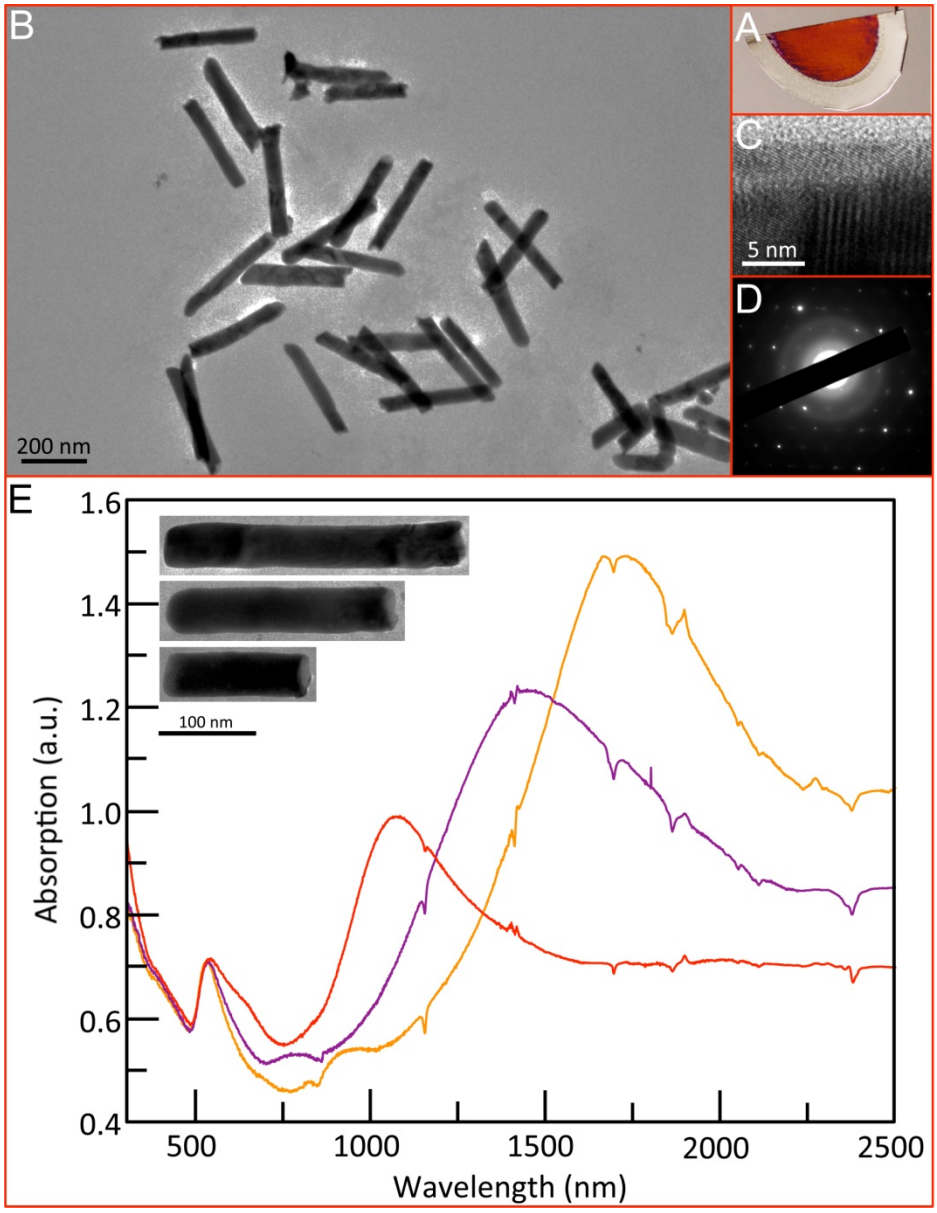

Figure 3.6 Metallic Au Nanowires. (A) Photo of AAO template with DC deposited Au nanowires; (B) Large scale TEM images of Au nanowires; (C) High resolution of TEM image of section of Au nanowires, showing polycrystalline structure along wire; (D): electron diffraction pattern; (E) Length dependence of longitude and transverse SPR modes of Au nanowires. (Inset) typical TEM images of three nanowires with three different lengths.

3.3.3 Magnetic Nanowires

3.3.3.1 Fe Nanowires

Experiment: An AAO template was prepared by the same method as described in Section 3.2.1 in this chapter. For Fe deposition, pore widening was employed after the second anodization in order to reduce the barrier layer thickness. This was done by immersing the samples in 0.1 M phosphoric acid at 37 °C for various lengths of time. Fe was deposited from an electrolyte consisting of $FeSO_4 \cdot 7H_2O$ 120 g/L; boric acid 45 g/L; ascorbic acid 1 g/L by using pulsed electrodeposition The pH value of electrolyte solution was adjusted to be 3. Electrodeposition was carried out at 18.2 Hz using a $40V_{peak}$ square waveform. The crystallinity of the Fe nanowires was determined by transmission electron microscopy (TEM). The magnetization measurement was carried out using a superconducting quantum interference device (SQUID) magnetometer.

Results and Discussions: Figure 3.7(A) shows as-deposited Fe nanowires in an AAO template, with a homogeneous black color. TEM images (Figure 3.7(B) and (C)) indicate that Fe nanowires have a uniform diameter of 60nm, and selected area electron diffraction (SAED) patterns of Fe nanowires deposited in templates indicate single crystals.

Anisotropic magnetization in such 1D magnetic nanowires is revealed by hysteresis loop measurements at 300K, as shown in Figure 3.7(D). Results obtained with

the magnetic field oriented both perpendicular to the template surface (i.e., longitudinally along the nanowire axis) and parallel to the template surface (i.e., transverse to the nanowire axis) are represented by the red solid curve and the blue solid curve, respectively. In addition, the response of a pure AAO template supported with Teflon tape in the SQUID is shown (black solid curve) with pore axial orientation parallel to applied magnetic field. The coercivity (H_C) in the longitudinal direction is measured to be ~1100 Oe, and the squareness $M_{Remanence}/M_{Saturation}$ = 0.60. In contrast, the hysteresis loops measured transverse to the nanowires are very narrow, as for most superparamagnetic materials.

The competition between magneto-crystalline anisotropy and shape anisotropy of the magnetic nanowire array generally results in an effective anisotropy of magnetic materials [121]. In the case of a polycrystalline nanowire, anisotropic magnetic properties derive from the shape anisotropy, because the magneto-crystalline anisotropy would be rather small in nanowires with large aspect ratio [121, 122]. In contrast, as the diameter increases, the shape anisotropy decreases and the moments will no longer be fully coaxial with the nanowire's long axis. Our results for the magnetization show a larger value than those of previous reports with a similar shape. This can be attributed to the crystallinity of our as-grown Fe nanowires in AAO (single crystal or highly textured states have higher coercivity and remanence than that of polycrystalline nanowires [123]).

A temperature- dependent magnetization measurement was also performed with the zero-field-cooled (ZFC) and field-cooled (FC) magnetization curves of Fe nanowire arrays in Figure 3.7(D) (bottom). The samples were cooled from 300 to75K without applying an external field and then a field of 1000 Oe was applied and the magnetic

moments were recorded as the temperature increased after reaching 75K. For FC measurements, the samples were cooled from 300K under an applied field of 1000 Oe; then the magnetic moments were recorded as the temperature increased. The data shown in red are for Fe NWs embedded in AAO template with nanowire axial orientation parallel to applied magnetic field under ZFC (circle) and FC (square) measurements; those in blue are for Fe NWs embedded in AAO template with nanowire axial orientation perpendicular to applied magnetic field; the data shown in black are for pure AAO template (stabilized with Teflon tape) with pore axial orientation parallel to applied magnetic field.

A change of slope with temperatures was detected in the low temperature range for both the ZFC and the FC processes. Specifically, in the ZFC process, the magnetization rises at a different rate in the parallel aligned Fe nanowires compared with perpendicular alignment of sample to applied magnetic field. This also highlights the anisotropic properties of Fe nanowires in AAO template.

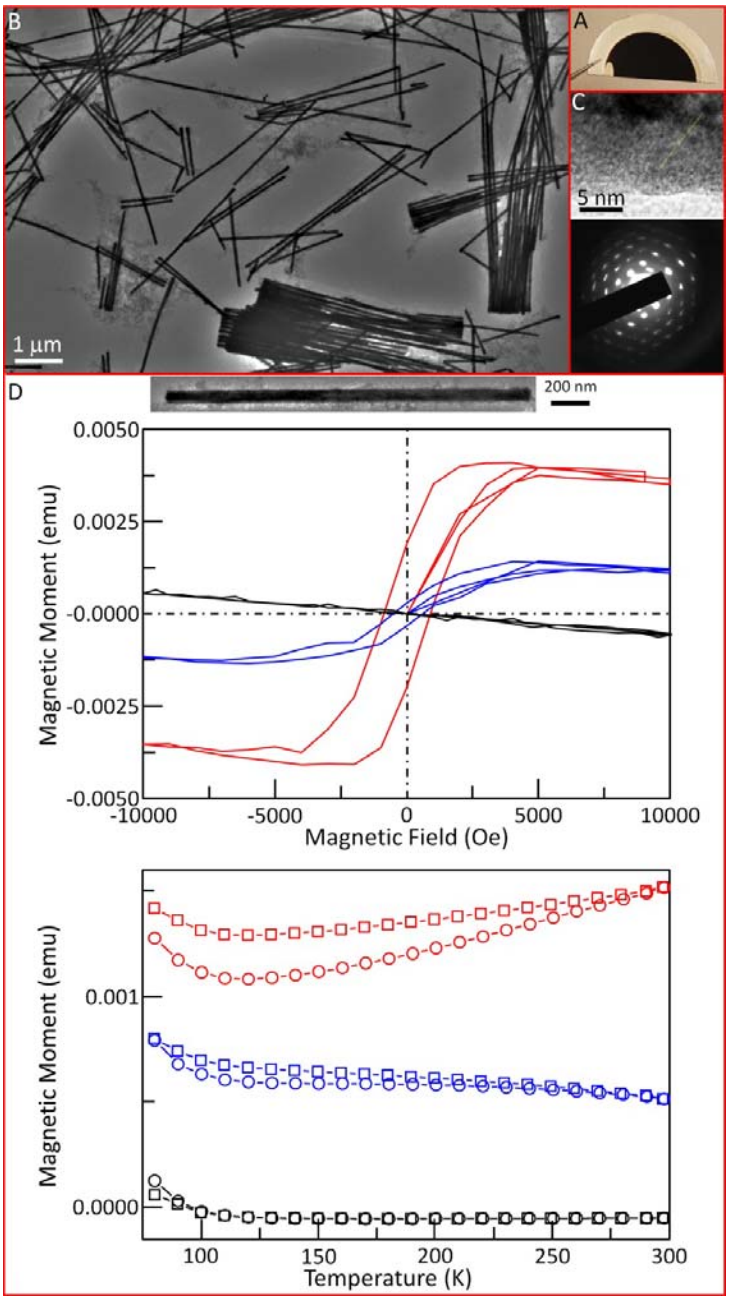

Figure 3.7 Magnetic Fe nanowires: (A) Photo of AAO template with AC deposited Fe nanowires, (B) Large scale TEM images of single crystalline Fe nanowires, (C) (Top) High resolution of TEM image of section of Fe nanowires, showing single crystalline features; (Bottom): electron diffraction pattern; (D) SQUID measurement of Fe nanowires in AAO (nanowires axial orientation parallel (red), perpendicular (blue) to applied magnetic field; black with pure AAO template) under ZFC (○) and FC (□) .

3.3.3.2 Ni Nanowires

Experiment: Electrodeposition was carried out under inert atmosphere protection in which the electrolyte, AAO template, cathode, and graphite anode were housed in a sealed glass cell with condenser and nitrogen gas flow. Nickel chloride was dissolved in either DMF (dimethylformamide) or DMSO with a 0.05M concentration. The electrolyte temperature was controlled in a silicone oil bath at 170°C and protected with high purity nitrogen gas. An AC technique (60V peak-to-peak voltage in sine waveform, 50Hz) was applied.

Results and Discussion: Figure 3.8(A) shown with digital photo of as-made Ni nanowires embedded in AAO by using DMF as solvent. This results in a black-brown color depending on the length of Ni nanowires. The crystallinity of Ni nanowires was characterized by TEM with diffraction pattern, as shown in Figure 3.8(B) and Figure 3.8(C) respectively. The results indicate that these uniform Ni nanowires possess polycrystalline structure. A tube morphology in the TEM images was attributed to the residue of incompletely dissolved aluminum oxide template by sodium hydroxide (NaOH). It was suggested before that oxide layer of the AAO template had a different anion impurity concentration associated with anodizing electrolyte, resulting in a different etching rate in an etchant solution like NaOH and the formation of thin alumina nanowires or nanotubes [124].

Very interestingly, I observed the formation of axial heterostructures if the solvent was changed from DMF to DMSO. Such axial heterostructures was attributed to the junction between the crystalline Ni nanowires by electrodeposition and the amorphous Ni-DMSO compound nanowires by electroless- deposition. This axial structure was formed when the sample was placed within pure DMSO solution without gas protection after nickel nanowire deposition. Control of the DMSO soaking time can result in a different length of the nickel-DMSO part as shown in Figure 3.8(D).

While the pure nickel segments in Figure 3.8(D) manifest polycrystalline structure feature, Ni-DMSO segments are found to be amorphous. It is not clear at this stage how the amorphous Ni-DMSO was formed during DMSO soaking. Qualitatively, formation of such an axial heterostructure could be understood as follows: Nickel ions were able to form a coordination compound with DMSO easily at room temperature [125, 126], but this compound was not stable at high temperature, and the content of pure nickel ions in the DMSO solvent increased. These ions can be deposited as pure Ni nanowires by a high temperature electrodeposition process [127]. Pre- heated pure DMSO was used to rinse the sample without heating the source after electrodeposition. During the cleaning process under cooling, some content of nickel ions trapped in the pores can form a coordination compound with DMSO and be absorbed easily on inner pore wall of AAO template [127]. Furthermore, length control via DMSO soaking time is related to the formation rate of nickel-DMSO coordination compound with cooling rate. It has been reported that amorphous magnetic-DMSO composites present magnetic response with anisotropic features in one dimensional nanostructures to an applied magnetic field [127]. Therefore, the combination of electro- and electroless- deposition

process for Ni/Ni-DMSO junction might offer a new method for versatile magnetic axial structures

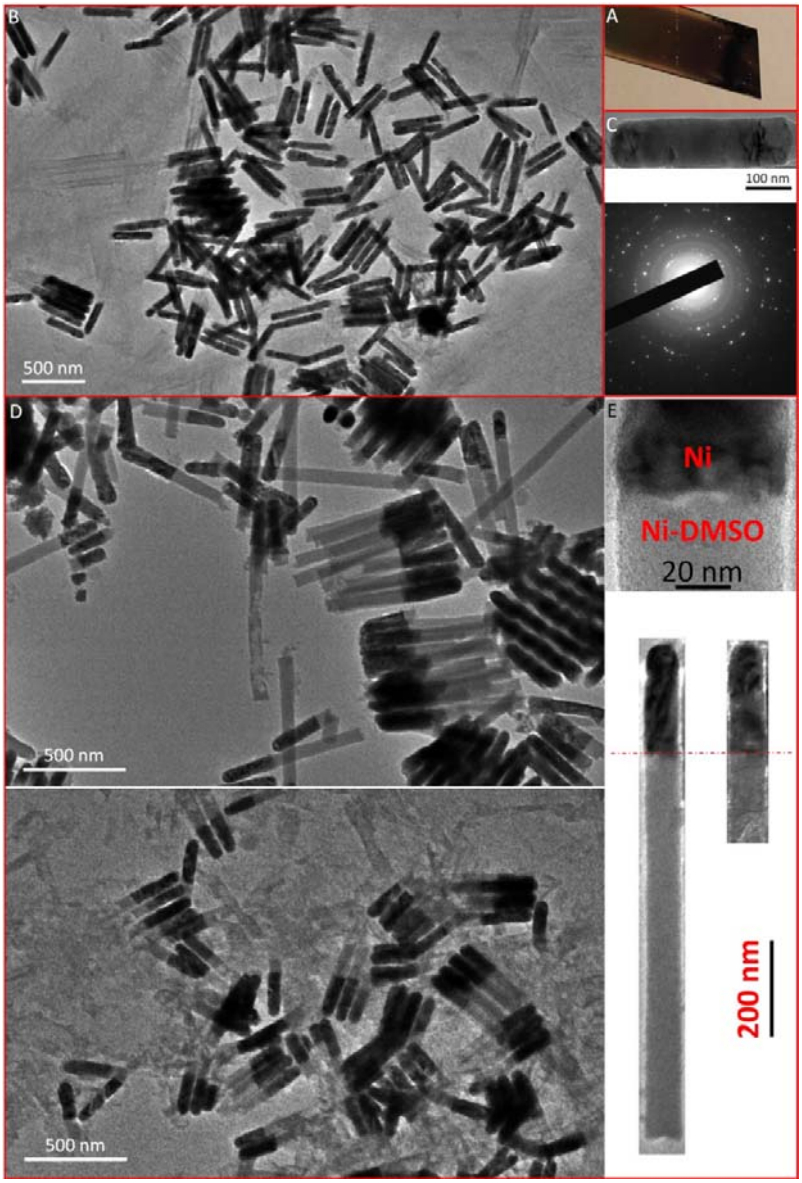

Figure 3.8 Magnetic Ni and Ni-DMSO nanowires. (A) Photo of AAO template with AC deposited Ni nanowires; (B) Large scale TEM images of Ni nanowires; (C) (Top) one typical TEM image of Ni nanowires; (Bottom): electron diffraction pattern; (D) Ni-Ni-DMSO nanowires with two different length of Ni-DMSO nanowires; (E) (Top) high resolution of interface of Ni nanowires and Ni-DMSO nanowire; (Bottom) typical TEM images of two nanowires with same Ni section but different lengths of Ni-DMSO section

3.4 Synthesis of Various One- Dimensional Axial and Radial Hetero- Structures

Unique radial confinement in one- dimensional semiconductor nanostructures can be expanded to axial and radial heterostructures with composition modulation for additional control of confinement, incorporating quantum wells (QWs) into nanowires in axial and/or in radial direction.

In radial nanowire heterostructures, new interfacial properties can be enabled for unique electronic photonic, and plasmonic application. For example, accumulation of high mobility hole carriers was demonstrated in Ge@Si core-shell nanowires, due to the modified electronic energy band structure at the interface of the radial nanostructure [128]. This has enabled the fundamental investigation of quantum transport, and the realization of the highest performance p-channel NWFETs.

With an AAO template, 1D axial heterostructures can be achieved by a sequential electrodeposition process by simply changing electrolytes involving desired target materials. On the other hand, for radial heterostructures, nanowires produced with an AAO template can be employed as another template (i.e., core) for shell formation due to homogeneity of nanowires demonstrated above. To that end, I have developed a modified AC technique for axial heterostructures with an AAO template as well as a versatile chemical synthesis for radial heterostructures, by using AAO-made nanowires as core nanowires.

3.4.1 Axial Heterostructures of Semiconductor Nanowires

3.4.1.1 CdS-CdSe Axial Heterostructures

Experiment: As an axial hetero-semiconductor nanowire structure, CdS nanowires were deposited first as described in Section 3.3.1, and then CdSe nanowires were deposited subsequently. For the CdS layer, a symmetric AC deposition technique (50Hz, $40V_{cathodic}$, 80% off-time) was applied at 110~120°C with controlled cathodic potential off-time percentage.

After deposition of the CdS layer, a pre-heated pure DMSO solvent was used to rinse to remove excess S residue, and the cell was heated to 170~180°C for CdSe nanowires deposition. For the CdSe nanowire deposition, an asymmetric AC deposition ($20V_{cathodic}/5V_{anodic}$, 80% off-time) was used, using the same frequency, and off-time of the cathodic potential.

Results and Discussion: For a second or subsequent layer of electrodeposition, an asymmetric AC technique was used with a square waveform. It was observed that the application of a large discharge voltage (or anodic potential) in a symmetric AC method for 2^{nd} layer could often cause formation of CdSSe alloy during CdSe nanowire deposition, with an absence of a sharp interface between CdS and CdSe segments.

An optimized asymmetric AC deposition method has been developed and extended to multiple layer deposition in sequences of CdS/CdSe.

The axial heterostructures were characterized by TEM. Figure 3.9(A) and Figure 3.9(B) are low- and high- resolution TEM images as well as Fourier transforms of the HRTEM images. They clearly depict a representative CdS/CdSe axial junction. A wurtzite (hexagonal) crystal structure for both CdSe and CdS segments with growth directions along [002] direction can be unambiguously identified. Importantly, the junctions between CdSe and CdS sections exhibit a sharp epitaxial interface (due to less than 5% stacking faults between wurtzite CdS and CdSe) and the alloy-free localization of Se and S within each section is confirmed by EDS mapping analysis in Figure 3.9(B).

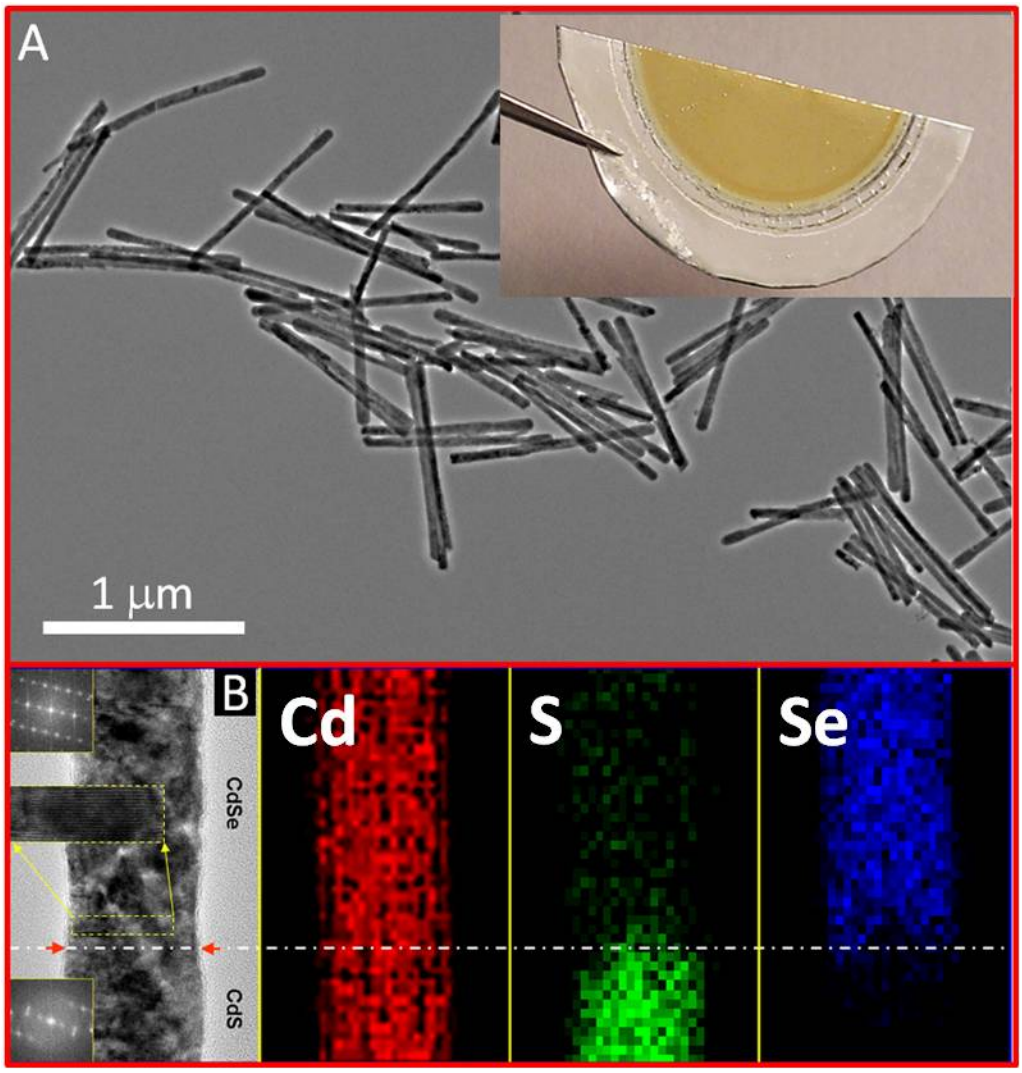

Figure 3.9 CdS-CdSe axial heterostructure; (A) Large scale TEM images of CdS-CdSe nanowires. (Inset) Photo of AAO template; (B) In-depth characterization of CdS-CdSe hetero-interface by high resolution imaging and EDS mapping.

3.4.1.2 CdS-CdSe-CdS Axial Heterostructures

Experiment: Our technique for simple axial CdS-CdSe junction fabrication can be further extended for more complex axial heterostructures, including CdS-CdSe-CdS axial heterostructures by continuous layer deposition. All deposition processes resulted in epitaxial growth, the deposition rates were controlled by the cathodic potential, and the length was controlled by the time. Each layer deposition was followed by a cleaning process with pure DMSO solvent, at high temperature, to remove the residues of previously deposited materials.

Results and Discussion: In Figure 3.10(A), a large scale TEM image of few micron long CdS-CdSe-CdS heterostructure nanowires, with nanoscale portion of CdSe located in the middle is shown (digital photo of samples embedded in AAO is available in the inset to compare color change with Figure 3.9(A)). While the topographic TEM image cannot identify unambiguously such heterostructures, due to lattice similarity between CdS and CdSe, the existence and the length of CdSe can be determined from an EDS measurement, as indicated in the Figure 3.10(B). It was observed that the cathodic potential for the second layer (CdSe) and third layer (CdS) was not as critical as that of the first layer. It was interpreted that higher layer depositions results in epitaxial growth under the well controlled diffusion rate of cadmium cation after formation of first layer of CdS.

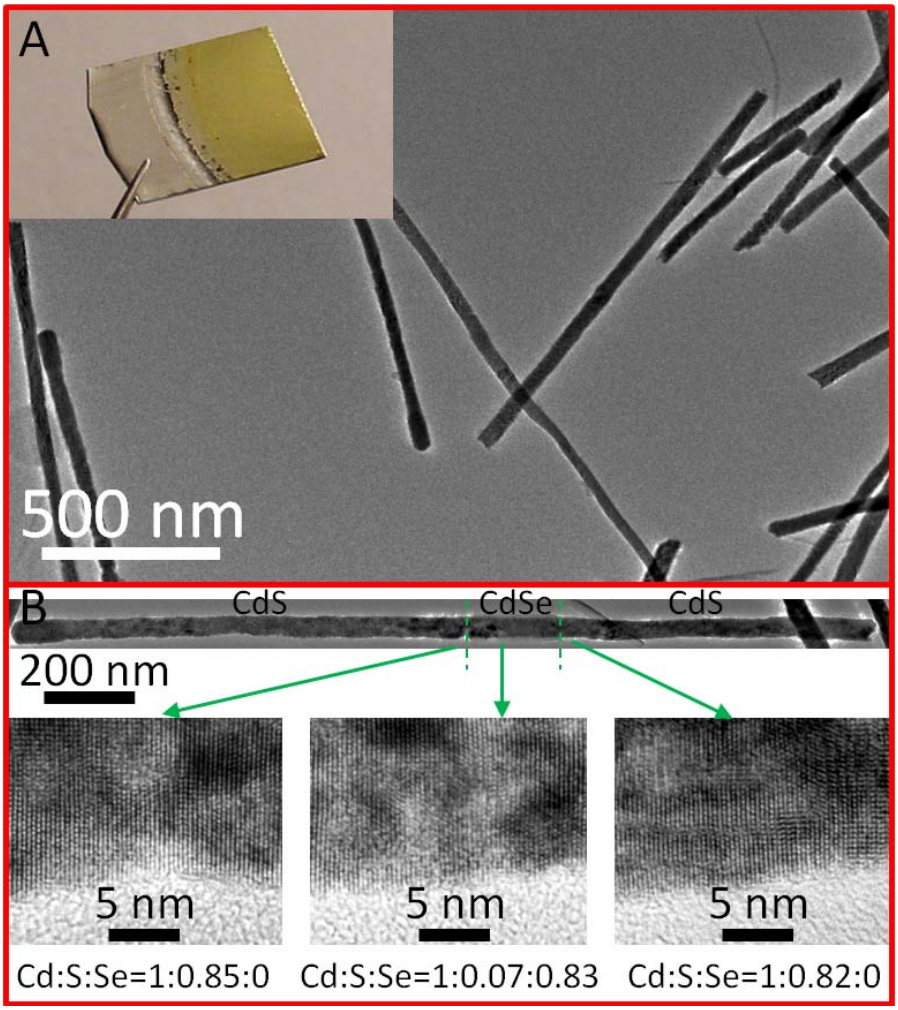

Figure 3.10 CdS-CdSe-CdS axial heterostructure; (A) Large scale TEM images of CdS-CdSe nanowires. (Inset) Photo of AAO template; (B) In-depth characterization of one typical CdS-CdSe-CdSe hetero-interface by high resolution imaging and EDS measurement.

3.4.2 Au@Ag Core-Shell Nanowires

Anisotropic metal nanostructures (nanorods) were generally synthesized using a cationic surfactant, CTAB (cetyltrimethylammonium bromide) using soft template methods because CTAB form rodlike micelles in aqueous solution [129]. Shape regulation using a surfactant-based method has usually been applied to synthesis of Au and Ag anisotropic nanostructures, enabling better optical properties. Au and Ag nanowires show different SPR modes at different frequency because of their different dielectric characteristics with incident light. Moreover, the combination nanostructures of these two constituents (for example, AuAg alloy nanostructures and Au@Ag nanorods) have also attracted interest due to the possibility of tailoring their optical and plasmonic characteristics. In particular Au@Ag core@shell nanostructures produced by surfactant-based methods exhibit unprecedented characteristic optical properties which are absent for individual constituent metals due to plasmon damping by interfaces in core@shell structures [16, 130].

Experiment: Au nanowires were synthesized using with the same method as in Section 3.3.2.2. After deposition, the AAO template was removed to release the Au nanowires, followed by a cleaning process to remove the residue. This consisted of NaOH with copious distilled water and re-dispersion in 0.2M CTAB solution. To form CTAB capping on Au nanowires, Au nanowires in CTAB solution were heated at 60°C

overnight with vigorous stirring to avoid aggregation and sedimentation of the Au nanowires.

After the Au nanowires were re-capped with CTAB surfactant, Au nanowires were centrifuged out (6800rpm, 10 minutes) and re-dispersed in 0.1M CTAB at room temperature with sonification. This was a stock solution of Au nanowires. For a typical Ag shell coating, 0.1M ascorbic acid (0.5mL), 0.01M silver nitrate (0.01mL) and 0.1M sodium hydroxide (0.75mL) were added to 1.5mL of stock solution of Au nanowires sequentially. The order of addition (L-ascorbic acid(aq) → AgNO3(aq) → NaOH(aq)) was found to be important in order to reduce self nucleation of Ag nanoparticles.

Results and Discussion: While chemical synthetic methods can provide metal nanostructures of controlled size, shape, and length, tight control of these materials parameters has been found to be very challenging [131]. This limitation can be overcome by template- based electrodeposition of metal nanostructure with tunable pore size.

Enabled by uniform Au nanowires produced by the template method, Au@Ag core-shell nanostructures can be obtained, as shown in Figure 3.11. In particular, Au nanowires were synthesized by electrochemical method without any protection by surfactants, which could lead to inhomogeneous Ag shell morphology. Therefore, it is crucial to deposit a CTAB cap on the Au nanowires surface by soaking freshly released AAO-made Au nanowires in 0.2M CTAB solution for a long time (12~18 hours) with vigorous stirring. After this CTAB capping process, Ag shell coating was controlled by adjusting the concentration of silver ions. As shown in Figure 3.11(A), a homogeneous

Ag shell morphology has been developed with an absence of by-product Ag nanoparticles and with a sharp interface (Figure 3.11(B)) between the AAO-made core Au nanowires and the chemically deposited Ag. In addition, the diameter of the Au in the Au@Ag nanowires is consistent well with the original pure Au nanowires, which further supports our conclusion that no alloy formation occurs in Au@Ag. The SAED pattern in Figure 3.11(C) represents the epitaxial growth of Ag shell on Au nanowires.

The ability to tune SPR modes of Au@Ag nanowires through the overgrowth of Ag shell onto Au core surface is clearly demonstrated in Figure 3.11(A) by comparing optical absorption spectra before and after Ag shell growth. By systematically investigating Au@Ag nanowires with similar Au core diameter and Ag shell thickness but different length, I observed that while the spectral position of transverse mode shows weak red shift by Ag shell formation, the longitude modes (both fundamental and higher modes) manifest very strong length dependences. In particular, long nanowires lead to large energy shifts of the longitude modes. This is understood by the difference of dielectric constant of Ag and Au, moreover, this result agrees well with Gans theory's prediction [27, 28] in which a strong red shift of the longitudinal SPR modes, but weak blue shift of the transverse SPR modes for prolate spheroids (rods) are predicted as aspect ratio increases.

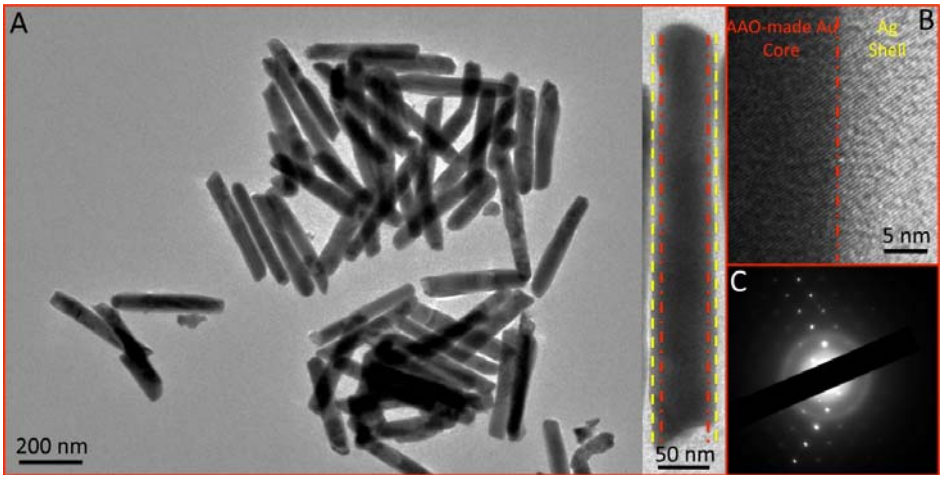

Figure 3.11 Au-Ag core-shell nanostructures; (A) Large scale TEM images of Au-Ag core-shell nanowires. (Inset) Photo of AAO template; (B) optical absorption of length dependence; (C)optical absorption of shell thickness dependence; Synthesis of Au-Ag coaxial nanowires with AAO-made Au core. (A) Large scale TEM image. Inset, TEM image of an individual coaxial nanowires. Dashed yellow and dashed red lines represent outer Ag shell surface and Au-Ag interface, respectively. (B)High- resolution TEM image, highlighting Au-Ag interface. (C) selected area electron diffraction of a Au-Ag coaxial nanowires.

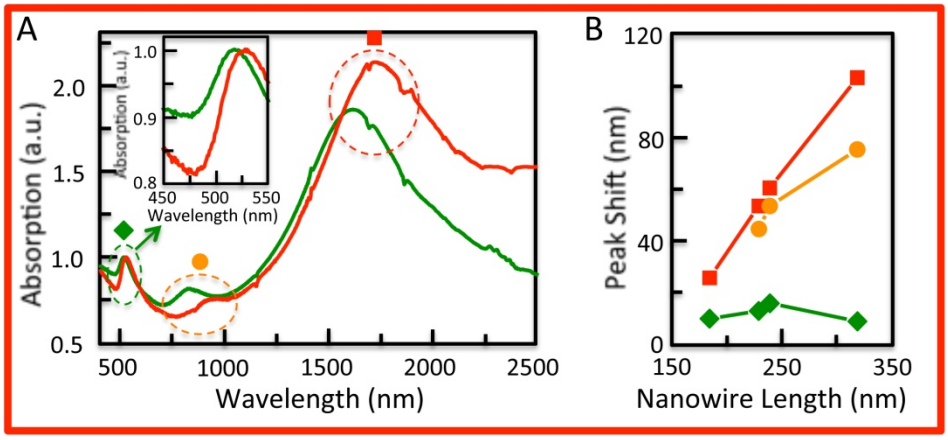

Figure 3.12 Tuning SPR modes of coaxial Au@Ag nanowires with Ag growth. (A) Absorption spectra of pure Au (red) and Au@Ag nanowires (green). Dashed oval circles highlight different spectroscopy shifting of different SPR modes before and after Ag growth. Inset, absorption spectra of transverse SPR mode.(B) Dependence of SPR peak energy shift on nanowire length induced by Ag shell growth. Red square (■), orange sphere (●) and green diamond (♦) were data of fundamental longitudinal SPR peak, quadruple longitudinal SPR peak and fundamental transverse SPR peak, respectively

3.5 Summary

In this chapter, I have summarized new syntheses and some preliminary characterizations of various uniform and well- controlled one- dimensional functional nanostructures. These were fabricated by AAO template- assisted electrochemical deposition including pure metallic, magnetic and semiconducting nanowires and corresponding axial and radial heterostructures. Some of these functional nanostructures will be otherwise difficult to fabricate by other approaches.

Availability of these high quality nanowires should offer opportunity to investigate fundamental plasmoncis, excitonic and magnetic physics at the nanoscale.

Chapter 4: Morphology Control and Mechanically Driven Nanoscale Crystalline Growth of Monocrystalline Semiconductor Based Hybrid Core- Shell Nanostructures

In this chapter, I will describe a novel universal non-epitaxial synthetic route to simultaneously achieve control of two independent fundamental materials characteristics, shape and monocrystallinity, of lattice-mismatched hybrid core-shell nanostructures. It possesses adaptable conformal and non-conformal core-shell configurations and dimensionality tailoring. The essence of our approach is to start with epitaxially grown bi-metallic core-shell with desired core and shell geometry and then to non-epitaxially convert anisotropic metal shell to monocrystalline semiconductor with morphology preservation via judicious kinetic control of both chemical transformation and crystalline grain growth processes. Additionally and importantly, meticulous non-epitaxial shape and monocrystalline evolution kinetics have revealed a new mechanical stress driven crystalline growth mechanism unique in bottom-up synthesis. This study represents an important step for high level control of artificial nanostructures with new functionality and property through shape regulation, and also substantially advances our understanding of nanoscale grain growth process.

4.1 Introduction

Anisotropic shape control of a nanostructure remains a long-standing fundamental problem in materials science, chemistry and physics, but is essential for tailoring its physical and chemical properties. Current available strategies for achieving shape control of homogeneous or heterogeneous pure metal and pure semiconductor nanostructures are essentially based on epitaxial growth in the context of classical Gibbs crystallization theories [132]. These are however inapplicable for hybrid metal- semiconductor nanostructures typically possessing substantial differences in lattice symmetry, lattice constants and chemical nature [133-141]. Indeed, even though hybrid metal-semiconductor core-shell nanostructures are emerging as key materials for applications in electronics, photonics, catalysis and spintronics, with capability to integrate multi-component and multi-functionality in a single unit, previous studies were mainly limited to thermodynamically stable spherical morphology [142-145]. I will demonstrate in this chapter that a novel and versatile non-epitaxial scheme to achieve unprecedented anisotropic control of hybrid core-shell structures, whereby the semiconductor shell manifests perfect monocrystallinity with well-defined anisotropic morphology that are independent of those of the dissimilar metal core. Additionally and importantly, this approach allows shape-directing monocrystalline growth spanning length scales from the nano- to the micron- scale under synthetic conditions outside of those for conventional two- dimensional grain growth. These results provide invaluable insights of new fundamental crystalline growth mechanisms.

4.2 Materials and Experimental Methods

All chemicals applied in this study were purchased from Sigma-Aldrich, Alfa-Aesa, and TCI, and were used as-received without further processing. The preparation of S-precursors followed previously reported recipes [145]. Deionized water (H_2O) was obtained by using a Barnstead NANOPure water purification system, having a resistivity of 18.2 MΩ-cm. All aqueous solutions were prepared in deionized water.

As-synthesized nanostructures in this chapter were characterized mainly by TEM and EDS. Samples for TEM characterization were prepared by adding one drop of sample solution onto 300 mesh Copper grids with carbon support films (Ted Pella #01820). Both JEOL 2100F and JEM 2100 LaB6 TEMs were used to determined size, morphology and elemental composition. Single- point EDS measurements were performed in STEM mode with JEOL 2100F.

Detailed synthetic procedures for the hetero- core-shell nanostructures presented in this chapter are summarized below.

4.2.1 Synthesis of conformal Au-CdS nanocubes

The synthesis of Au nanocubes was based on a modified process from a seed-mediated growth method [146]. In a typical synthesis, 0.125ml of 0.01M $HAuCl_4$ and 3.75ml of 0.1M CTAB (cetyltrimethyl ammonium bromide, $((C_{16}H_{33})N(CH_3)_3Br)$ were

mixed first. 0.6ml of ice- cooled 0.01M $NaBH_4$ aqueous solution was quickly injected into the mixture of $HAuCl_4$ and CTAB with vigorous stirring for 2 minutes, and the whole solution was then aged for 1 hour at room temperature to provide a seed solution. In order to grow Au nanocubes, the above Au seed solution was diluted by a factor of ten first, and then 20μl of diluted seed solution was added to a mixture of 6.4ml of 0.1M CTAB, 0.8ml of 0.01M $HAuCl_4$, 32ml of deionized H_2O and 3.8ml of 0.1M ascorbic acid (AA) with gently shaking. The reaction liquor was then aged for 13 hours.

In order to synthesize conformal Au-Ag nanocubes, Au nanocubes were collected by centrifugation at 5000rpm for 12 minutes, re-dispersed to 1ml of deionized H_2O and then loaded into a 40ml autoclave cell. 8μl of 4mM $AgNO_3$, 1.25ml of 0.15M BDAC (dibutoxydiacetoxysilane), 10.5ml of 0.1M CTAB and 0.5ml of 0.1M AA were added to the autoclave cell and then stirred for 5 minutes. After that, the autoclave cell was sealed and aged at 80ºC for 24 hours. As-made Au-Ag nanocubes were stabilized with CTAB surfactants and could be collected by centrifugation at 6000rpm for 15 minutes. The thickness of Ag shell could be increased monotonically by repeating the above Ag growth procedure.

In order to preserve the morphology during chemical transformation, Au-Ag nanocubes (that were originally passivated with CTAB surfactants) were recapped with alkanethiols molecules (such as $C_{10}H_{22}S$) by dispersing 5ml of Au-Ag nanocubes solution to 0.4ml of 10% $C_{10}H_{22}S$ in acetone. After that, 2ml of a S-precursor was prepared following the procedure described in previous publication [145]. This was then added to the $C_{10}H_{22}S$ recapped Au-Ag solution in acetone and reacted at 60ºC for 1 hour with vigorous stirring to convert Ag shell to amorphous Ag_2S shell. Au-Ag_2S nanocubes could

then be extracted by adding 10ml of toluene. To initiate cation exchange process between Ag and Cd ions as well as non-epitaxial crystalline growth of CdS shell, 0.06g of $Cd(NO_3)_2$ dissolved in 2ml methanol was added to 8ml of Au- Ag_2S nanocubes in toluene, followed by adding 10 drops of fresh TBP. It was reacted at 60ºC for 2 hours. This process could be stopped by adding excess ethanol. As-synthesized Au-CdS nanocubes were typically washed by the mixture solution of toluene and ethanol (1:5 volume ratios) for three or four times to remove excess chemicals such as $C_{10}H_{22}S$, OAm (oleylamine) and OA (oleic acid).

4.2.2 Synthesis of conformal Au-CdS nanorods

Synthesis of Au nanorods was achieved by modifying the previously described seed- mediated growth method with binary surfactant mixture of BDAC and CTAB [147]. The Au seed was obtained by adding 0.6ml of ice- cooled 0.01M $NaBH_4$ into a mixture solution of 5ml of 0.2M CTAB and 5ml of 5mM $HAuCl_4$ with vigorous stirring for 2 minutes at 25ºC. The surfactant mixture was prepared by adding 5ml of 0.15M BDAC to 0.1g of CTAB, followed by the addition of 0.1ml of 4mM $AgNO_3$. 5ml of 1mM $HAuCl_4$ was then added to the surfactant mixture solution with gentle stirring, followed by the addition of 0.06ml of 0.1M AA. After that, two droplets of Au seed solution were added, and the whole solution was aged for 16 hours. As-prepared Au nanorods could be collected by centrifugation at 6000rpm for 20 minutes and re-dispersed in deionized H_2O.

Conformal Au-Ag nanorods were prepared by adding 0.5ml of 0.06M $AgNO_3$ to the diluted Au nanorods (ten times diluted from above as-synthesized Au nanorods) with gentle shaking, followed by the addition of 6ml of 0.1M AA at 60ºC. The whole solution was aged at 60ºC for 16 hours. As-prepared Au-Ag nanorods were obtained by centrifugation at 5000rpm for 12 minutes and re-dispersed in H_2O.

Non-epitaxial synthetic procedure and condition of conformal Au-CdS nanorods converted from Au-Ag nanorods were similar to those for Au-CdS nanocubes.

4.2.3 Synthesis of conformal Au-CdS nanoprisms

Synthesis of Au nanoprisms followed that of a previous report of iodide ion-controlled seed-mediated growth [148]. In a typical synthesis, the Au seed solution was prepared by mixing 0.5ml of 0.01M $HAuCl_4$, 0.5ml of 0.01M $Na_3C_6H_5O_7$ and 18ml of deionized H_2O first. 0.5ml of 0.1M ice- cooled $NaBH_4$ was quickly injected to the above mixture solution followed by vigorous stirring for 2 minutes. After that the seed solution was aged for at least 6 hours and could be used for up to a week without degradation. In order to induce anisotropic Au growth, iodide ions were introduced to act as a key shape-directing element through selectively binding to the Au (111) facet. To achieve this, iodide ions were introduced by dissolving 20μL of 0.1M KI with 50ml of 0.05M CTAB (it is worth noting that contaminant iodide ion concentration was one of the ill-characterized characteristics of as-purchased CTAB. We found levels significant enough to influence synthetic yield of Au nanoprisms. Thus we observed that different batches of

CTAB even from the same manufacturer required minor adjustment of KI concentration in order to achieve the highest yield of nanoprisms) [148]. After the aging period of the seed solution, multiple step solutions were prepared and sequentially mixed: the *Step-1* solution was prepared by mixing 0.25ml of 10mM $HAuCl_4$, 0.05ml of 0.1M NaOH, 9ml of KI solution and 0.05ml of 0.1M AA; the *Step-2* solution was prepared by mixing 2.5ml of 10mM $HAuCl_4$, 90ml of KI solution, 0.5ml of 0.1M NaOH and 0.5ml of 0.1M AA. 1ml of seed solution was then added into the *Step-1* solution and gently stirred for 30s, followed by the addition of the *Step-2* solution. Then the whole solution was aged for 15hrs.

Conformal Au-Ag nanoprisms were synthesized by modifying the procedure of a former report [149]. In a typical synthesis, 0.2ml of 0.1M AA and 40μl of 0.01M $AgNO_3$ were added to the appropriate amount of as-synthesized Au nanoprisms. 0.3ml of 0.1M NaOH was then added quickly to the above mixture solution, followed by aging for 1hour. The thickness of Ag shell could be monotonically increased by repeating above procedure.

The non-epitaxial synthetic procedure and the condition of conformal Au-CdS nanoprisms converted from Au-Ag nanoprisms were similar to those for Au-CdS nanocubes.

4.2.4 Synthesis of non-conformal spherical Au core- cubic CdS shell nanostructures

I followed a previous report to synthesize non-conformal spherical Au core and cubic Ag shell with slight modification of synthetic procedure [17]. I used 11nm- near-spherical Au nanoparticles passivated with CTAC (cetyltrimethylammonium chloride) surfactants as core nanoparticles. In a synthesis of Au nanoparticles, 6ml of 0.5mM $HAuCl_4$, 6ml of 0.2M CTAC and 4.5ml of 0.1M AA solutions were mixed first, followed by fast injection of a seed solution. The brownish seed solution was prepared by adding 0.7ml of 10mM ice- cooled $NaBH_4$ into 10ml of mixture solution of 0.25mM $HAuCl_4$ and 100mM CTAB. In order to overgrow a cubic Ag shell onto near-spherical Au nanoparticles we re-dispersed the Au core nanoparticles in 5ml of 20mM CTAC solution and the solution was loaded to a 40ml autoclave cell. 7ml of deionized H_2O, 1ml of 0.2M CTAC, 2ml of 0.01M $AgNO_3$ and 2ml of 0.1M AA were then added to the re-dispersed Au core nanoparticle solution with stirring for 5 minutes. The autoclave cell was sealed and then aged for 21 hours at 80ºC. Such hydrothermally synthesized spherical Au- cubic Ag nanostructures could be collected by centrifugation at 10000rpm for 10 minutes.

The non-epitaxial synthetic procedure and the condition of non-conformal spherical Au- cubic CdS shell were similar to those for Au-CdS nanocubes.

4.2.5 Synthesis of non-conformal octahedral Au core-cubic CdS shell nanostructures

Our synthetic procedure of non-conformal octahedral Au core-cubic Ag shell nanostructures was modified from a seed- mediated growth method in previous report [150]. The Au seed solution was prepared by rapid injection of 0.6ml of 10mM ice-cooled $NaBH_4$ to a 10ml of mixture solution of 0.25mM $HAuCl_4$ and 75mM CTAB with vigorous stirring. The seed solution was aged for 1 hour and then diluted by a factor of 100 before usage. A five-times diluted solution of a mixture consisting of 0.1ml of 10mM $HAuCl_4$, 4ml of 0.1M CTAB and 1.5ml of 0.1M AA was further mixed with 0.3ml of diluted Au seed solution, and then aged for 6 hours at room temperature without stirring. After the aging period, 0.6ml of 0.01M $AgNO_3$ and 2.4ml of 0.1M AA were directly added to the octahedral Au nanoparticles solution with stirring for 10 minutes, and the whole solution was transferred to a 40ml autoclave cell with a seal and then aged at 80ºC for 24 hours. The Au-Ag core-shell could thus be collected by centrifugation at 6000rpm for 30 minutes. The thickness of the cubic Ag shell could be fine tuned by changing concentration of $AgNO_3$ and/or AA solutions.

The non-epitaxial synthetic procedure and the condition of non-conformal octahedral Au- cubic CdS shell were similar to those for Au-CdS nanocubes.

4.2.6 Synthesis of coaxial one- dimensional Au-CdS nanowires

In the current work, I have synthesized and compared Au nanowires of two different diameters, 30nm and 60nm, with lengths up to 5μm by modifying a three-step seeding method taken from the literature [151, 152]. In a typical synthesis for 30nm Au nanowires, two different solutions, the seed solution and the growth solution, were prepared first. The seed solution was prepared by rapid injection of 1ml of 0.1M ice-cooled $NaBH_4$ into a mixture of 1ml of 10mM $HAuCl_4$, 36ml of deionized H_2O and 1ml of 20mM $Na_3C_6H_5O_7$ with stirring. The growth solution was initially prepared by mixing 30ml of 0.1M CTAB with 0.75ml of 0.01M $HAuCl_4$. This growth solution was then distributed into three separated vials labeled as *A*, *B* and *C* that contained 2.25ml, 2.25ml and 22.5ml of growth solution, respectively. 0.0125ml of 0.1M AA was added to vials *A* and *B*, while 0.125ml of 0.1M AA and 0.1ml of concentrated nitric acid were added to vial *C*. Once seed and growth solutions were ready, 0.2ml of the seed solution was added to vial *A* and was stirred for 3s first. Then 0.2ml of solution in vial *A* was transferred to vial *B* and was stirred for 5s. Lastly, 0.2ml of solution in vial *B* was transferred to vial *C* and was stirred for 5s. This final solution was kept at room temperature for 18 hours, and was diluted by the addition of 25ml of deionized H_2O. Au nanowires synthesized by such three-step seed growth could be collected by centrifugation at 2000rpm for 15 minutes, and was re-dispersed well in deionized H_2O. Synthesis of 60nm- Au nanowires followed almost the same procedure as described above, except that only 0.1ml of solution in vial *B* was transferred to vial *C* in the second step.

A typical synthetic condition for overgrowth of the Ag shell was as follows: Au nanowire colloid was collected by centrifugation at 2000rpm for 15 minutes and re-dispersed in 1.5ml of 50mM CTAB aqueous solution. 0.5ml of 0.1M AA and 0.16ml of 0.01M $AgNO_3$ solutions were added drop by drop to the Au nanowires solution, and then 0.75ml of 0.1M NaOH was added with gentle shaking for 1 minute, followed by aging for 3 hours at room temperature. These conditions were used for both 30nm and 60nm diameter Au core nanowires (for 60nm size Au core nanowires, the thickness of overgrown Ag shell was observed to be smaller than that of Ag shell grown onto 30nm-Au core nanowires under the same condition). The thickness of the overgrown Ag shell could be controlled by simply changing the Ag concentration.

As grown Au-Ag coaxial nanowires with 30nm Au core diameter were collected by centrifugation at 2000rpm for 15 minutes, and were re-dispersed in 1ml of 10% $C_{10}H_{22}S$ acetone solution with sonification for 2 minutes for ligand exchange. After that, thiols-recapped Au-Ag coaxial nanowires were collected by centrifugation at 2000rpm for 10 minutes, and a similar ligand exchange process was repeated for a second time. 0.5ml of 10% $C_{10}H_{22}S$ solution was diluted in 5ml acetone and was applied to re-disperse thiols-recapped Au-Ag nanowires. 2ml of S-precursor was added and reacted with Au-Ag nanowires at 60ºC for 1.5~2 hours with vigorous stirring. Once the reaction was complete and the Ag shell was converted to amorphous Ag_2S shell, Au-Ag_2S was collected by centrifugation at 3000rpm for 15 minutes and then was re-dispersed in 1ml of 10% $C_{10}H_{22}S$ acetone solution by sonification for 2 minutes, followed by aging for 14 hours. The Au-Ag_2S nanowires recapped with $C_{10}H_{22}S$ surfactants were collected by centrifugation at 3000rpm for 5 minutes. The cation exchange process between Ag and

Cd ions was initiated by re-dispersing as-obtained Au-Ag_2S in 8ml of toluene with addition of 0.02ml OA (oleic acid), 0.01ml OAm (oleylamine) and 2ml of room-temperature saturated $Cd(NO_3)_2$ in methanol solution, followed by 10 drops of fresh TBP. The whole solution was sealed in 50ml plastic tubes and heated at 90ºC for 4 hours. This process was stopped by adding excess ethanol solution, and then the final product was collected by centrifugation at 2000rpm for 10 minutes. For non-epitaxial growth of Au-CdS coaxial nanowires with 60nm Au core diameter, a similar procedure was followed except that it typically took up to 7 hours for the whole cation exchange and grain growth process and it required much more vigorous stirring in order to achieve high yield of monocrystalline CdS shell.

4.3 Shape Controlled Synthesis of Monocrystalline Semiconductor Based Core-Shell Nanostructures

The central of our shape- control strategy is illustrated in Figure 4.1.

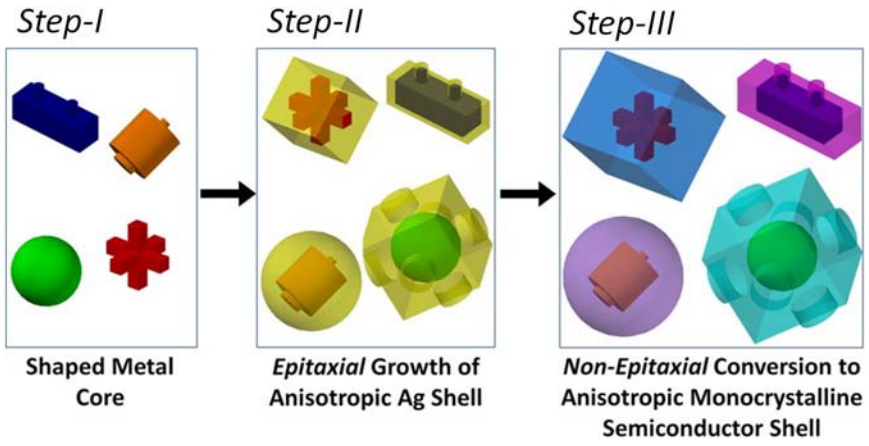

Figure 4.1 Illustration of novel synthetic route to achieve anisotropic monocrystalline semiconductor based hybrid core-shell nanostructures with conformal and non-conformal geometry. Step *I*: Synthesis of various anisotropic metal core nanostructures; Step *II*: Conformal and non-conformal growth of bimetallic core-shell nanoparticles via epitaxial growth; Step *III*: Morphology- preserved non- epitaxial conversion of anisotropic metal shell to monocrystalline semiconductor shell.

In order to circumvent the challenges of direct shape control of metal core and semiconductor shell due to their substantial structural dissimilarity, I start with binary metallic core-shell nanostructures, whose morphology features of both core and shell can be easily tailored by maneuvering the surface energy and chemistry among different crystal planes with the assistance of capping surfactants [136, 141]. Once a binary metallic core-shell nanostructure with the desired morphology is achieved, molecules, such as alkanethiols that can possess very high chemical affinity to metals, are applied to

form strong interfacial thiol-metal bonds to the shell surfaces and to offer regulation of chemical thermodynamics in the successive chemical transformation processes [153, 154]. Metal shells recapped with alkanethiol molecules therefore provide shaped platforms in which the desired monocrystalline semiconductor compounds (independent of core's morphology and crystallinity) can be non-epitaxially converted, which is based on a Lewis acid-base reaction with the preservation of shell morphology [145]. While in principle our shape-control strategy, illustrated in Figure 4.1, should not pose limitations on the metal element of the shell, silver (Ag) was chosen for all of the studies in this report, based on the following considerations to facilitate generality of our approach: (1) Ag has served as an ideal platform for understanding metallic shape evolution mechanisms, exhibiting a high degree of rich shape control in solution [138]; and (2) Ag possesses extremely high soft Lewis acidity as compared with many other metals and can thus enable chemical transformation to form various semiconductor within shaped shell matrix [145]. I further take an Au-CdS core-shell as a model system to investigate in detail various conformal and non-conformal morphology controls, as depicted in Figure 4.1.

4.3.1 Conformal Au-CdS Core-Shell Nanostructures

Figure 4.2 and Figure 4.3 exemplify and compare conformal Au-Ag and corresponding Au-CdS anisotropic core-shell nanostructures with rod-, prism- and cubic-geometry. The low- resolution bright field TEM images show the overall morphologies

and uniformity of as-synthesized core-shell nanostructures. All samples were characterized as prepared without further purification. By comparing with the morphology of the corresponding Au-Ag core-shell structures (Figure 4.2) from which hybrid structures are converted as shown in Figure 4.3, a clear injective morphology relationship can be established between the Au-Ag core-shell and the Au-CdS core-shell. The shape of binary metallic core-shell can be exclusively preserved after being chemically transformed to semiconductor shells. Importantly, in addition to the anisotropic characteristics and control, high- resolution TEM characterization further reveals the monocrystalline structure of shaped semiconductor shell that is unrelated to both the core and shell geometry. The crystalline perfection of the as-grown semiconductor shell can be further revealed by different position characterization, which unambiguously confirms defect- free single crystalline feature of semiconductor shell even with anisotropic confinement.

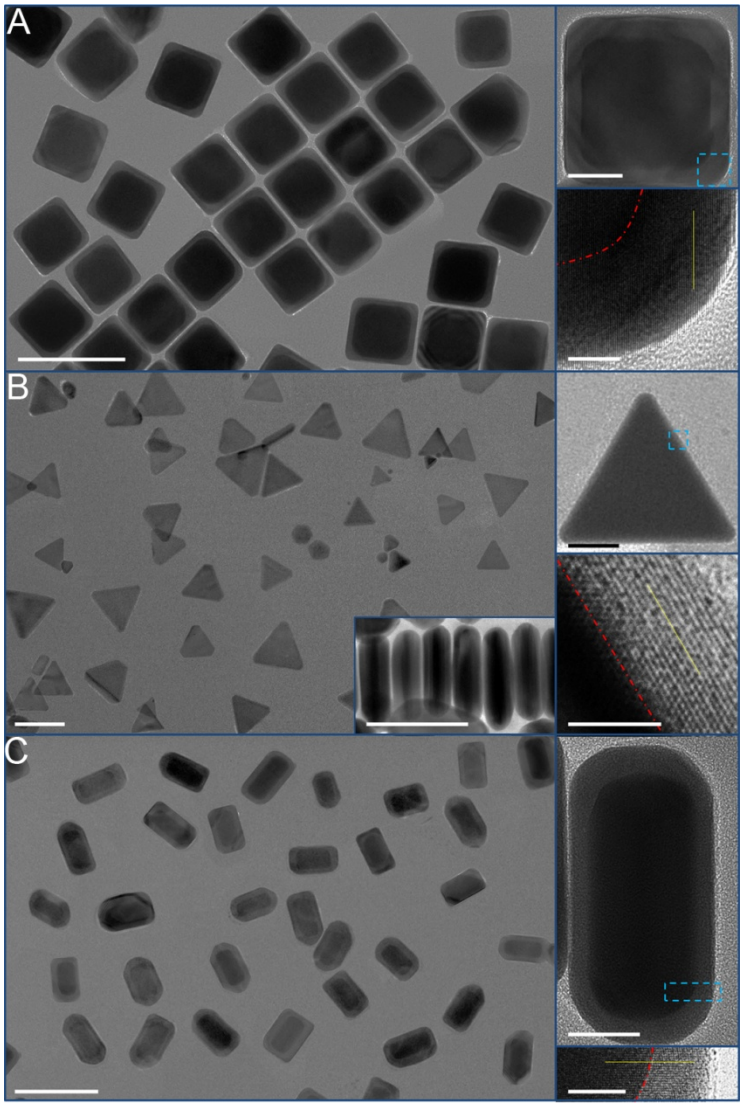

Figure 4.2 Conformal Au-Ag core-shell nanostructures. TEM characterization of: (A) Nanocubes. (Left) Large scale TEM image. Scale bar, 100nm. (Top-right) TEM image of a single nanocube. Scale bar, 20nm. (Bottom-right) High- resolution TEM image of blue outlined area in (Top-right). Scale bar, 5nm. (B) Nanoprisms. (Left) Large scale TEM image. Scale bar, 100nm. Inset, TEM image showing cross-section of Au-Ag prism. Scale bar, 100nm. (Top-right) TEM image of a single nanoprism. Scale bar, 20nm. (Bottom-right) High- resolution TEM image of blue outlined area in (Top-right). Scale bar, 5nm. (C) Nanorods. (Left) Large- scale TEM image. Scale bar, 100nm. (Top-right) TEM image of a single nanorod. Scale bar, 20nm. (Bottom-right) High- resolution TEM image of blue outlined area in (Top-right). Scale bar, 5nm. For (A) to (C), red dashed line and yellow solid line represent bimetallic interface and shell lattice orientations.

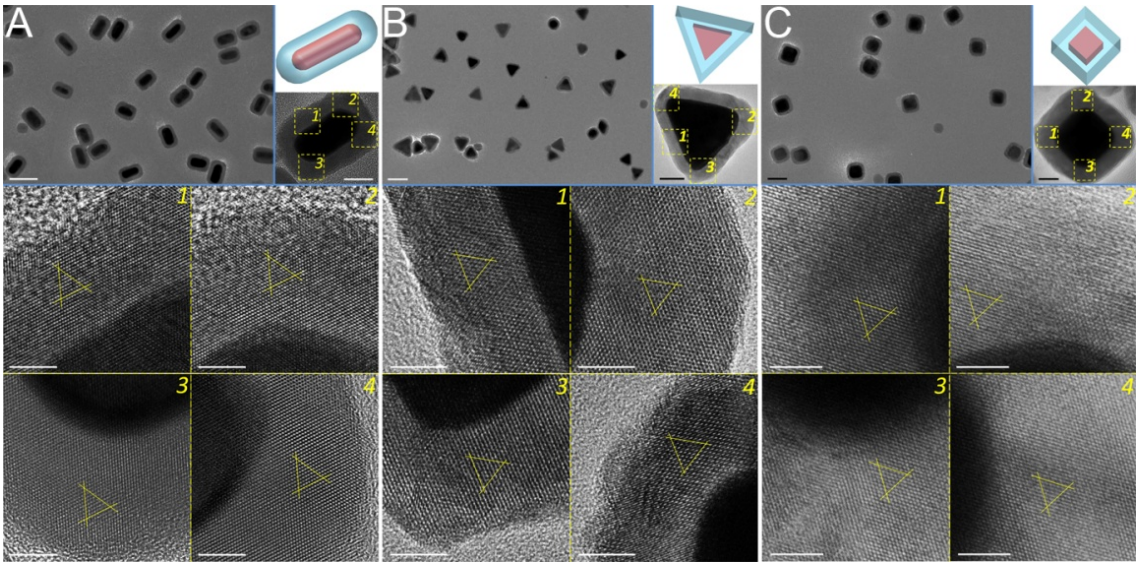

Figure 4.3 Conformal Au-CdS core-shell nanostructures. (A) Nanorod morphology; (B) Nanoprism morphology; (C) Nanocube morphology: (Top-left) Large scale TEM image. Scale bar, 100nm. (Top-right) Core-shell model and typical TEM image of a single core-shell nanostructure. Scale bar, 20nm. (Bottom) Area- dependent high- resolution TEM images of labeled selective areas in (Top-right), highlights perfect monocrystalline feature. Scale bar, 5nm. Yellow lines highlight lattice orientation of CdS shell. Different areas of a single anisotropic CdS shell all manifest identical lattice orientation without detectable structural defects.

4.3.2 Non- conformal Au-CdS Core-Shell Nanostructures

I have further applied the same shape- control scheme in Figure 4.1 to achieve more complex non-conformal metal-semiconductor core-shell nanostructures, possessing distinct core and shell geometries. Figure 4.4 and Figure 4.5 exemplify and compare non-conformal Au-Ag and corresponding Au-CdS anisotropic core-shell nanostructures with cubic shell but different metal Au core shapes.

Similar to the conformal core-shell geometries shown in Figure 4.2 and Figure 4.3, non-conformal cubic shell morphology that is unrelated to the core shape also exclusively originates from the cubic morphology of the Ag shell (Figure 4.4). Further high-resolution TEM characterization at different positions confirms monocrystalline feature of both cube- shaped CdS shells, even though they retain different interfaces with distinct facets of the Au cores. Our achievement of both conformal and non-conformal hybrid core-shell nanostructures, as demonstrated in Figure 4.3 and Figure 4.5, highlight the uniqueness of this novel shape control scheme to achieve simultaneously two independent critical fundamental materials characteristics: shape and monocrystallinity, which cannot be possible from other techniques, including the conventional epitaxial method.

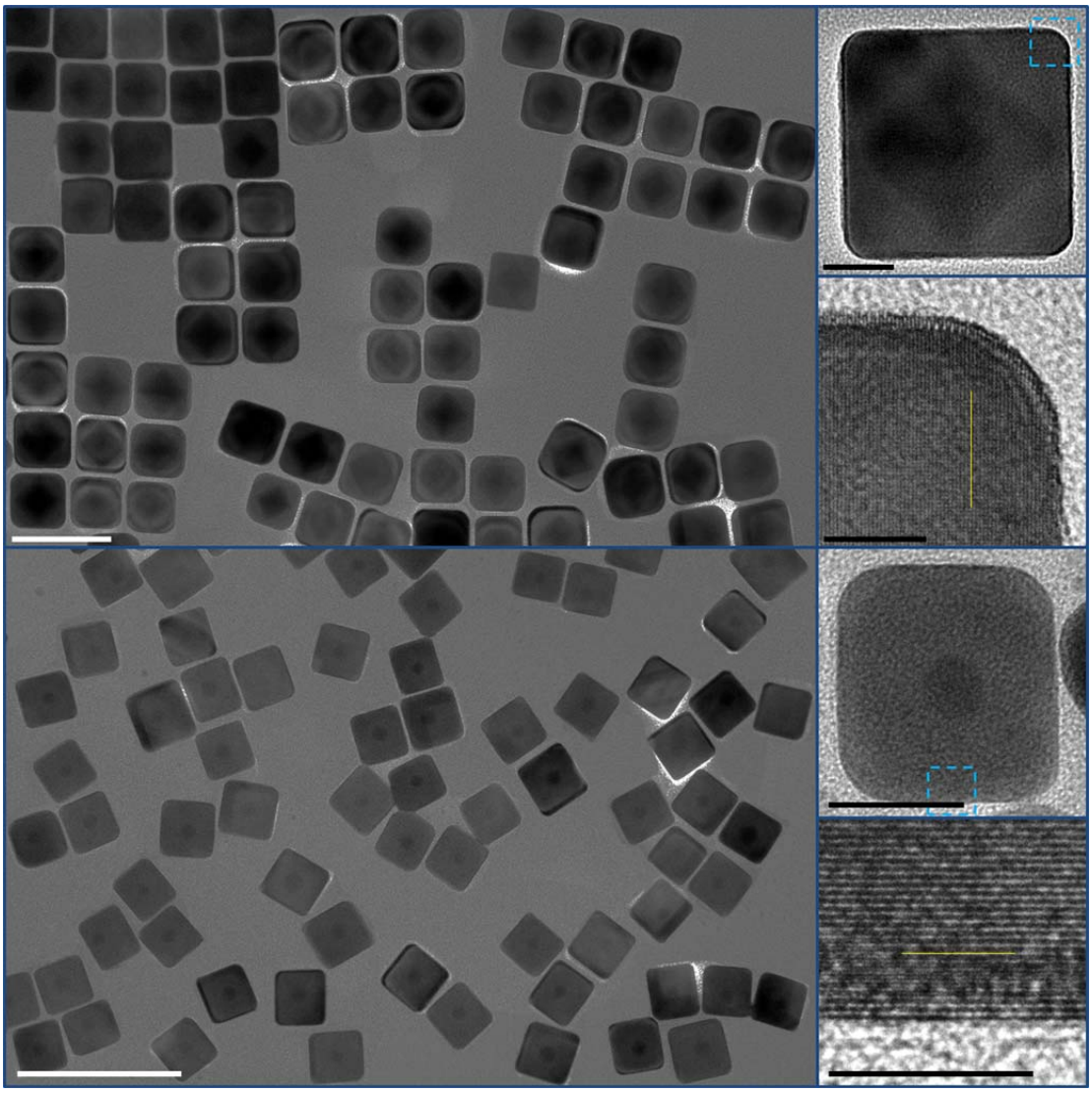

Figure 4.4 Non-conformal Au-Ag core-shell nanostructures. TEM characterization of: (A) Spherical core-cubic shell. (Left) Large- scale TEM image. Scale bar, 100nm. (Top-right) TEM image of a single core-shell nanostructure. Scale bar, 20nm. (Bottom-right) high-resolution TEM image of blue outlined area in (Top-right). Scale bar, 5nm. (B) Octahedral core-cubic shell. (Left) Large- scale TEM image. Scale bar, 100nm. (Top-right) TEM image of a single core-shell nanostructure. Scale bar, 20nm. (Bottom-right) High- resolution TEM image of blue outlined area in (Top-right). Scale bar, 5nm.

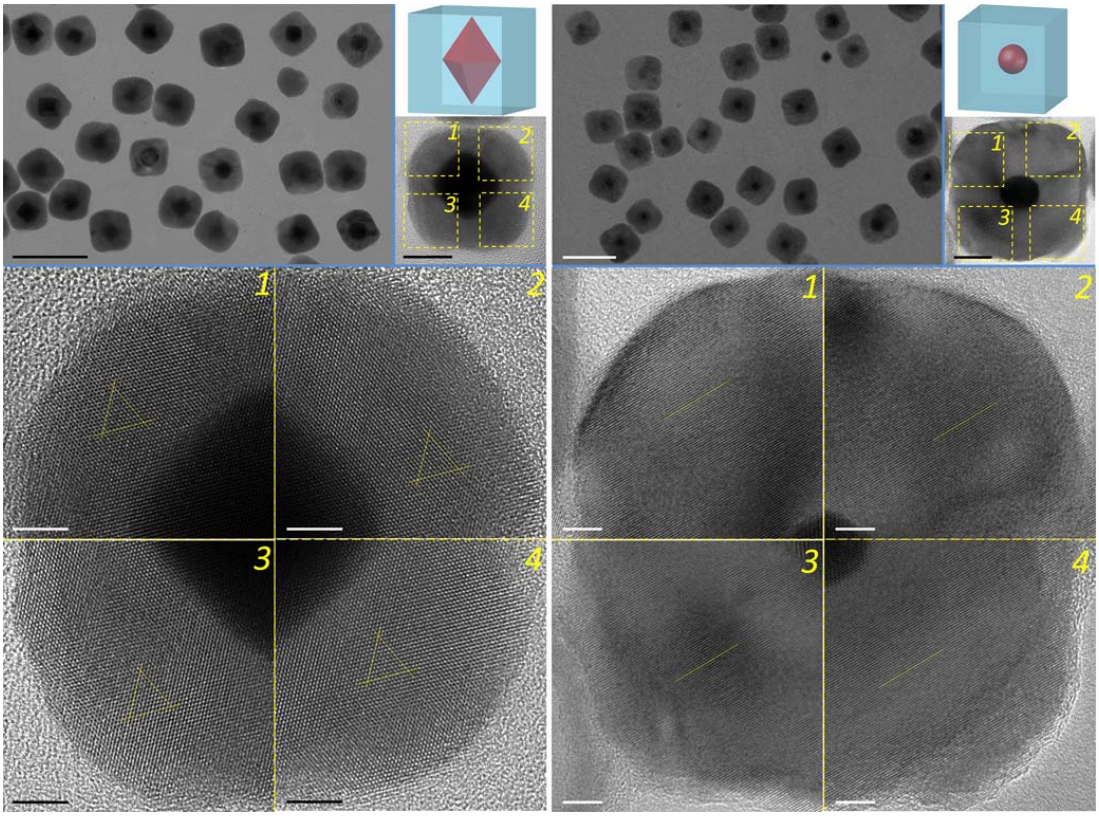

Figure 4.5 Non- conformal Au-CdS core-shell nanostructures with cubic CdS shell. (A) Spherical Au core; (B) Octahedral Au core. (Top-left) Typical large- scale TEM image. Scale bar, 100nm. (Top-right) Core-shell model and TEM image of a single core-shell nanostructure. Scale bar, 20nm. (Bottom) Area- dependent high- resolution TEM images of labeled selective areas in (Top-right), highlighting perfect monocrystalline feature. Scale bar, 5nm. Yellow lines represent lattice orientation of CdS shell. Dark contrast area is Au core. Different areas of a single CdS shell all manifest identical lattice orientation without detectable structural defects.

4.3.3 One-dimensional Coaxial Au-CdS Core-Shell Nanostructures

This approach can further provide a tantalizing opportunity to obtain even more intricate and larger scale metal-semiconductor heterostructures with precise structure and dimensionality tailoring, such as one-dimensional metal core- semiconductor shell nanostructures. It is worth noting that while one- dimensional coaxial heterostructures are considered as a critical breakthrough in the development of nanowire building blocks with important applications in such as nanoprocessors [155], nanolasers [156], multistate memory [157], nano-photovoltaics [158] and nanophotonics [159], hybrid metal-semiconductor coaxial structures as demonstrated in Figure 4.7 have been lacking due to substantial synthetic difficulties [160].

Figure 4.6 shows chemically synthesized Au core nanowires with a diameter of 60nm. The selected area electron diffraction (SAED) pattern from the Au nanowires, shows two sets of interpenetrated zone patterns (i.e., 112 and 100 zone patterns, labeled by red and green typefaces, respectively) from a *fcc* structure. Both high- resolution images and electron diffraction patterns are consistent with nanowire structure proposed and determined in former reports [146, 151, 161, 162], in which nanowire represents a cyclic penta-twinned crystal with twin boundaries arranged radially to the long axis.

Figure 4.7 shows one-dimensional coaxial metal-semiconductor cables possessing monocrystalline CdS shells, which are grown from Au core nanowires presented in the Figure 4.6. Coaxial Au-CdS nanowires are uniformly grown with length up to a few micron- meters with Au core diameter of 60 ± 5nm (Figure 4.7(A)). A typical TEM

image of a single coaxial Au-CdS nanowire is further presented in Figure 4.7(B), revealing the core-shell configuration with uniformity. Even though the crystallography of as-synthesized anisotropic Au core nanowires has been shown to manifest a [110] growth orientation along their long axis with (100) facets on the side (Figure 4.6) [151, 152], a series of high- magnification TEM images along Au-CdS nanowires (Figure 4.7(c)) have explicitly revealed both an intact and uniform non-epitaxially grown CdS Wurtzite lattice and atomically smooth interfaces along the whole nanowire, including two sharp ends with high curvature. Both interfacial smoothness at the atomic level and defect- free monocrystallinity of semiconductor shell are crucial for a high performance device with enhanced novel electronic and photonic functions.

Importantly, we have observed up to 5μm long coaxial nanowires with perfect monocrystalline CdS shells, whose lengths are merely limited by that of the as-synthesized Au core nanowires (Figure 4.8).

Similar coaxial Au-CdS nanowires can also be achieved with tunable core diameters and semiconductor shell thickness by finely tailoring the dimensionality of conforming Au-Ag core-shell nanowires, as demonstrated in Figure 4.9 for Au core diameter of 30nm and Figure 4.10 for different shell thickness.

Such precise control of the dimensionality and monocrystallinity should allow tunable coupling between, e.g., the quantum confinement of semiconductor shells and localized surface plasmon resonance of metal core nanowires, to enable new physics and device concepts. While hybrid core-shell nanostructures highlighted in Figure 4.3, Figure 4.5, Figure 4.7, Figure 4.8, and Figure 4.9 manifest various anisotropic morphology

combination between core and shell, there exists one common feature of monocrystalline CdS shells: there is no preferred crystallographic texture of semiconductor shell (relative to their anisotropic morphology), which is consistent with the nature of the non-epitaxial crystalline growth process [145]. This feature can also be revealed by comparing different Au-CdS core-shells possessing the same core diameter and shell thickness, as shown in Figure 4.11.

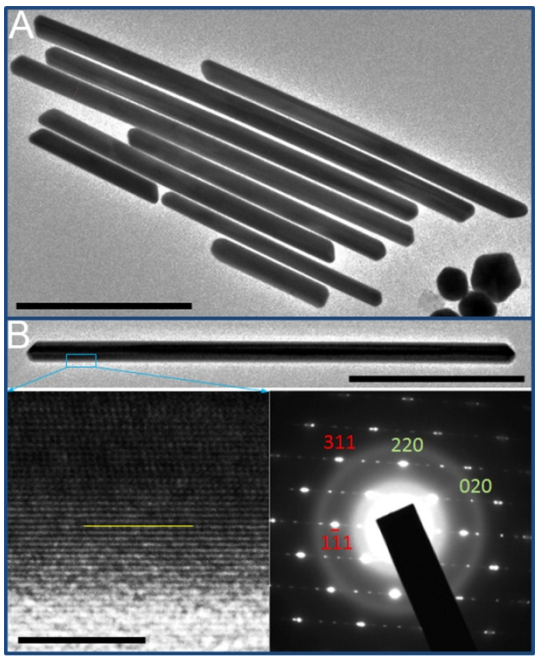

Figure 4.6 Chemically synthesized Au nanowires with diameter of 60nm. (A) Large scale TEM image of as- synthesized Au nanowires. Scale bar, 500nm. (B) (Top) TEM image of a single Au nanowire. Scale bar, 500nm. (Bottom-left) High- resolution TEM image of blue outlined area in (Top), showing [110] growth direction along their long axis with the sides bound with the {100} surface. Scale bar, 5nm. (Bottom-right) Selected area electron diffraction pattern of Au nanowires, showing two sets of interpenetrated zone patterns (i.e., 112 and 100 zone patterns, labeled by red and green typefaces, respectively) from a *fcc* structure. Both high- resolution images and electron diffraction patterns are consistent with nanowire structure proposed and determined in former reports [146, 151, 161, 162], in which nanowire represents a cyclic penta- twinned crystal with twin boundaries arranged radially to the long axis.

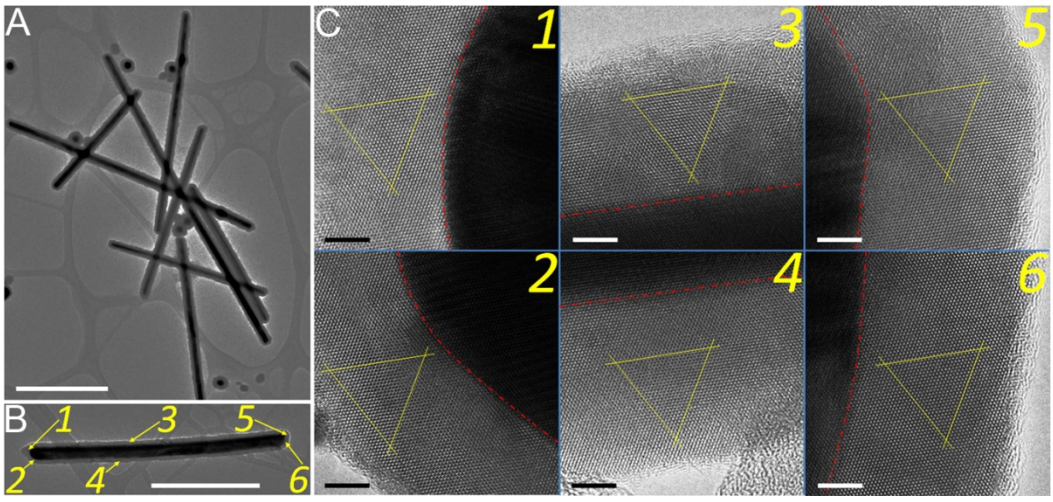

Figure 4.7 Coaxial nanowires with Au core diameter of 60nm and monocrystalline CdS shell. (A) Large- scale TEM image of Au-CdS nanowires with different lengths. Scale bar, 500nm. (B) Typical TEM image of a ~1.2μm long single coaxial nanowire. Scale bar, 500nm. (C) Area- dependent high- resolution TEM characterization from selective areas labeled in (B); Scale bar, 5nm. Yellow lines are guides to the lattice orientation. Red dashed lines highlight metal-semiconductor interface with different curvatures.

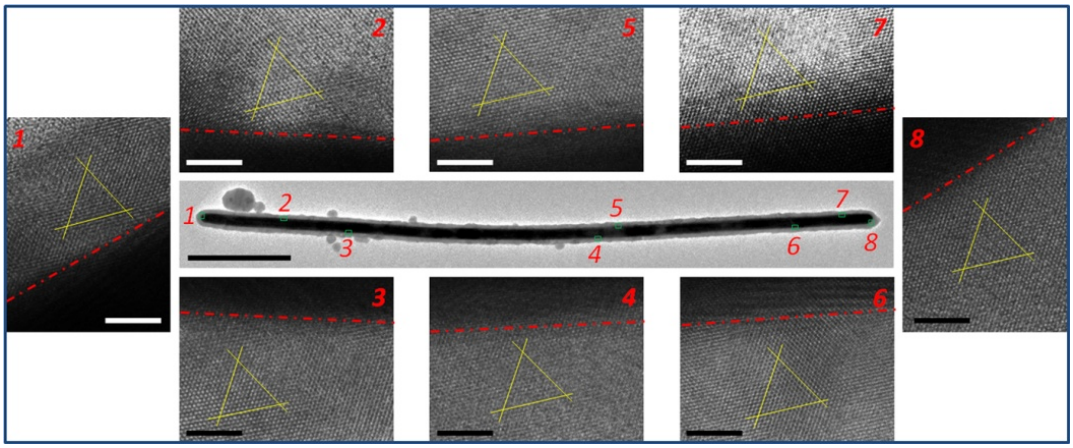

Figure 4.8 A ~3.2μm long coaxial Au-CdS nanowires with Au core diameter of 60nm. (Center) TEM image of an intact nanowire, showing slightly bent morphology. Scale bar, 500nm. Area- dependent high- resolution TEM images of eight numerically labeled selective areas as highlighted in (Center), showing perfect monocrystalline feature and identical lattice orientations (yellow solid line) along the whole nanowire that are independent on the local curvature. Red dashed line represents metal-semiconductor interface, possessing different local curvature. Scale bar, 5nm.

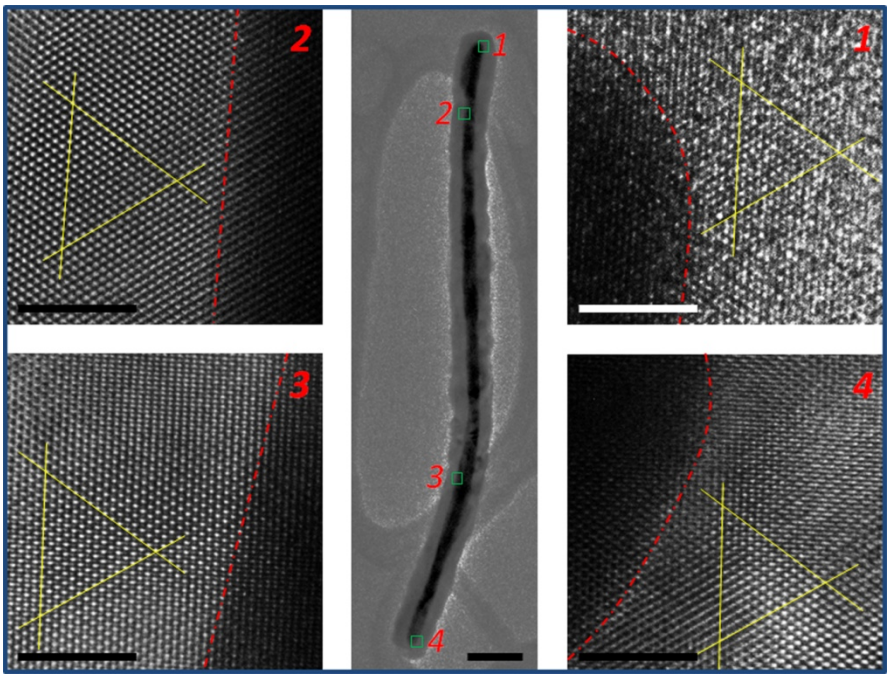

Figure 4.9 A ~1.2μm long coaxial Au-CdS nanowires with 30nm Au core diameter. (Center) TEM image of a whole nanowire, showing slightly bent morphology. Scale bar, 100nm. Area- dependent high- resolution TEM images of four numerically labeled selective areas as highlighted in (Center), showing perfect monocrystalline feature and identical lattice orientations (yellow solid line) along the whole nanowire that are independent on the local curvature. Red dashed line represents metal-semiconductor interface, possessing different local curvature. Scale bar, 5nm.

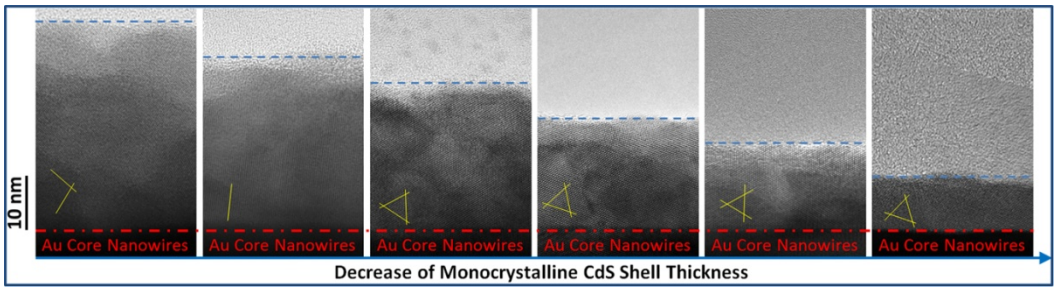

Figure 4.10 High- resolution TEM images of a set of six different coaxial Au-CdS nanowires, possessing same 60nm Au core diameter but different shell thickness of monocrystalline CdS. Blue and red dashed lines represent CdS shell external surface and Au-CdS interface, respectively. Yellow solid line highlights lattice orientations.

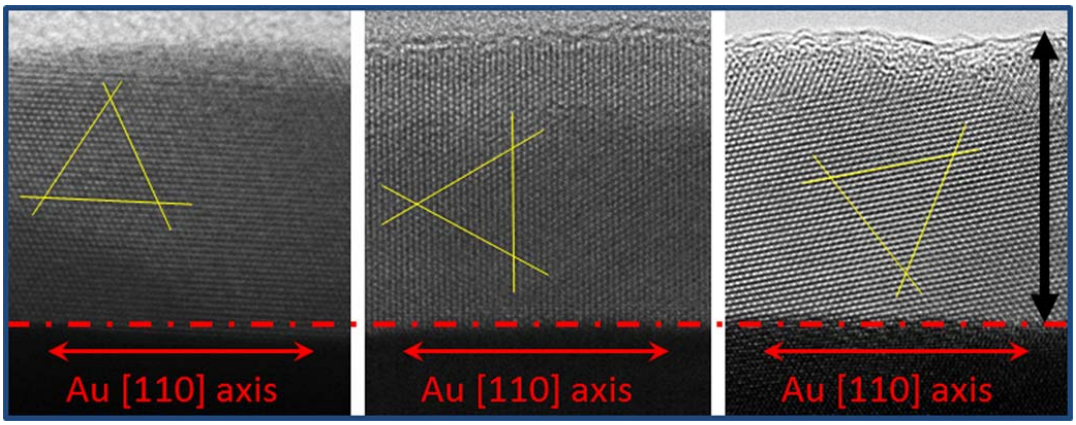

Figure 4.11 High- resolution TEM images of a set of three different coaxial Au-CdS nanowires, possessing the same Au core diameter (60nm) and CdS shell thickness (black arrow, 16.6nm). While all these nanowires manifest perfect monocrystalline structure, lattice orientations (yellow solid lines, relative to the Au core [110] long axis) are distinct among three nanowires. This comparison highlights the nature of the non-epitaxial crystalline growth, in which no preferred crystallographic texture exists. Red dashed line represents metal-semiconductor interface.

4.4 Underlying Mechanisms of Shape Control and Monocrystalline Semiconductor Growth Spanning from Nanometer- to Micrometer- Scale

From a thermodynamics viewpoint, a grand challenge of anisotropic nanostructures is to preserve their structures with high surface curvature. It is generally believed that anisotropic nanostructures containing sharp features on the surface, such as metallic Au cubes and prisms, are not stable after synthesis and can evolve spontaneously into structures with lower surface energy [138]. However, all of the anisotropic metal-semiconductor core-shell nanostructures demonstrated in Figure 4.3, Figure 4.5, Figure 4.7, Figure 4.8, and Figure 4.9, show stability for months without noticeable change of overall morphology as well as quality of the semiconductor shell. On the other hand, in order to retain shell morphology during chemical transformation process we have observed that the addition of alkanethiols molecules to passivate surface of bimetallic core-shell nanostructures plays a key role. I observed that surface passivation with alkanethiol molecules is critical for shape preservation and reaction- kinetics control during the whole chemical transformation process. I have also investigated effect of alkyl chain length (n) of alkanethiols ($C_nH_{2n+2}S$) by comparing n=10, 14 and 16. So far we have not observed any conclusive length dependence of both monocrystalline growth and shape preservation. Therefore, only results involving $C_{10}H_{22}S$ molecules are presented in the current report.

A few control experiments have clearly revealed role of alkanethiols for shape preservation: (1) conversion from Ag to Ag_2S shell with the absence of alkanethiols molecules always leads to irregular and rough morphology. This is consistent with former

study that showed that the chemical transformation kinetics involving anisotropic metals can show dramatic differences along different directions, and that the reaction rate is the fastest at the sharp corner sites, leading to structural deformation with progression of reaction [163]; (2) passivation of alkanethiols onto Ag shell surface can allow tight control of reaction kinetics (therefore degree of chemical transformation can by controlled by concentration of alkanethiols and reaction time), which has led to homogeneous reaction between Ag and S over the whole surface instead of corner sites only [163]. Such tight control is particularly critical for preserving morphology under massive lattice transformation during the reaction; and (3) existence of alkanethiols can further significantly regulate kinetics of cation exchange and crystalline grain growth processes. Compared with a former study on non-epitaxial crystalline growth in small sized spherical nanostructures [145], the dimensions of anisotropic core-shell structures considered here are typically much larger, therefore multiple nucleation events as well as grain domain interactions cannot be negligible. I have observed that surface passivation with a high density of alkanethiols can efficiently inhibit the cation exchange process, while introduction of labile oleylamine molecules can assist ion diffusions and exchanges through outward surface of amorphous Ag_2S matrix. Therefore a judicious combination of alkanethiol and oleylamine molecules can offer a method to maneuver entire cation exchange process and thus total number of initiated nanocrystalline nucleation sites in a large amorphous Ag_2S shell matrix. For example, under a typical synthetic condition with appropriate surface passivation of alkanethiols and oleylamine molecules, on average two spontaneous nanocrystalline CdS nucleations occur over 1-μm length scale in an amorphous Ag_2S matrix at the initial stage of cation exchange process. This

experimental observation strongly suggests that the underlying monocrystalline growth mechanism of anisotropic nanostructures with large aspect ratio should be profoundly different from that of the earlier report on non-epitaxial crystalline growth at the small scale, in which only one nucleation site occurs [145], and should open up a new avenue to explore unique grain growth in a confined region bridging from the nano- to the micron- scale that will be otherwise difficult.

I have characterized in detail the kinetic non-epitaxial growth process of monocrystalline CdS in a set of coaxial nanowires with core diameter of 60nm and length around 1.2μm (Figure 4.7(B) and (C)), by both time-dependent structural imaging (Figure 4.12 (A)-(G)) and statistics analysis of evolution of grain size distribution (Figure 4.12(H)).

The structures and chemical compositions of different domains at various growth stage presented in the Figure 4.12 were assigned by carrying out in-depth high resolution TEM imaging and single point EDS measurement, as illustrated in Figure 4.13.

I start from the reaction stage of the formation of amorphous Ag_2S passivated with majority surfactant of alkanethiols mixed with minority oleylamine molecules (Figure 4.12(A)). Similar to former study of non-epitaxial growth at the smaller dimension [145], every crystalline nucleus spontaneously forms as soon as cation exchange is initiated on the surface of nanowires, and can rapidly grow along both axial and radial directions to enlarge the crystalline domain.

As a result, only crystalline CdS grains and amorphous Ag_2S matrix are observed at the very early growth stage (Figure 4.12(B)). With time, the evolution of the

amorphous phase of CdS appears, then co-exists with amorphous Ag_2S and crystalline CdS domains, and can eventually fully substitute amorphous Ag_2S (Figure 4.12(C) and (D)), signifying that ions diffusion is faster than crystalline grain growth. For coaxial nanowires with 60nm Au core and 1.2μm length, entire cation exchange process can take about 2 hours.

It is worth noting that in addition to the crystalline nuclei initiated by cation exchange crystalline nucleation can also occur and grow inside amorphous CdS matrix after cation exchange process as shown in Figure 4.14, which can be attributed to mechanical shear deformation of amorphous shell matrix as predicted by molecular dynamics simulation [164, 165]. This has led, on average, to four independent nucleation sites over a 1-μm length scale and obscured the grain growth interactions.

In order to quantify the nanoscale crystalline growth kinetics in this chapter I also carried out a histogram analysis of the grain size at different growth stages. Since the shell thickness in current study was typically smaller than the averaged domain size and the length of nanowires, size of crystalline domain was defined as the domain lateral size *d*, and was measured by high resolution TEM characterization. In order to ensure that the analysis of grain growth was statistically significant, over 50 coaxial nanowires with average lengths of 1.2μm were measured and calculated for each set of data. The colored solid line in Figure 4.12(H) represents Gaussian fits to the data, with the accompanying coefficients (α, σ) (where α is the mean value of domain size and σ is the full width at half maximum) for each fit provided below: For growth stage 12**C** – red curve fit (0.15, 0.055); For growth stage 12**D** – red curve fit (0.50, 0.060), green curve fit (0.28, 0.085); For growth stage 12**E** – red curve fit (0.65, 0.055), green curve fit (0.40, 0.098); For

growth stage 12**F** – red curve fit (0.90, 0.077), blue curve fit (0.55, 0.072), purple curve fit (0.28, 0.073); For growth stage 12**G** – red curve fit (0.116, 0.057);

Non-epitaxial grain growth initiated by the cation exchange process qualitatively follows normal grain growth model in an amorphous matrix, with manifestation of monotonic increase of averaged domain size with time (Figure 4.12(C)-(E)). However, compared with an ideal unimodal normal grain growth that typically occurs in two-dimensional thin films, a clear existence of bimodal normal grain distribution arise as a mixture of two distinct nucleation events with different underlying mechanisms, which is consistent with our TEM observation: one from initial cation exchange process induced by chemical energy [145] and the other from later nucleation within an amorphous matrix driven by such as mechanical energy [165]. However, normal grain growth itself can eventually lead to stagnation of crystalline domains. A surprising key feature of histogram analysis shows the multimodality of grain size distribution during subsequent grain development, which qualitatively agrees with an abnormal grain growth scenario originally proposed for recrystallization in two- dimensional thin films [166]. Such abnormal grain growth often leads to a population of domain with favored lattice orientation at the expense of a static matrix of normal grains, and eventually leads to monocrystallinity of our core-shell nanostructures (Figure 4.12(G) and (H)). Clear supporting evidence for abnormal grain growth is the observation of an intermediate stage, showing transition between two domains, as shown in high resolution TEM image (Figure 4.12(F)).

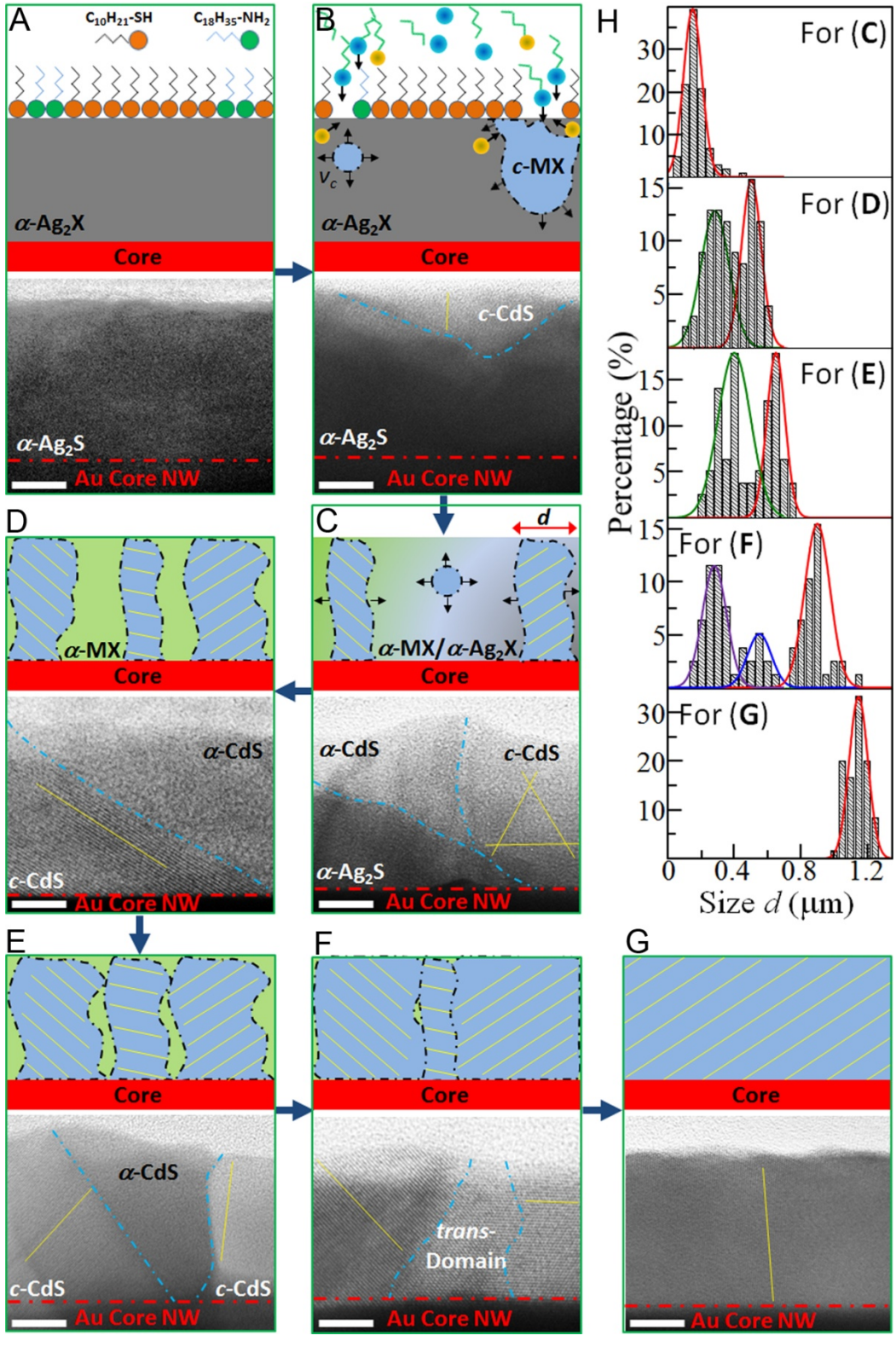
A
$C_{10}H_{21}$-SH
$C_{18}H_{35}$-NH$_2$
α-Ag_2X
Core
α-Ag_2S
Au Core NW
B
V_C
c-MX
α-Ag_2X
Core
c-CdS
α-Ag_2S
Au Core NW
C
d
α-MX/α-Ag_2X
Core
α-CdS
c-CdS
α-Ag_2S
Au Core NW
D
α-MX
Core
α-CdS
c-CdS
Au Core NW
E
Core
α-CdS
c-CdS
c-CdS
Au Core NW
F
Core
trans-
Domain
Au Core NW
G
Core
Au Core NW
H
For (C)
For (D)
For (E)
For (F)
For (G)
Percentage (%)
Size d (μm)
0
0.4
0.8
1.2

Figure 4.12 Non- epitaxial grain growth kinetics in coaxial Au-CdS nanowires with core diameter of 60nm and averaged length of 1.2μm. (A)–(G) Schematic model (top) and high- resolution TEM characterization (bottom) of grain nucleation and evolution at different reaction stage. In TEM images, red dashed line, blue dashed line and yellow solid lines highlight Au-CdS interface, grain boundary and CdS lattice orientation, respectively. Scale bar, 10nm. (A) Amorphous Ag_2X (α-Ag_2X, X=chalcogenides, As, P anions) shell capped with majority alkanethiols and minority oleylamine molecules. (B) Cation exchange induced semiconductor crystalline nucleation (*c*-MX, M=metal cations) in an amorphous matrix. Green zigzag line represents TBP molecule. Blue and yellow spheres represent semiconductor cation M and Ag ion, respectively. Arrow highlights ion diffusion direction. (C) Coexistence of α-Ag_2X, *c*-MX and amorphous semiconductor (α-MX) due to faster cation exchange speed than crystalline growth speed. Color gradient background in schematic model represents mixture phase of α-Ag_2X and α-MX. (D) Completeness of cation exchange process that α-Ag_2X is fully converted to either *c*-MX or α-MX. New crystalline nucleation can occur and grow in amorphous matrix driven by mechanical shear deformation of nanowires. (E) Normal crystalline domain growth in α-MX. (F) Occurrence of abnormal grain growth when two mis-oriented domains meet, which can lead to continuous growth of one domain lattice at the expense of the other. (G) Formation of monocrystalline semiconductor shell by abnormal grain growth pathway. (H) Histograms of grain size (*d*) distribution at different growth stages from (C) to (G). The color solid line represent Gaussian fits to the data.

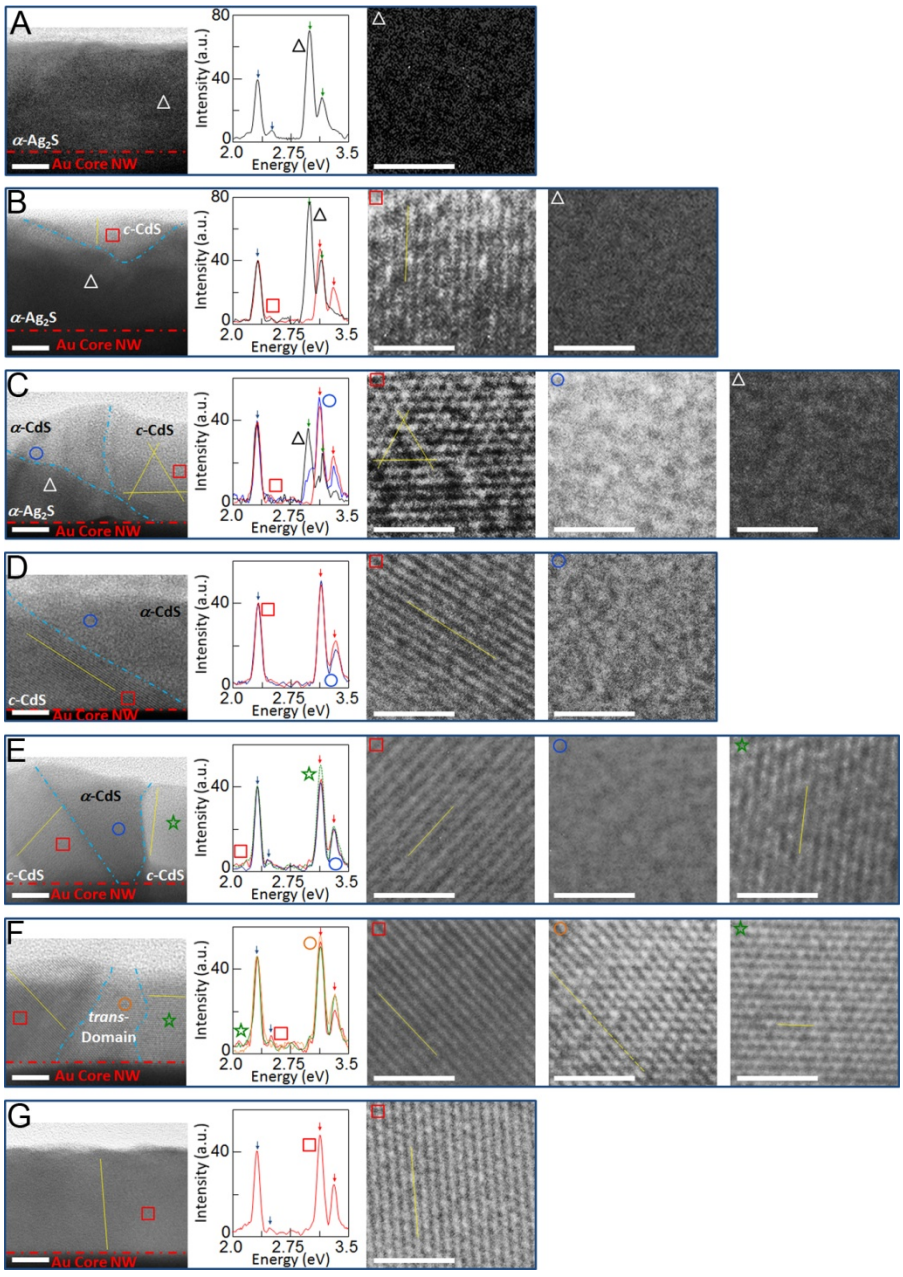

Figure 4.13 Assignment of structures and elemental compositions of domains characterized at different growth stages as presented in the Figure 4.12 by the in-depth TEM imaging and spectroscopic characterizations. (A)-(G) Different non- epitaxial crystalline growth stages as described in the Figure 4.12 (Left) The same TEM images presented in the Figure 4.12. Scale bar, 10nm. (Middle) Single- point EDS spectra measured at different location as labeled by symbols in (Left). Blue, red and green arrows highlight peaks assigned for S, Cd and Ag, respectively. (Right) Corresponding high-resolution TEM images of selective areas as labeled by symbols in (Left), distinguishing crystalline domain (whose lattice orientations are highlighted by yellow solid lines) from amorphous domain. Scale bar, 2nm.

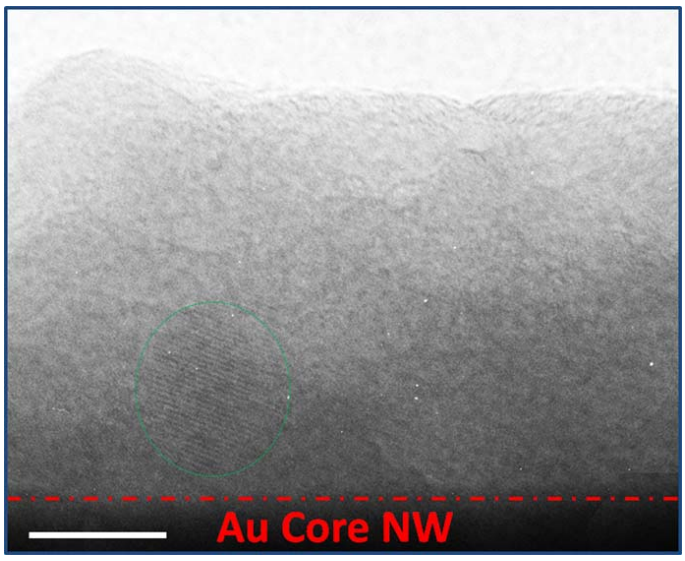

Figure 4.14 Experimental confirmation of the existence of small crystalline CdS nucleus (green dashed oval) within an amorphous CdS matrix by high- resolution TEM image, which can be attributed to mechanical shear deformation of amorphous matrix. Scale bar, 10nm.

While the observed non-epitaxial growth process phenomenologically agrees well with macroscopic normal and abnormal grain growth scenarios, the underlying driving mechanism remains elusive. The fact that our non-epitaxial monocrystalline solution growth temperature is much lower than those for traditional macroscopic normal and abnormal grain growths, typically requiring temperature close to the materials melting temperature. It suggests that conventional thermal energy mechanism cannot be the main activation energy for the large scale non- epitaxial monocrystalline growth. It is generally believed that at low temperature (compared with melting temperature) most grain boundaries are smooth and migrate slowly, leading to grain growth stagnation. However geometric constraints imposed in anisotropic nanostructures as well as flexible mechanical motion of nanostructures during synthesis can lead to high curvature of

boundaries, and thus promote high mobility grain boundaries [167]. Recent experiments have demonstrated that grain boundary migration in a two-dimensional polycrystalline metal thin film could be induced by applying mechanical surface stress even at room temperature [168]. Nevertheless, there has been no direct evidence to confirm such mechanically driven grain growth mechanism due to the experimental challenges in applying in-situ mechanical force during crystalline growth as well as in separating the effect of mechanical force from thermal effect, which turns out to be a major benefit of bottom-up solution phase synthesis.

During the cation exchange and non-epitaxial crystalline growth process in solution, mechanical stirring is always applied with speed controllable by hot plate setting. Under optimum synthetic conditions for coaxial nanowires with core diameters of 30nm and 60nm, fluid flow velocities by stirring are estimated to be 0.67m/s and 1.20m/s, respectively. I have observed that such mechanical disturbance plays a key role in the non-epitaxial monocrystalline growth. Mechanical stirring in solution containing anisotropic nanostructures (such as nanowires) can lead to two effects: constant fluid flow around nanostructures and mechanical deformation of nanostructures. Both effects can result in shear stress, whose magnitude depends on the aspect ratio of nanostructures. For anisotropic nanostructures with large aspect ratio (such as long nanowires), the latter effect can be very significant. Because the aspect ratio of anisotropic nanowires can be easily tuned by changing diameter and/or length, I use nanowires as an example and present two models schematically in the Figure 4.15 to qualitatively illustrate these two effects (the conclusions drawn from nanowires can also be applied to other types of anisotropic nanostructures): (1) Model presented in (**A**; top in Figure 4.15) is modified

from the literature [169] and a few conclusions are summarized as follows. When a uniform fluid flow velocity, ***U***, along the nanowire axial direction is assumed, shear stress can be caused with magnitude depending on location along straight nanowires: nearby the end of nanowires that possess higher local curvature shear stress can be expressed by $\tau \approx \frac{\mu U}{r}$, where μ is the viscosity of the fluid and r is the radius of core-shell nanowires. On the other hand, at places far away from the end (i.e., smaller curvature), the shear stress can be given as $\tau(x) \approx \frac{\mu U}{r} \ln\left(\frac{Ur^2}{4\nu x}\right)$, where $\nu=\mu/\rho$, with ρ being the fluid density and x is the distance away from the end of nanowires. When $x>>r$ (smaller curvature), $\tau(x)$ decreases as compared with the value in the end (higher curvature). (2) Model presented in (**B**; bottom in Figure 4.15) considers the effect of deformation of nanowires due to mechanical stirring in solution [170-172]. This effect becomes more pronounced when aspect ratio of nanowires increases. When the nanowire is assumed as a continuum beam with circular cross section, averaged shear stress can be approximated as $\tau_{avg} \approx \frac{2V}{3\pi r^2}$, where V is the total shear force at the beam section when beam is deformed and is proportional to the deformation and the length of beam [173]. These two models offer underlying mechanisms for the existence of mechanical shear stress in an anisotropic nanostructure due to mechanical stirring, and suggest that the magnitude of shear stress can be significantly increased by increasing stirring speed, decreasing radius, and/or increasing length of nanostructures. All of these predictions agree qualitatively with the experimental finding of the formation of monocrystalline semiconductor shell as described in the main text. It is also worth noting that model **B** is oversimplified for a

core-shell configuration, in which core and shell might not be considered as “bonded” to form a single intact piece of continuum beam. While more advanced modeling and analysis are needed to account for this effect, qualitatively it would result in enhanced shear stress at the core-shell interface [173]. Indeed, the small CdS crystalline nucleus in the Figure 4.14 occurred near the Au-CdS interface. The latter effect is particularly important for anisotropic structure with large aspect ratio and can lead to shear stress in range of MPa - GPa under external forces [174].

In order to further elucidate roles of mechanical effect on non-epitaxial monocrystalline growth of anisotropic nanostructures, I have carried out a few control experiments: (1) I have observed that yield of monocrystalline CdS shell shows a significant dependence on the stirring speed during non-epitaxial growth process. Comparative study of the process with and without mechanical stirring show that a static growth can only lead to polycrystallinity of CdS shell instead of monocrystallinity; (2) I have investigated and compared monocrystalline growth process with two different Au core diameters (60nm and 30nmn) but with similar semiconductor shell thickness and length. While monocrystalline growth of CdS shell can be achieved with both core diameters (Figure 4.7, Figure 4.8, and Figure 4.9), averaged growth time required for achieving monocrystalline CdS shell with 30nm- Au core is about 2/3 shorter than that of the 60nm core under the same synthetic condition. This observation can be understood by the fact that mechanical shear stress is proportional to flow velocity and viscosity but reversibly proportional to the diameter as discussed above [172, 175, 176]; and (3) one feature predicted for shear stress-driven migration of grain boundary between two mis-oriented crystalline domains is the relatively easy shape change accommodated with size

enlargement of dominate/subpopulation domain [177]. Indeed I have observed that coaxial nanowire with large aspect ratios are easily found to possess curved morphology with perfect monocrystallinity of semiconductor shell, whose curvature increases as the aspect ratio increases, due to the size dependent Young's modulus of nanostructures (Figure 4.16) [175, 176]. This observation has provided direct experimental evidence of mechanical stress driven monocrystalline growth in solution.

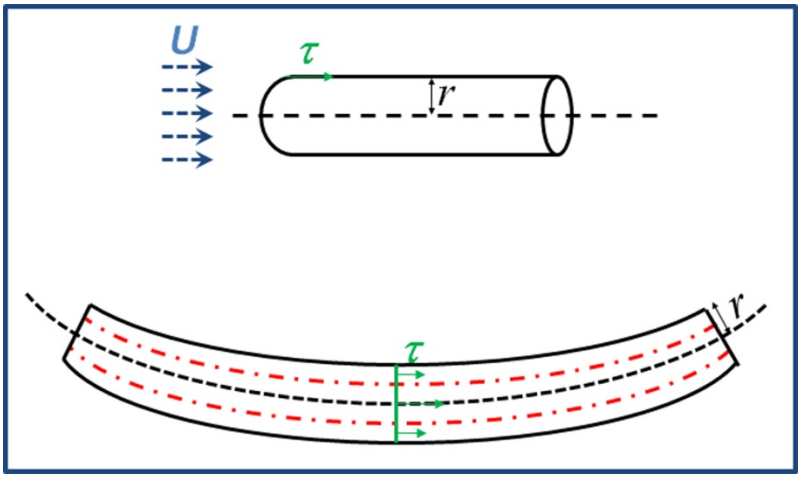

Figure 4.15 Models of mechanical stirring induced shear stress, τ, of nanowires in a solution. (A) Shear stress due to fluid flow with far-field velocity U [169]. (B) Shear stress due to mechanical deformation [173]. Black dashed line represent central neutral axis of nanowire. Red dashed lines represent core-shell interface. Green solid line represents cross-section of nanowire.

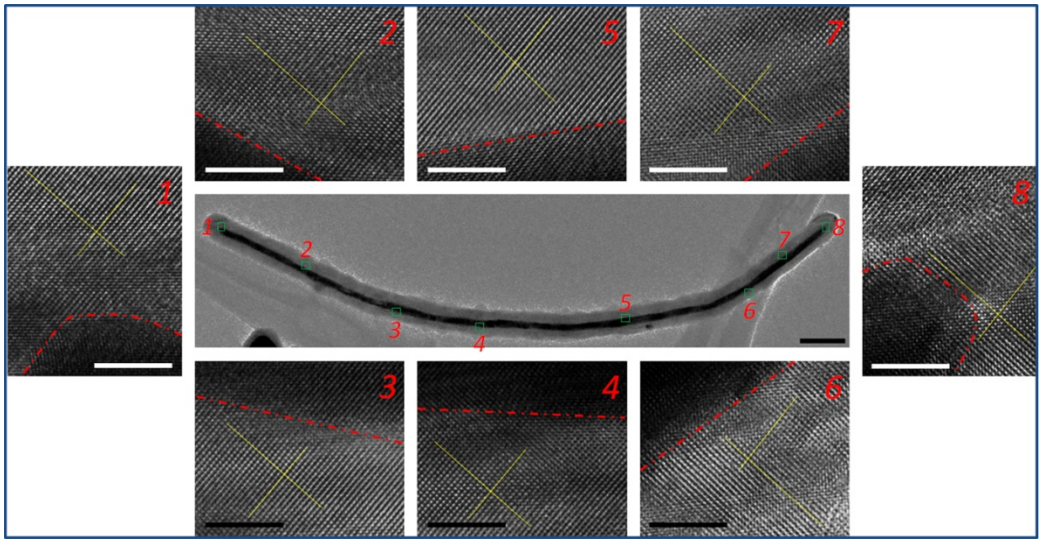

Figure 4.16 A ~3.3 μm long coaxial Au-CdS nanowires with Au core diameter of 30nm. (Center) TEM image of an intact nanowire, showing highly bent morphology. Scale bar, 200nm. Area- dependent high- resolution TEM images of eight numerically labeled selective areas as highlighted in (Center), showing perfect monocrystalline feature and identical lattice orientations (yellow solid line) along the whole nanowire that are independent on local curvature. Red dashed line represents metal-semiconductor interface, highlighting different local curvature. Scale bar, 5nm.

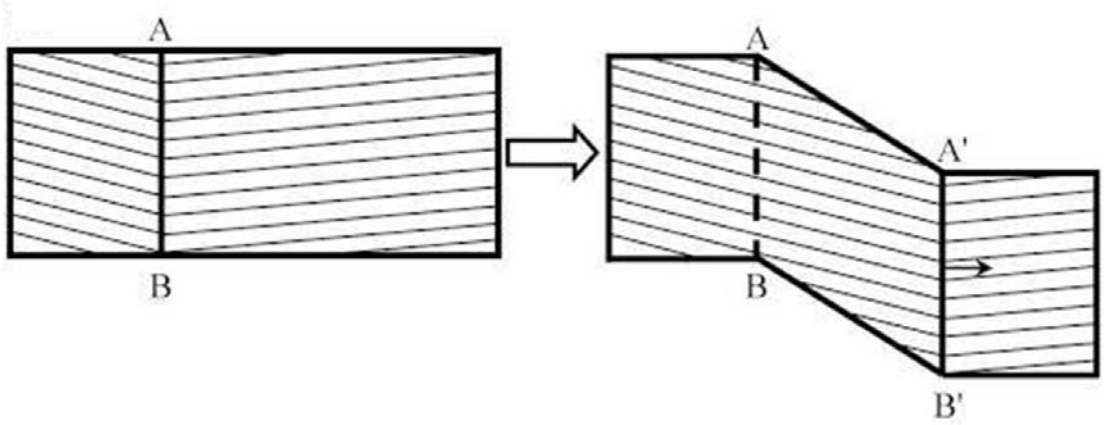

Figure 4.17 Stress-driven migration of grain boundaries in bicrystal [177].

4.5 Summary

Unprecedented control of hybrid core-shell nanostructures on two independent parameters, shape and monocrystallinity, represents a significant advance in the complexity and functionality of building blocks for nanoscience and nanotechnology. I have demonstrated a versatile synthetic approach to achieve independent morphology control of metal core and monocrystalline semiconductor shell in anisotropic nanostructures with various aspect ratios, spanning from the nano- to the micron- length scale. Although conventional grain growth mechanisms fail to explain this novel non-epitaxial monocrystalline growth process, our experiment offers a new test bed for understanding novel nanoscale mechanically driven grain growth, thus substantially advancing our understanding of crystalline growth mechanism. All these together should pave the way for the creation of novel routes for designing materials and devices with diverse functions, and for development of novel "metamaterials". For example, quantum cables by hybrid coaxial nanowires consisting of a metallic plasmonic core and a high-gain monocrystalline semiconductor shell can combine dimensionality confinement, engineered inherent hybrid metal-dielectric interfaces with strong plasmonic mode confinement and long- range propagation, with transport in which metal Au core can simultaneous serve as the backbone for unique electrical contact, leading to the implementation of different schemes for electronic-plasmonic-photonic devices at the nanoscale.

Chapter 5: Summary and Future Work

One- dimensional (1D) nanowires represent fascinating nanoscale material system because of their size related quantum confinement effect and anisotropic properties. The control of composition, size, shape and structure of nanowires is essential to their properties and applications. Therefore, the availability of precise and tunable structure and functionality control of pure metallic, magnetic and semiconducting nanowires as well as their axial and radial heterostructure demonstrated in this thesis should offer invaluable opportunity to investigate fundamental nanoscience and to explore their exciting application of novel nanotechnology.

In the Chapter 2, I showed a rational new fabrication of the flexible AAO templates. Self-organized nanoporous structures can be achieved and tailored by versatile constant current anodization and its combination with constant voltage anodization. This study can also advance our understanding of the formation mechanism of well-ordered self- organized nanoporous pattern in aluminum oxide.

As one important application of well-ordered nanoporous AAO templates, I demonstrated in the Chapter 3 that these engineered structures can be used to control steady state diffusion- limited electrodeposition by AC and DC techniques. Through precise control of such as growth rate and composition of electrolytes, various high quality and uniform 1D nanostructures (including pure metallic, magnetic and semiconducting nanowires and more complex axial and radial heterostructures) have been achieved. An availability of these 1D nanostructures can allow investigation of

much fascinating aspect of 1D physics, including some preliminary characterizations of excitonic confinement, anisotropic magnetism and tunable surface plasmon resonance.

As a further extension of controlled 1D synthesis in the Chapter 3, the Chapter 4 presents a very important materials advance by developing a versatile non-epitaxial synthetic strategy to achieve unprecedented control of two fundamental materials parameters of metal-semiconductor core-shell nanostructures: anisotropy and crystallinity. Various conformal and non-conformal metal-monocrystalline semiconductor shell nanostructures, ranging from nano- to micron-meter length scale, have been achieved. Additionally and importantly, our study in Chapter 4 has also revealed a new mechanical stress driven crystalline growth mechanism unique in the bottom-up synthesis.

Currently, most anodization is performed with low concentration (i.e., 0.3M) of acid electrolyte including oxalic and phosphoric acid and it limited tunability of AAO template. While we focused on anodization with sulfuric acid in the Chapter 2, similar method should be readily applied to other acid electrolytes to further extend regime of self- ordered nanoporous structure. Importantly, the periodic configuration of 1D nanostructures enabled by patterned AAO templates could present enhanced unique anisotropic properties with precise dimension and crystallinity engineering. Therefore, future combination of various electrochemical deposition approaches (in Chapter 3) with tunability of self- ordered nanoporous template (in Chapter 2) could provide powerful means for observation of light trapping effect by enhancing the optical absorption efficiency of the materials in the field of energy application [178-180], for enhancement

of the photocurrent efficiency of photo- generated electron-hole pairs in aligned nanowires [181], for high density magnetic recording [51, 52] and sensors [53]. Moreover, our novel synthetic route should be very useful to create complexity and functionality of building blocks for nanoscience and nanotechnology. As a next step, unique anisotropic physics should be explored through for example, exciton-plasmon interactions including tunable resonance plasmonic nanocavity by semiconductor exciton coupling and/or enhanced resonance mode in axial cavity of semiconductor nanowires by SRP interaction. This can be achieved by precise crystallinity and dimensionality engineering, and more materials combination should be explored by combination of core nanowire synthesis from the template- assisted electrodeposition in Chapter 3 and novel non-epitaxial synthetic approach for monocrystalline semiconductor shell formation in Chapter 4. This combination will be employed not only to develop scale up production of uniformly controlled various metal core and non-epitaxial grown monocrystalline semiconductor shell but also to investigate reliable and systematic control of size-dependent nanoscale stress driven grain growth mechanisms.

Bibliography

1. Peercy, P.S., *The drive to miniaturization.* Nature, 2000. **406**(6799): p. 1023-1026.

2. Moore, G.E., *Cramming More Components Onto Integrated Circuits.* Proceedings of the Ieee, 1998. **86**(1): p. 82-85.

3. Meyer, G., et al., *Controlled Atom by Atom Restructuring of a Metal Surface with the Scanning Tunneling Microscope.* Physical Review Letters, 1997. **78**(8): p. 1512.

4. Huang, D., H. Uchida, and M. Aono, *Deposition and subsequent removal of single Si atoms on the Si(111)-7x7 surface by a scanning tunneling microscope.* Journal of Vacuum Science & Technology B: Microelectronics and Nanometer Structures, 1994. **12**(4): p. 2429-2433.

5. Avouris, P., *Manipulation of Matter at the Atomic and Molecular Levels.* Accounts of Chemical Research, 1995. **28**(3): p. 95-102.

6. Murray, C.B., C.R. Kagan, and M.G. Bawendi, *Synthesis and Characterization of Monodisperse Nanocrystals and Close-Packed Nanocrystal Assemblies.* Annual Review of Materials Science, 2000. **30**(1): p. 545-610.

7. Puntes, V.F., K.M. Krishnan, and A.P. Alivisatos, *Colloidal Nanocrystal Shape and Size Control: The Case of Cobalt.* Science, 2001. **291**(5511): p. 2115-2117.

8. Morales, A.M. and C.M. Lieber, *A Laser Ablation Method for the Synthesis of Crystalline Semiconductor Nanowires.* Science, 1998. **279**(5348): p. 208-211.

9. Kim, K.S., et al., *Large-scale pattern growth of graphene films for stretchable transparent electrodes.* Nature, 2009. **457**(7230): p. 706-710.

10. Xia, Y., et al., *One-Dimensional Nanostructures: Synthesis, Characterization, and Applications.* Advanced Materials, 2003. **15**(5): p. 353-389.

11. Zhong Lin, W., *Piezopotential gated nanowire devices: Piezotronics and piezo-phototronics.* Nano Today, 2010. **5**(6): p. 540-552.

12. Yazawa, M., M. Koguchi, and K. Hiruma, *Heteroepitaxial ultrafine wire-like growth of InAs on GaAs substrates.* 1991. - **58**(- 10).

13. Chu, S.Z., et al., *Fabrication of Ideally Ordered Nanoporous Alumina Films and Integrated Alumina Nanotubule Arrays by High-Field Anodization.* Advanced Materials, 2005. **17**(17): p. 2115-2119.

14. Li, Y., et al., *Nanowire electronic and optoelectronic devices.* Materials Today, 2006. **9**(10): p. 18-27.

15. Law, M., J. Goldberger, and P. Yang, *Semiconductor Nanowires and Nanotubes.* Annual Review of Materials Research, 2004. **34**(1): p. 83-122.

16. Liu and P. Guyot-Sionnest, *Synthesis and Optical Characterization of Au/Ag Core/Shell Nanorods.* The Journal of Physical Chemistry B, 2004. **108**(19): p. 5882-5888.

17. Ma, Y., et al., *Au@Ag Core-Shell nanocubes with finely tuned and well-controlled sizes, shell thickness, and optical properties.* ACS Nano, 2010. **4**: p. 6725-6734.

18. Li, Z., et al., *Controlled Synthesis of CdSe Nanowires by Solution–Liquid–Solid Method.* Advanced Functional Materials, 2009. **19**(22): p. 3650-3661.

19. Tang, Z., N.A. Kotov, and M. Giersig, *Spontaneous Organization of Single CdTe Nanoparticles into Luminescent Nanowires.* Science, 2002. **297**(5579): p. 237-240.

20. Cho, K.-S., et al., *Designing PbSe Nanowires and Nanorings through Oriented Attachment of Nanoparticles.* Journal of the American Chemical Society, 2005. **127**(19): p. 7140-7147.

21. Wang, N., Y. Cai, and R.Q. Zhang, *Growth of nanowires.* Materials Science and Engineering: R: Reports, 2008. **60**(1-6): p. 1-51.

22. Rycenga, M., et al., *Controlling the Synthesis and Assembly of Silver Nanostructures for Plasmonic Applications.* Chemical Reviews, 2011. **111**(6): p. 3669-3712.

23. Mayer, K.M. and J.H. Hafner, *Localized Surface Plasmon Resonance Sensors.* Chemical Reviews, 2011. **111**(6): p. 3828-3857.

24. Huang, X., S. Neretina, and M.A. El-Sayed, *Gold Nanorods: From Synthesis and Properties to Biological and Biomedical Applications.* Advanced Materials, 2009. **21**(48): p. 4880-4910.

25. Schatz, G.C. and R.P. Van Duyne, *Electromagnetic Mechanism of Surface-Enhanced Spectroscopy.* Handbook of Vibrational Spectroscopy, 2002.

26. McFarland, A.D., et al., *Wavelength-scanned surface-enhanced Raman excitation spectroscopy.* Journal of Physical Chemistry B, 2005. **109**(22): p. 11279-11285.

27. Gans, R., *Über die Form ultramikroskopischer Goldteilchen.* Annalen der Physik, 1912. **342**(5): p. 881-900.

28. Gans, R., *Über die Form ultramikroskopischer Silberteilchen.* Annalen der Physik, 1915. **352**(10): p. 270-284.

29. Kelly, K.L., et al., *The Optical Properties of Metal Nanoparticles: The Influence of Size, Shape, and Dielectric Environment.* The Journal of Physical Chemistry B, 2002. **107**(3): p. 668-677.

30. Bohren, C.F. and D.R. Huffman, *Rayleigh-Gans Theory*, in *Absorption and Scattering of Light by Small Particles*. 2007, Wiley-VCH Verlag GmbH. p. 158-165.

31. Huang, X., et al., *Cancer Cell Imaging and Photothermal Therapy in the Near-Infrared Region by Using Gold Nanorods.* Journal of the American Chemical Society, 2006. **128**(6): p. 2115-2120.

32. Steinbrück, A., et al., *Preparation and Optical Characterization of Core-Shell Bimetal Nanoparticles.* Plasmonics, 2006. **1**(1): p. 79-85.

33. Yang, Y., et al., *Preparation of Au–Ag, Ag–Au core–shell bimetallic nanoparticles for surface-enhanced Raman scattering.* Scripta Materialia, 2008. **58**(10): p. 862-865.

34. Hubenthal, F., et al., *Tuning the surface plasmon resonance by preparation of gold-core/silver-shell and alloy nanoparticles.* The European Physical Journal D - Atomic, Molecular, Optical and Plasma Physics, 2005. **34**(1): p. 165-168.

35. Huang, C.-C., Z. Yang, and H.-T. Chang, *Synthesis of Dumbbell-Shaped Au−Ag Core−Shell Nanorods by Seed-Mediated Growth under Alkaline Conditions.* Langmuir, 2004. **20**(15): p. 6089-6092.

36. Chou, S.Y., *Patterned magnetic nanostructures and quantized magnetic disks.* Proceedings of the Ieee, 1997. **85**(4): p. 652-671.

37. Ross, C., *Patterned magnetic recording media.* Annual Review of Materials Research, 2001. **31**: p. 203-235.

38. Whitney, T.M., et al., *Fabrication and Magnetic Properties of Arrays of Metallic Nanowires.* Science, 1993. **261**(5126): p. 1316-1319.

39. Liu, K., et al., *Perpendicular giant magnetoresistance of multilayered Co/Cu nanowires.* Physical Review B, 1995. **51**(11): p. 7381.

40. Nielsch, K., et al., *Uniform Nickel Deposition into Ordered Alumina Pores by Pulsed Electrodeposition.* Advanced Materials, 2000. **12**(8): p. 582-586.

41. Wang, Y.W., et al., *Fabrication of Ordered Ferromagnetic−Nonmagnetic Alloy Nanowire Arrays and their Magnetic Property Dependence on Annealing Temperature.* The Journal of Physical Chemistry B, 2002. **106**(10): p. 2502-2507.

42. AlMawlawi, D., N. Coombs, and M. Moskovits, *Magnetic properties of Fe deposited into anodic aluminum oxide pores as a function of particle size.* Journal of Applied Physics, 1991. **70**(8): p. 4421-4425.

43. Sun, M., et al., *Electrodeposition of highly uniform magnetic nanoparticle arrays in ordered alumite*. Vol. 78. 2001: AIP. 2964-2966.

44. Li, F. and R.M. Metzger, *Activation volume of alpha-Fe particles in alumite films*. Vol. 81. 1997: AIP. 3806-3808.

45. Nagayama, M. and K. Tamura, *Dissolution of the anodic oxide film on aluminium in a sulphuric acid solution.* Electrochimica Acta, 1967. **12**(8): p. 1097-1107.

46. Nielsch, K., et al., *Hexagonally ordered 100 nm period nickel nanowire arrays*. Vol. 79. 2001: AIP. 1360-1362.

47. Lieber, C.M. and Z.L. Wang, *Functional nanowires.* MRS Bulletin, 2007. **32**(2): p. 99-108.

48. Yan, R., D. Gargas, and P. Yang, *Nanowire photonics.* Nat Photon, 2009. **3**(10): p. 569-576.

49. Daniel, L., *Electrodeposition of semiconductors.* Thin Solid Films, 2005. **487**(1-2): p. 40-48.

50. Jérôme, C. and R. Jérôme, *Electrochemical Synthesis of Polypyrrole Nanowires.* Angewandte Chemie International Edition, 1998. **37**(18): p. 2488-2490.

51. Guo, Y.-G., et al., *Ordered Ni-Cu Nanowire Array with Enhanced Coercivity.* ChemInform, 2003. **34**(16): p. no-no.

52. Yang, S., et al., *Preparation and magnetic property of Fe nanowire array.* Journal of Magnetism and Magnetic Materials, 2000. **222**(1-2): p. 97-100.

53. Zheng, G., et al., *Multiplexed electrical detection of cancer markers with nanowire sensor arrays.* Nat Biotech, 2005. **23**(10): p. 1294-1301.

54. Martin, C.R., *Nanomaterials: A Membrane-Based Synthetic Approach.* Science, 1994. **266**(5193): p. 1961-1966.

55. Sun, L., P.C. Searson, and C.L. Chien, *Electrochemical deposition of nickel nanowire arrays in single-crystal mica films*. Vol. 74. 1999: AIP. 2803-2805.

56. Mallet, J., et al., *Growth of Silicon Nanowires of Controlled Diameters by Electrodeposition in Ionic Liquid at Room Temperature.* Nano Letters, 2008. **8**(10): p. 3468-3474.

57. Xu, J., *Nanotube electronics: non-CMOS routes.* Proceedings of the Ieee, 2003. **91**(11): p. 1819-1829.

58. Jessensky, O., F. Müller, and U. Gösele, *Self-organized formation of hexagonal pore arrays in anodic alumina*. Vol. 72. 1998: AIP. 1173-1175.

59. G.E, T., *Porous anodic alumina: fabrication, characterization and applications.* Thin Solid Films, 1997. **297**(1-2): p. 192-201.

60. Li, A.P., et al., *Hexagonal pore arrays with a 50-420 nm interpore distance formed by self-organization in anodic alumina*. Vol. 84. 1998: AIP. 6023-6026.

61. Garcia-Vergara, S.J., et al., *A flow model of porous anodic film growth on aluminium.* Electrochimica Acta, 2006. **52**(2): p. 681-687.

62. Hunter, M.S. and P. Fowle, *Factors Affecting the Formation of Anodic Oxide Coatings.* Journal of The Electrochemical Society, 1954. **101**(10): p. 514-519.

63. Friedman, A.L., D. Brittain, and L. Menon, *Roles of pH and acid journal article in the anodic growth of porous alumina*. Vol. 127. 2007: AIP. 154717.

64. Thompson, G.E., et al., *Nucleation and growth of porous anodic films on aluminium.* Nature, 1978. **272**(5652): p. 433-435.

65. Garcia-Vergara, S.J., et al., *Mechanical Instability and Pore Generation in Anodic Alumina.* Proceedings: Mathematical, Physical and Engineering Sciences, 2006. **462**(2072): p. 2345-2358.

66. Li, F., L. Zhang, and R.M. Metzger, *On the Growth of Highly Ordered Pores in Anodized Aluminum Oxide.* Chemistry of Materials, 1998. **10**(9): p. 2470-2480.

67. Nicewarner-Peña, S.R., et al., *Submicrometer Metallic Barcodes.* Science, 2001. **294**(5540): p. 137-141.

68. Lee, W., et al., *Fast fabrication of long-range ordered porous alumina membranes by hard anodization.* Nat Mater, 2006. **5**(9): p. 741-747.

69. Rosenberg, R., et al., *Copper metallization for high performance silicon technology.* Annual Review of Materials Science, 2000. **30**: p. 229-262.

70. Martin, C.R., *Membrane-Based Synthesis of Nanomaterials.* Chemistry of Materials, 1996. **8**(8): p. 1739-1746.

71. Penner, R.M. and C.R. Martin, *Preparation and electrochemical characterization of ultramicroelectrode ensembles.* Analytical Chemistry, 1987. **59**(21): p. 2625-2630.

72. Martin, C.R., *Template synthesis of polymeric and metal microtubules.* Advanced Materials, 1991. **3**(9): p. 457-459.

73. C. Hulteen, J. and C.R. Martin, *A general template-based method for the preparation of nanomaterials.* Journal of Materials Chemistry, 1997. **7**(7): p. 1075-1087.

74. Hurst, S.J., et al., *Multisegmented One-Dimensional Nanorods Prepared by Hard-Template Synthetic Methods.* Angewandte Chemie International Edition, 2006. **45**(17): p. 2672-2692.

75. Paunovic, M., M. Schlesinger, and D.D. Snyder, *Fundamental Considerations*, in *Modern Electroplating*. 2010, John Wiley & Sons, Inc. p. 1-32.

76. Borukhov, I., D. Andelman, and H. Orland, *Steric Effects in Electrolytes: A Modified Poisson-Boltzmann Equation.* Physical Review Letters, 1997. **79**(3): p. 435.

77. Vermilyea, D.A., *Conduction and Rectification in Anodic Oxide Films*. Vol. 36. 1965: AIP. 3663-3671.

78. Sauer, G., et al., *Highly ordered monocrystalline silver nanowire arrays*. Vol. 91. 2002: AIP. 3243-3247.

79. Patermarakis, G. and D. Tzouvelekis, *Development of a strict kinetic model for the growth of porous anodic Al2O3 films on aluminium.* Electrochimica Acta, 1994. **39**(16): p. 2419-2429.

80. Patermarakis, G. and H.S. Karayannis, *The mechanism of growth of porous anodic Al2O3 films on aluminium at high film thicknesses.* Electrochimica Acta, 1995. **40**(16): p. 2647-2656.

81. Che, G., et al., *Carbon nanotubule membranes for electrochemical energy storage and production.* Nature, 1998. **393**(6683): p. 346-349.

82. Li, A.P., et al., *Hexagonal pore arrays with a 50-420 nm interpore distance formed by self-organization in anodic alumina.* Journal of Applied Physics, 1998. **84**(11): p. 6023-6026.

83. Mikulskas, I., et al., *Aluminum Oxide Photonic Crystals Grown by a New Hybrid Method.* Advanced Materials, 2001. **13**(20): p. 1574-1577.

84. Lee, S.B., et al., *Antibody-Based Bio-Nanotube Membranes for Enantiomeric Drug Separations.* Science, 2002. **296**(5576): p. 2198-2200.

85. Liang, J., H. Chik, and J. Xu, *Nonlithographic fabrication of lateral superlattices for nanometric electromagnetic-optic applications.* Selected Topics in Quantum Electronics, IEEE Journal of, 2002. **8**(5): p. 998-1008.

86. Park, S., et al., *Self-Assembly of Mesoscopic Metal-Polymer Amphiphiles.* Science, 2004. **303**(5656): p. 348-351.

87. Masuda, H. and K. Fukuda, *Ordered Metal Nanohole Arrays Made by a Two-Step Replication of Honeycomb Structures of Anodic Alumina.* Science, 1995. **268**(5216): p. 1466-1468.

88. Asoh, H., et al., *Conditions for Fabrication of Ideally Ordered Anodic Porous Alumina Using Pretextured Al.* Journal of the Electrochemical Society, 2001. **148**(4): p. B152-B156.

89. Masuda, H., et al., *Ordered Mosaic Nanocomposites in Anodic Porous Alumina.* Advanced Materials, 2003. **15**(2): p. 161-164.

90. Lee, W., et al., *Structural engineering of nanoporous anodic aluminium oxide by pulse anodization of aluminium.* Nat Nano, 2008. **3**(4): p. 234-239.

91. Schwirn, K., et al., *Self-Ordered Anodic Aluminum Oxide Formed by H2SO4 Hard Anodization.* ACS Nano, 2008. **2**(2): p. 302-310.

92. Zhao, S., et al., *Novel Structure of AAO Film Fabricated by Constant Current Anodization.* Advanced Materials, 2007. **19**(19): p. 3004-3007.

93. Thompson, G.E., *Porous anodic alumina: fabrication, characterization and applications.* Thin Solid Films, 1997. **297**(1-2): p. 192-201.

94. Nielsch, K., et al., *Self-ordering Regimes of Porous Alumina: The 10 Porosity Rule.* Nano Letters, 2002. **2**(7): p. 677-680.

95. Zhang, Z. and et al., *Synthesis of silicon nanotubes with cobalt silicide ends using anodized aluminum oxide template.* Nanotechnology, 2010. **21**(5): p. 055603.

96. Kanakala, R., et al., *Modeling of Porous Alumina Template Formation under Constant Current Conditions.* Journal of the Electrochemical Society, 2005. **152**(1): p. J1-J5.

97. Abdel Rehim, S.S., H.H. Hassan, and M.A. Amin, *Galvanostatic anodization of pure Al in some aqueous acid solutions Part I: Growth kinetics, composition and morphological structure of porous and barrier-type anodic alumina films.* Journal of Applied Electrochemistry, 2002. **32**(11): p. 1257-1264.

98. Ono, S., M. Saito, and H. Asoh, *Self-Ordering of Anodic Porous Alumina Induced by Local Current Concentration: Burning.* Electrochemical and Solid-State Letters, 2004. **7**(7): p. B21-B24.

99. Meng, G., et al., *Controlled fabrication of hierarchically branched nanopores, nanotubes, and nanowires.* Proceedings of the National Academy of Sciences of the United States of America, 2005. **102**(20): p. 7074-7078.

100. Lee, W. and et al., *Self-ordering behavior of nanoporous anodic aluminum oxide (AAO) in malonic acid anodization.* Nanotechnology, 2007. **18**(47): p. 475713.

101. Masuda, H., et al., *Long-range-ordered anodic porous alumina with less-than-30 nm hole interval.* Japanese Journal of Applied Physics Part 2-Letters & Express Letters, 2006. **45**(42-45): p. L1165-L1167.

102. Hu, J., T.W. Odom, and C.M. Lieber, *Chemistry and Physics in One Dimension: Synthesis and Properties of Nanowires and Nanotubes.* Accounts of Chemical Research, 1999. **32**(5): p. 435-445.

103. Law, M., J. Goldberger, and P.D. Yang, *Semiconductor nanowires and nanotubes.* Annual Review of Materials Research, 2004. **34**: p. 83-122.

104. Li, W., et al., *Magnetic nanowires fabricated by anodic aluminum oxide template—a brief review.* SCIENCE CHINA Physics, Mechanics & Astronomy, 2011. **54**(7): p. 1181-1189.

105. Shingubara, S., *Fabrication of Nanomaterials Using Porous Alumina Templates.* Journal of Nanoparticle Research, 2003. **5**(1): p. 17-30.

106. Masuda, H., et al., *Highly ordered nanochannel-array architecture in anodic alumina*. Vol. 71. 1997: AIP. 2770-2772.

107. Tian, M., et al., *Electrochemical Growth of Single-Crystal Metal Nanowires via a Two-Dimensional Nucleation and Growth Mechanism.* Nano Letters, 2003. **3**(7): p. 919-923.

108. Zhang, X.Y., et al., *Fabrication and characterization of highly ordered Au nanowire arrays.* Journal of Materials Chemistry, 2001. **11**(6): p. 1732-1734.

109. Choi, J., et al., *Hexagonally Arranged Monodisperse Silver Nanowires with Adjustable Diameter and High Aspect Ratio.* Chemistry of Materials, 2003. **15**(3): p. 776-779.

110. Yu, H., et al., *Cadmium Selenide Quantum Wires and the Transition from 3D to 2D Confinement.* Journal of the American Chemical Society, 2003. **125**(52): p. 16168-16169.

111. van Vugt, L.K., et al., *One-dimensional polaritons with size-tunable and enhanced coupling strengths in semiconductor nanowires.* Proceedings of the National Academy of Sciences of the United States of America, 2011. **108**(25): p. 10050-10055.

112. Yoffe, A.D., *Low-dimensional systems: quantum size effects and electronic properties of semiconductor microcrystallites (zero-dimensional systems) and some quasi-two-dimensional systems.* Advances in Physics, 1993. **42**(2): p. 173-262.

113. Babentsov, V. and F. Sizov, *Defects in quantum dots of IIB-VI semiconductors.* Opto-Electronics Review, 2008. **16**(3): p. 208-225.

114. Routkevitch, D., et al., *Electrochemical Fabrication of CdS Nanowire Arrays in Porous Anodic Aluminum Oxide Templates.* The Journal of Physical Chemistry, 1996. **100**(33): p. 14037-14047.

115. Rao, C.N.R. and K. Biswas, *Characterization of Nanomaterials by Physical Methods*, in *Annual Review of Analytical Chemistry*. 2009, Annual Reviews: Palo Alto. p. 435-462.

116. Schmucker, A.L., et al., *Correlating Nanorod Structure with Experimentally Measured and Theoretically Predicted Surface Plasmon Resonance.* ACS Nano, 2010. **4**(9): p. 5453-5463.

117. Moon, J.-M. and A. Wei, *Uniform Gold Nanorod Arrays from Polyethylenimine-Coated Alumina Templates.* The Journal of Physical Chemistry B, 2005. **109**(49): p. 23336-23341.

118. Yin, A.J., et al., *Fabrication of highly ordered metallic nanowire arrays by electrodeposition*. Vol. 79. 2001: AIP. 1039-1041.

119. Nicoletti, O., et al., *Surface plasmon modes of a single silver nanorod: an electron energy loss study.* Opt. Express, 2011. **19**(16): p. 15371-15379.

120. Chen, H., et al., *Shape- and Size-Dependent Refractive Index Sensitivity of Gold Nanoparticles.* Langmuir, 2008. **24**(10): p. 5233-5237.

121. Sellmyer, D.J. and et al., *Magnetism of Fe, Co and Ni nanowires in self-assembled arrays.* Journal of Physics: Condensed Matter, 2001. **13**(25): p. R433.

122. Kashi, M.A. and et al., *The influence of the ac electrodeposition conditions on the magnetic properties and microstructure of Co nanowire arrays.* Journal of Physics D: Applied Physics, 2006. **39**(19): p. 4130.

123. Thongmee, S., et al., *Fabrication and magnetic properties of metallic nanowires via AAO templates.* Journal of Magnetism and Magnetic Materials, 2009. **321**(18): p. 2712-2716.

124. Kim, J. and et al., *Direct observation of alumina nanowire formation from porous anodic alumina membrane via the droplet etching method.* Nanotechnology, 2006. **17**(2): p. 355.

125. Shvartsburg, A.A., *DMSO Complexes of Trivalent Metal Ions: First Microsolvated Trications Outside of Group 3.* Journal of the American Chemical Society, 2002. **124**(41): p. 12343-12351.

126. Shvartsburg, A.A. and J.G. Wilkes, *Fragmentation Chemistry of DMSO Complexes of Metal Dications.* The Journal of Physical Chemistry A, 2002. **106**(18): p. 4543-4551.

127. Fu, J., et al., *One-Step Process To Fabricate Fe Core/Fe−Dimethylsulfoxide Shell Coaxial Nanocables.* Chemistry of Materials, 2008. **20**(5): p. 2016-2019.

128. Xiang, J., et al., *Ge/Si nanowire heterostructures as high-performance field-effect transistors.* Nature, 2006. **441**(7092): p. 489-493.

129. Törnblom, M. and U. Henriksson, *Effect of Solubilization of Aliphatic Hydrocarbons on Size and Shape of Rodlike C16TABr Micelles Studied by 2H NMR Relaxation.* The Journal of Physical Chemistry B, 1997. **101**(31): p. 6028-6035.

130. Ah, C.S., S.D. Hong, and D.-J. Jang, *Preparation of AucoreAgshell Nanorods and Characterization of Their Surface Plasmon Resonances.* The Journal of Physical Chemistry B, 2001. **105**(33): p. 7871-7873.

131. Gou, L. and C.J. Murphy, *Fine-Tuning the Shape of Gold Nanorods.* Chemistry of Materials, 2005. **17**(14): p. 3668-3672.

132. Mullin, J.W., *Crystallization*. 4th ed. 2001: Butterworth-Heinemann.

133. Kumar, S. and T. Nann, *Shape control of II-VI semiconductor nanomaterials.* Small, 2006. **3**: p. 316-329.

134. Yin, Y. and A.P. Alivisatos, *Colloidal nanocrystal synthesis and the organic-inorganic interface.* Nature, 2005. **437**: p. 664-670.

135. Lim, B. and Y. Xia, *Metal nanocrystals with highly branched morphologies.* Angew. Chem. Int. Ed., 2011. **50**: p. 76-85.

136. Xia, Y., et al., *Shape-Controlled Synthesis of Metal Nanocrystals: Simple Chemistry Meets Complex Physics?* Angew. Chem. Int. Ed., 2009. **48**: p. 60-103.

137. Habas, S.E., et al., *Shaping binary metal nanocrystals through epitaxial seeded growth.* Nature Materials, 2007. **6**: p. 692-697.

138. Rycenga, M., et al., *Controlling the synthesis and assembly of silver nanostructures for plasmonic applications.* Chemical Reviews, 2011. **111**: p. 3669-3712.

139. Jones, M.R., et al., *Templated techniques for the synthesis and assembly of plasmonic nanostructures.* Chemical Reviews, 2011. **111**: p. 3736-3827.

140. Jun, Y.-W., J.-S. Choi, and J. Cheon, *Shape control of semiconductor and metal oxide nanocrystals through nonhydrolytic colloidal routes.* Angew. Chem. Int. Ed., 2006. **45**: p. 3414-3439.

141. Tao, A.R., S. Habas, and P. Yang, *Shape control of colloidal metal nanocrystals.* Small, 2008. **4**: p. 310-325.

142. Tsung, C.-K., et al., *Sub-10nm Platinum nanocrystals with size and shape control: catalytic study for ethylene and pyrrole hydrogenation.* J.Am.Chem.Soc., 2009. **131**: p. 5816-5822.

143. Lee, J.-S., E.V. Shevchenko, and D.V. Talapin, *Au−PbS Core−Shell Nanocrystals: Plasmonic Absorption Enhancement and Electrical Doping via Intra-particle Charge Transfer.* J.Am.Chem.Soc., 2008. **130**: p. 9673-.

144. Kim, H., et al., *Synthesis and Characterization of Co/CdSe Core/Shell Nanocomposites: Bifunctional Magnetic-Optical Nanocrystals.* J.Am.Chem.Soc., 2005. **127**: p. 544.

145. Zhang, J.T., et al., *Nonepitaxial growth of hybrid core-shell nanostructures with large lattice mismatches.* Science, 2010. **327**: p. 1634-1638.

146. Sau, T.K. and C.J. Murphy, *Room temperature, high-yield synthesis of multiple shapes of gold nanoparticles in aqueous solution.* J.Am.Chem.Soc., 2004. **126**: p. 8648-8649.

147. Nikoobakht, B. and M.A. Ei-Sayed, *Preparation and growth mechanism of gold nanorods (NRs) using seed-mediated growth method.* Chem.Mater, 2003. **15**: p. 1957-1962.

148. Millstone, J.E., et al., *Iodide ions control seed-mediated growth of anisotropic gold nanoparticles.* Nano Letters, 2008. **8**: p. 2526-2529.

149. Yoo, H., et al., *Core-shell triangular bifrustums* Nano Letters, 2009. **9**: p. 3038-3041.

150. Fan, F.-R., et al., *Epitaxial growth of heterogeneous metal nanocrystals: from gold nano-octahedra to palladium and silver nanocubes.* J.Am.Chem.Soc., 2008. **130**: p. 6949-6951.

151. Kim, F., et al., *Chemical synthesis of gold nanowires in acidic solutions.* J.Am.Chem.Soc., 2008. **130**: p. 14442-14443.

152. Murphy, C.J., et al., *Anisotropic metal nanoparticles: synthesis, assembly, and optical applications.* J.Phys.Chem. B, 2005. **109**: p. 13857-13870.

153. Jackson, A.M., et al., *From homoligand- to Mixed-Ligand- Monolayer-Protected Metal Nanoparticles: A scanning Tunneling Microscopy Investigation.* J.Am.Chem.Soc., 2006. **128**: p. 11135-11149.

154. Forster, R.J., T.E. Keyes, and J.G. Vos, *Interfacial Supramolecular Assemblies*. 2003, England: John Wiley & Sons, Ltd.

155. Yan, H., et al., *Programmable nanowire circuits for nanoprocessors.* Nature, 2011. **470**: p. 240-245.

156. Qian, F., et al., *Multi-quantum-well nanowire heterostructures for wavelength-controlled lasers.* Nature Materials, 2008. **7**: p. 701-706.

157. Jung, Y., et al., *Core-shell heterostructured phase change nanowire multistate memory.* Nano Letters, 2008. **8**: p. 2056-2062.

158. Dong, Y., et al., *Coaxial group III-Nitride nanowire photovoltaics.* Nano Letters, 2009. **9**: p. 2183-2187.

159. Yan, R., D. Gargas, and P. Yang, *Nanowire photonics.* Nature Materials, 2008. **3**: p. 569-576.

160. Lauhon, L.J., et al., *Epitaxial core-shell and core-multishell nanowire heterostructures.* Nature, 2002. **420**: p. 57-61.

161. Johnson, C.J., et al., *Growth and form of gold nanorods prepared by seed-mediated, surfactant-directed synthesis.* J.Mater.Chem, 2002. **12**: p. 1765-1770.

162. Sun, Y., et al., *Crystalline silver nanowires by soft solution processing.* Nano Letters, 2002. **2**: p. 165-168.

163. Zeng, J., et al., *Selective sulfuration at the corner sites of a silver nanocrystal and its use in stabilization of the shape.* Nano Letters, 2011. **ASAP**.

164. Bording, J.K. and J. Tafto, *Molecular-dynamics simulation of growth of nanocrystals in an amorphous matrix.* Phys.Rev.B, 2000. **62**: p. 8098-8103.

165. Tarumi, R., et al., *Molecular dynamics simulation of crystallization in an amorphous metal during shear deformation.* Jpn.J.Appl.Phys., 2000. **39**: p. L611-L613.

166. Thompson, C.V., *Grain Growth in Polycrystalline Thin Films of Semiconductors.* Interface Science, 1998. **6**: p. 85.

167. Holm, E.A. and S.M. Foiles, *How Grain Growth Stops: A Mechanism for Grain-Growth Stagnation in Pure Materials.* Science, 2010. **328**: p. 1138-1141.

168. Rupert, T.J., et al., *Experimental observations of stress-driven grain boundary migration.* Science, 2009. **326**: p. 1686-1690.

169. Wang, C., et al., *Bending nanowire growth in solution by mechanical disturbance.* Nano Letters, 2010. **10**: p. 2121-2125.

170. Yun, G. and H.S. Park, *Surface stress effects on the bending properties of fcc metal nanowires.* Phys.Rev. B, 2009. **79**: p. 195421.

171. Song, F., et al., *A continuum model for the mechanical behavior of nanowires including surface and surface-induced initial stresses.* Int.J.Solids and Structures, 2011. **48**: p. 2154-2163.

172. Gao, Y. and Z.L. Wang, *Electrostatic potential in a bent piezoelectric nanowire: The fundamental theory of nanogenerator and nanopiezotronics.* Nano Letters, 2007. **7**: p. 2499-2505.

173. Bucciarelli, L.L., *Engineering Mechanics for Structures*. 2009: Dover Publications.

174. Hoffmann, S., et al., *Measurement of the bending strength of vapor-liquid-solid grown silicon nanowires.* Nano Letters, 2006. **6**: p. 622-625.

175. Chen, C.Q., et al., *Size dependence of Young's modulus in Zno nanowires.* Phys.Rev.Lett., 2006. **96**: p. 075505.

176. He, J. and C.M. Lilley, *Surface effect on the elastic behavior of static bending nanowires.* Nano Letters, 2008. **8**.

177. Bobylev, S.V. and I.A. Ovid'ko, *Mobility of triple junctions of grain boundaries during their migration in deformed nanocrystalline materials.* Rev.Adv.Mater.Sci., 2009. **22**: p. 39-51.

178. Tsakalakos, L., et al., *Silicon nanowire solar cells.* Applied Physics Letters, 2007. **91**(23): p. 233117-3.

179. Spurgeon, J.M., H.A. Atwater, and N.S. Lewis, *A Comparison Between the Behavior of Nanorod Array and Planar Cd(Se, Te) Photoelectrodes.* The Journal of Physical Chemistry C, 2008. **112**(15): p. 6186-6193.

180. Hu, L. and G. Chen, *Analysis of Optical Absorption in Silicon Nanowire Arrays for Photovoltaic Applications.* Nano Letters, 2007. **7**(11): p. 3249-3252.

181. Fan, Z., et al., *Three-dimensional nanopillar-array photovoltaics on low-cost and flexible substrates.* Nat Mater, 2009. **8**(8): p. 648-653.